Journal of
Print and Media Technology Research

Scientific contributions

Journal of Print and Media Technology Research

A PEER-REVIEWED QUARTERLY

PUBLISHED BY

A mission statement

To meet the need for a high quality scientific publishing platform in its field, the International Association of Research Organizations for the Information, Media and Graphic Arts Industries is publishing a quarterly peer-reviewed research journal.

The journal is fostering multidisciplinary research and scholarly discussion on scientific and technical issues in the field of graphic arts and media communication, thereby advancing scientific research, knowledge creation, and industry development. Its aim is to be the leading international scientific journal in the field, offering publishing opportunities and serving as a forum for knowledge exchange between all those interested in contributing to or learning from research in this field.

By regularly publishing peer-reviewed, high quality research articles, position papers, surveys, and case studies as well as review articles and topical communications, the journal is promoting original research, international collaboration, and the exchange of ideas and know-how. It also provides a multidisciplinary discussion on research issues within the field and on the effects of new scientific and technical developments on society, industry, and the individual. Thus, it intends to serve the entire research community as well as the global graphic arts and media industry.

The journal is covering fundamental and applied aspects of at least, but not limited to, the following topics:

Printing technology and related processes
- Conventional and special printing
- Packaging
- Fuel cells and other printed functionality
- Printing on biomaterials
- Textile and fabric printing
- Printed decorations
- Materials science
- Process control

Premedia technology and processes
- Colour reproduction and colour management
- Image and reproduction quality
- Image carriers (physical and virtual)
- Workflow and management

Emerging media and future trends
- Media industry developments
- Developing media communications value systems
- Online and mobile media development
- Cross-media publishing

Social impact
- Media in a sustainable society
- Environmental issues and sustainability
- Consumer perception and media use
- Social trends and their impact on media

Submissions to the Journal

Submissions are invited at any time and, if meeting the criteria for publication, will be rapidly submitted to peer-review and carefully evaluated, selected and edited. Once accepted and edited, the papers will be published as soon as possible.

✉ Contact the Editorial office: journal@iarigai.org

Journal of Print and Media Technology Research

4-2021

December 2021

Contents

A letter from the Editor

Gorazd Golob
Editor-in-Chief
E-mail: gorazd.golob@jpmtr.org
journal@iarigai.org

The last issue in 2021 comprises three original scientific papers, covering research topics from conventional printing technologies to some contemporary issues. The first paper presents the alternative method for the appropriate prediction of zonal settings of ink fountain of an offset printing press. A computer program based on a mathematic model was tested by using several theoretic examples of different coverage of the zonal area with print elements and the results are promising, however, it is also a challenge for further research on the machines with different inking systems and with dampening systems included into the model.

The second paper presents a process of development and use of a Spatial star as an upgrade of a well known Siemens star. The research is based on an original idea and well documented and practically approved process of development of quality control elements for potential use in 3D scanning and printing applications.

The third paper covers the environmental and sustainability issues with the study of preparation and laboratory tests of glucomannan–xylan blend biofilms, which can be used as an alternative for synthetic films currently used in food packaging. The results are promising; however, mechanical, optical, surface and other properties of this biomaterial should be further improved to come closer to the demanded properties of currently typically used low-density polyethylene (LDPE) and other plastic films.

The Topicalities, an overview of news, literature and events, is, unfortunately, shorter in the last part due to the influence of the last waves of a pandemic. However, Markéta Držková (marketa.drzkova@jpmtr.org), the editor of this section, prepared a useful and very informative summary of important topics in our field(s). The report on activities of the International Commission on Illumination (CIE) is a confirmation of the importance of characterization and measurement of illuminance and light sources in our working and general environment, as well as is a study of colour gamut for output media, including printers and displays. An overview of research projects conducted by the German institute Fogra shows their activities supporting the printing industry. As it is shown in the overview of 3D printing research projects conducted in Sweden, additive manufacturing is not limited only to the printing industry, actually, it is an interesting field for automotive and other 'big' industrial companies.

An overview of new books covers mainly graphic design and typography, however, also a summary of books on multimedia, 3D printing, textile printing, and printed electronics is included. The doctoral theses presented are on really different topics and from different countries. Julian Konrad Schäfer defended his thesis on the highly dynamic interfacial instability of printing ink in the cylinder gap of a gravure printing press at the Technical University of Darmstadt. The second

thesis, defended by Laurena Masbernat at the Université Paris-Saclay is on 3D printable edible materials for innovative recipes for the food of the future. Devin John Roach defended his thesis on intelligent structures and functional devices by using novel materials and methods in 3D printing at the Georgia Institute of Technology in Atlanta, Georgia.

The list of announced events is rather short and, actually, most of the events will be held as online or hybrid symposia, conferences, or another form of event. The changes of previously planned and announced events, many of which were postponed or ceased, are briefly explained and some information is added for the interested public, including the readers of the Journal. One positive news for some of them is the access to selected presentations and contributions free of charge.

I hope many readers of the Journal will find it a reliable source of information from the field(s) of their interest, as well as the appropriate publication for dissemination of the results of their research work. The call for papers is constantly open and we will appreciate your submissions. One good news is a confirmed listing of the Journal in the Directory of Open Access Journals (DOAJ). In many cases the works resulting of the projects, financed by EU or other public funds, should (obligatory) be published in the open-access publication, and the Journal of Print and Media Technology Research, published by iarigai, is now an appropriate publication to fulfill these expectations and demands.

Ljubljana, December 2021

Modeling and analysis of the ink splitting factors influence on ink filling in offset printing

Mykhailo Verkhola, Ulyana Panovyk, Myron Kalytka and Oleksandra Babych

Department of Automation and Computer Technology,
Ukrainian Academy of Printing,
Pid Holoskom St. 19, 79020 Lviv, Ukraine

m.i.werh@gmail.com
ulianapanovuk@gmail.com
kalytka_m@ukr.net

Abstract

Currently, offset printing technology is used to manufacture a wide range of printing products. Given the trends to reduced print circulation, the issue of increasing the competitiveness of printing equipment by reducing the cost of ink and paper in printing press setup remains relevant, which is most effectively achieved by improving the accuracy of its pre-adjustment. The technical condition of printing equipment, the properties of ink and paper, climatic conditions in the production room, and other factors affect the distribution of ink flows in the inking and printing system (IPS). Obviously, the change in the ink splitting factors, which occurs under the influence of these aspects, will affect the accuracy of the pre-adjustment. The purpose of this study is to model and research the effect of ink splitting factors in the contact zones of rollers and cylinders on the process of its distribution and transmission in the IPS and its ink filling and to obtain information about the weight of ink splitting factors on the accuracy of the previous adjustment. To solve this problem, computer technology has been developed using the methods of automatic control theory, methods of mathematical modeling, theory of discrete systems, and MATLAB-Simulink interactive environment. A mathematical model of offset IPS was developed to implement the research technology, which describes the operation modes of all its components. The IPS simulator of the offset machine is constructed, which reproduces the technology of printing process. Simulation modeling and analysis of the ink splitting factors that influence the process of ink distribution and transmission in the IPS are carried out. The need to determine the reliable value of the ink splitting factors in the contact zones of the rollers and cylinders is substantiated. Computer technology makes it possible to determine the ink amount accumulating in the IPS during printing process and the ink thickness and volume on the surfaces of the imprints.

Keywords: mathematical model, signal graph, inking and printing system simulator, ink flow distribution, ink volumes

1. Introduction

Offset printing is the most common way of making printed products. According to the Joseph Webb, Frank Romano, and Smithers Pira released studies cited in Romano (2015), the share of offset printing was expected to be nowadays at 30–40 % among all methods of the total print volume. To further increase the competitiveness of offset printing, specialists need to improve the methods of its application and automatic adjusting systems.

The behavior of the ink flow in the contact zones of the rollers and cylinders and the mechanism of its division is largely related to the ink properties. Today there is a wide range of printing inks, different in their prop-

erties and purpose. Scientific publications (Kapović, et al., 2019; Ma, 2010; Shen, et al., 2017) claim that the ink splitting, in addition to its properties, is influenced by the plate coverage with printing elements, paper properties, the technical condition of printing equipment, climatic conditions in the production room, and other factors. But there is no information about the impact of these indicators on the ink distribution and splitting in the zone of two moving surfaces.

A significant contribution to the development of the theoretical and methodological foundations of inking unit modeling was made by Rech (1971). He proposed a computer method for estimating the ink transfer, which allows determining the ink thickness on individual areas of the rollers and cylinders surfaces. A model

of ink transfer between two cylindrical surfaces was proposed in the scientific work published by Chu, Lin, and Cai (2019). The research results of the temperature regime in the contact zone of two rotating rollers are presented. It is established that the ink temperature at the exit from the contact zone is higher than at the entrance. The maximum temperature appears in the transition zone between the exit from the contact zone and the non-extrusion zone. However, no information is provided on the effect of temperature change on the value of ink splitting. In Liu, Li, and Lu (2016), a model of ink transfer in an offset inking and printing system (IPS) was developed based on the Reynolds equation. As a result of modeling, a directly proportional dependence of an ink layer thickness in the contact zone of the rollers on their equivalent radius is established. However, there is no information on the parameters of the ink microflows splitting at the contact zones of the IPS elements.

The difficulty of solving this problem is due to the peculiarities of offset printing (MacPhee, 1998). Depending on the properties of the printing ink and the printing speed, the nature of the rupture of the ink layer changes, namely the formation of ink threads, which negatively affect the quality of printed products (Vlachopoulos, Claypole and Bould, 2010; Claypole, Williams and Deganelo, 2012). The analysis of published works allows stating the fact of the absence of a uniform approach to the mathematical description of inking devices, transfer, and splitting of ink. The mathematical description of the ink transfer process is realized using a system of algebraic equations that reflect the ink addition and division in the contact zones of the rollers and cylinders, assuming that the ink layer is split in half.

Analysis of publications shows that information about the specific value of the ink splitting factor in the process of its transportation from the ink supply device to the blanket cylinder (BC) in these works is missing. However, it should be noted that the scientific work included in Handbook of print media (Kipphan, 2001) presents the experimental results conducted on a specially designed model of the sequentially structured IPS. Based on these studies, it was found that without dampening solution the ink splitting factor at the contact zones of the rollers and cylinders close to the printing plate varies from 0.45 to 0.50 with a change in the frequency of axially oscillating distributor roller (OR). With dampening solution, the value of these factors can increase (Kipphan, 2001). But this experiment was performed with a constant ink supply, and there is no information on how the change in the magnitude of the ink splitting factor affects the ink redistribution in the IPS, and, accordingly, its thickness on the surface of the imprints.

2. Materials and methods

2.1 Object of research

It is extremely difficult and expensive to study the influence of ink splitting factors in the contact zones of rollers and cylinders on the amount of ink supplied by the ink feed system with the help of measuring equipment. It is proposed to solve this problem by modeling the process of ink distribution and transfer in IPS, and this requires the development of appropriate computer technology. We choose the Heidelberg GTO-52 offset inking and printing system as the object of research. In our study, the IPS is considered as a summation of ink supply device, inking unit, and printing unit, in which take place the processes of supply, distributing, circulating direct and reverse ink flows, forming and application of uniform, technologically necessary layer of ink on the surface of the printing form. The IPS scheme of the offset machine Heidelberg GTO-52 is given in Figure 1. An ink is discontinuosly transmitted from the ink fountain roller (FR) to the OR 1 by the vibrator roller (VR). Next, the ink flows circulate on the surfaces of the rollers and cylinders, summing up when entering the places of their contacts and splitting at the outlet. On the printing elements of the form (plate), which is fixed on the plate cylinder (PC), the ink is transmitted by form rollers 6, 7, 11, 13. The IPS contains four ORs (1, 3, 5, and 12), which simultaneously with the rotational movement perform reciprocating axial movement. From the surface of the form, the ink is transferred to the BC, which in the area of contact with the impression cylinder (IC) applies the ink to the printed material (P).

2.2 Signal graph of the offset inking and printing system

According to the IPS scheme of the machine (Figure 1) we build a signal graph, which clearly shows the transmission of direct and reverse ink flows in the IPS during replication of printed products, a fragment of which for the first and last zone is shown in Figure 2. The vertices at the graph input correspond to the ink thicknesses of the zonal supply. The graph nodes reflect the volumes of ink flows at the contact points of the IPS elements. The nodes of the signal graph are connected by segments and arcs, which reflect the transmission operators of the ink flows between the contact zones of the rollers and cylinders. The segments at the graph output reflect the ink transfer operators in the appropriate zones of the imprint. Ink transfer operators reflect the value of ink splitting and the time of its transportation between adjacent contact points at the surfaces of rollers and cylinders: B_i – in the direction from the FR to the plate; H_i – in the opposite direction. Their mathematical description is presented in Equation [3] in section 2.3.

Ink thickness in the zonal ink supply

h_d^1 h_d^2 h_d^3 h_d^n

Ink thickness in the *j*-th zones of imprints

h_c^1 h_c^2 h_c^3 h_c^n

Ink fountain

Fountain roller

Vibrator roller
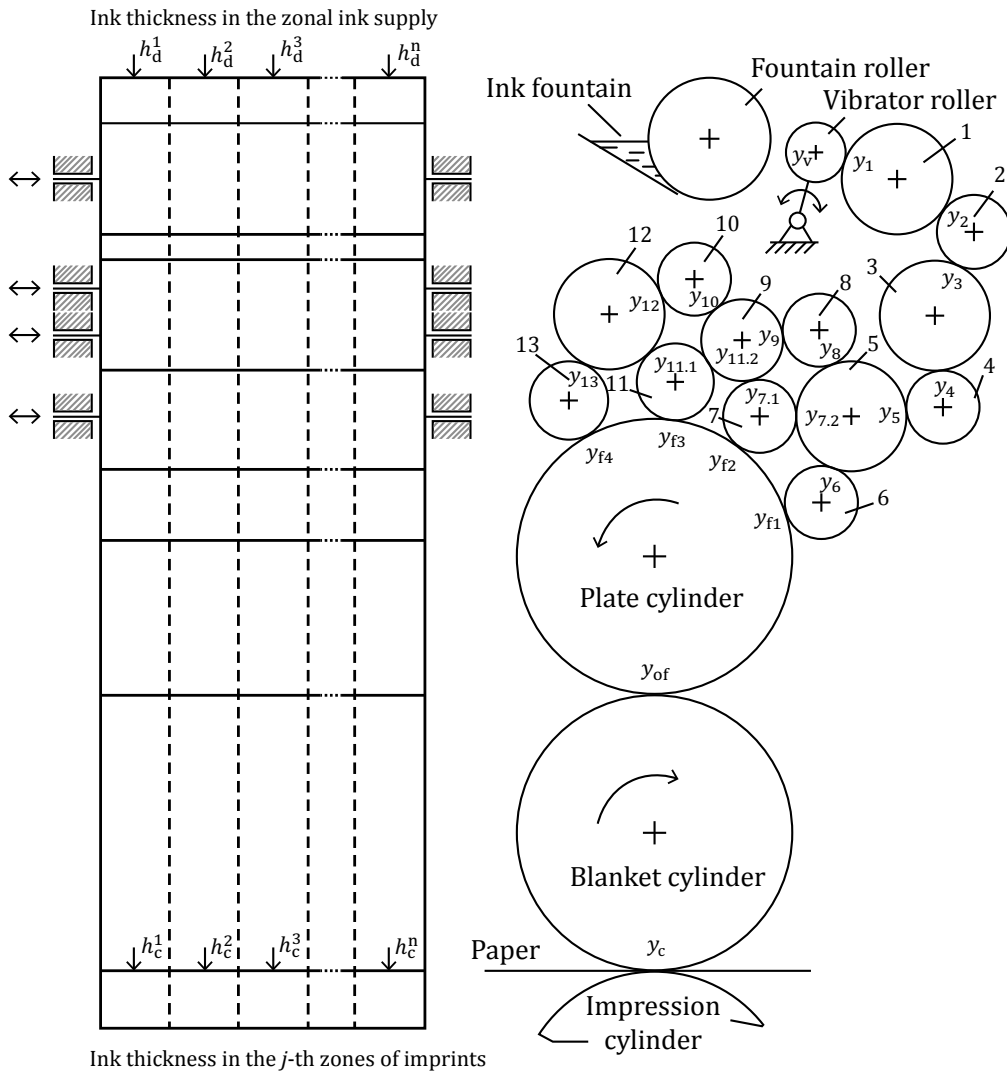
Figure 1: The inking and printing system scheme of the offset machine Heidelberg GTO-52

2.3 Mathematical model of the inking and printing system

When developing a mathematical model, we make the following assumptions: the diameters of the rollers and cylinders correspond to the diameters of the corresponding elements of the IPS of the GTO-52; the diameter of the PC is set taking into account the thickness of the printing form, and the diameter of the BC taking into account the thickness of the offset blanket; slipping in contact zones of rollers and cylinders is absent; pressure in the contact zones is neglected; linear velocities of the ink rollers and cylinders surfaces are the same; the surfaces of the IPS elements are (in axial direction) conventionally divided into zones, the number of which is equal to the number of inks supply regulators; the time of ink microflow passage on the surface of the IPS elements with a length of 1 mm corresponds to one relative unit; the period of OR movement in the axial direction corresponds to two work cycles of the offset printing machine.

Further, for variables was accepted: cross-sections of ink flows in the contact zones and on the surfaces of the IPS elements, and cross-sections of ink flows at the inlet and transmission to the imprints (Figure 3).

Based on the accepted assumptions and results of works of Verkhola and Kalytka (2019) according to the signal graph scheme and Figure 3, a system of equations (Equation [1])is compiled that describes ink distribution and its transfer from the ink fountain device to imprints in the *j*-th zone of the IPS.

Since the process of ink transfer in the IPS is discrete-continuous, it was used the mathematical apparatus of discrete Laplace transform, presented in the form of *z*-transform to describe it.
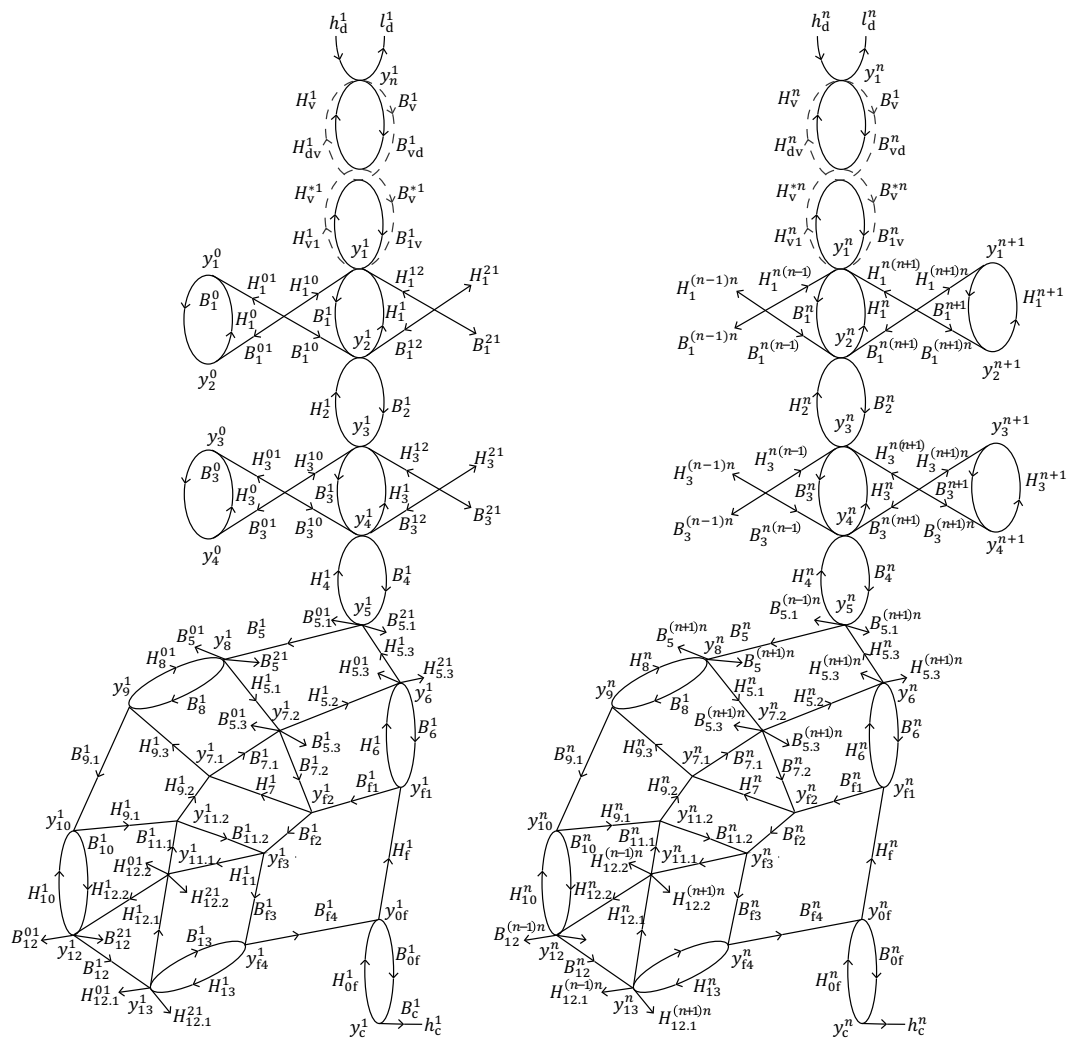
B_i^j, H_i^j are transfer operators of direct and reverse ink flow volumes by the rollers and cylinders $B_i^{j(j-1)}, H_i^{j(j-1)}$; and $B_i^{j(j+1)}, H_i^{j(j+1)}$ are transfer operators of direct and reverse ink flow volumes during the movement of the oscillator rollers in axial direction (right and left)

Figure 2: Signal graph of ink flow volume circulation in the offset printing machine GTO-52
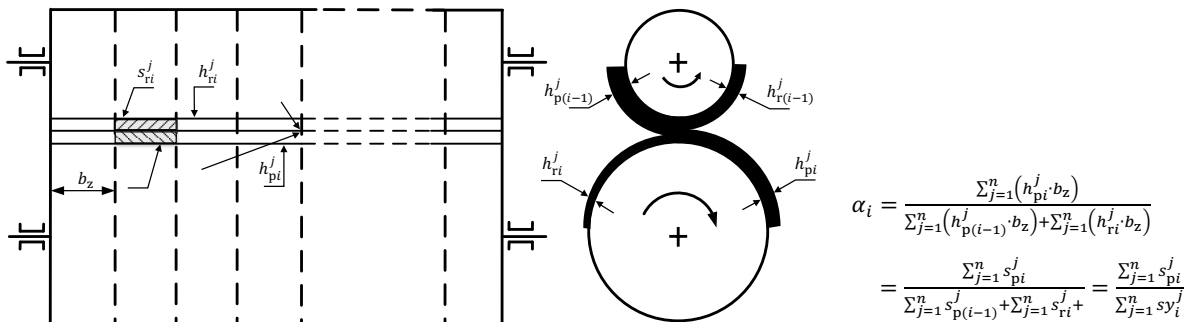
where α_i is an ink splitting factor, b_z is the width of ink supply zone (mm), h_{pi} is a thickness of direct ink flow (µm), h_{ri} is a thickness of reverse ink flow (µm), s_{pi} is the cross-sectional area of direct ink flow at leaving the contact point (mm²), s_{ri} is the cross-sectional area of reverse ink flow at leaving the contact point (mm²), y_i is the cross-sectional total area of ink flow at the contact point (mm²) and n is the number of ink supply regulation zones

Figure 3: Ink transfer in the inking and printing system

$$s_d^j(z) = b_z h_d^j(z); \; y_v^j(z) = s_d^j(z) + s_{rv}^j(z); \; s_{rd}^j(z) = H_d^j(z)y_v^j(z);$$ [1]

$$s_{pv}^j(z) = [B_{1v}^j(z)H_v^j(z) + B_v^{*j}(z)B_{vd}^j(z)]y_v^j(z) + B_v^{*j}(z)P_d^j(z)H_v^{*j}(z)y_1^j(z);$$

$$y_1^j(z) = s_{pv}^j(z) + s_{r1}^j(z) + s_{r1}^{j(J-1)}(z) + s_{r1}^{j(J+1)}(z); \; s_{p1}^j(z) = H_1^j(z)y_2^j(z);$$

$$s_{rv}^j(z) = H_v^j(z)P_g^j(z)B_v^j(z)y_v^j(z) + [H_v^j(z)H_{v1}^j(z) + H_{dv}^j(z)H_v^{*j}(z)]y_1^j(z);$$

$$y_2^j(z) = s_{p1}^j(z) + s_{p1}^{j(J-1)}(z) + s_{p1}^{j(J+1)}(z) + s_{r2}^j(z); \; s_{p2}^j(z) = B_2^j(z)y_2^j(z);$$

$$s_{r1}^j(z) = H_1^j(z)y_2^j(z); \; s_{r1}^{j(J-1)}(z) = H_1^j(z)y_2^{j-1}(z); \; s_{r1}^{j(J+1)}(z) = H_1^{j(J+1)}(z)y_2^{j+1}(z);$$

$$y_3^j(z) = s_{p2}^j(z) + s_{r3}^j(z) + s_{r3}^{j(J-1)}(z) + s_{r3}^{j(J+1)}(z); \; s_{p3}^j(z) = B_3^j(z)y_3^j(z);$$

$$s_{p3}^{j(J-1)}(z) = B_3^{j(J-1)}(z)y_3^{j-1}(z); \; s_{p3}^{j(J+1)}(z) = B_3^{j(J+1)}(z)y_3^j(z); \; s_{r2}^j(z) = H_2^j(z)y_3^j(z);$$

$$y_4^j(z) = s_{p3}^j(z) + s_{p3}^{j(J-1)}(z) + s_{p3}^{j(J+1)}(z) + s_{r4}^j(z); \; s_{p4}^j(z) = B_4^j(z)y_4^j(z);$$

$$s_{r3}^j(z) = H_3^j(z)y_4^j(z); \; s_{r3}^{j(J-1)}(z) = H_3^{j(J-1)}(z)y_4^{j-1}(z); \; s_{r3}^{j(J+1)} = H_3^{j(J+1)}(z)y_4^{j+1}(z);$$

$$y_5^j(z) = s_{p4}^j(z) + s_{r5.3}^j(z) + s_{r5.3}^{j(J-1)}(z) + s_{r5.3}^{j(J+1)}(z); \; s_{p5}^j(z) = B_5^j(z)y_5^j(z);$$

$$s_{p5}^{j(J-1)}(z) = B_5^{j(J-1)}(z)y_5^{j-1}(z); \; s_{p5}^{j(J+1)}(z) = B_5^{j(J+1)}(z)y_5^{j+1}(z); \; s_{r4}^j(z) = H_4^j(z)y_5^j(z);$$

$$y_6^j(z) = s_{r5.2}^j(z) + s_{r5.2}^{j(J-1)}(z) + s_{r5.2}^{j(J+1)}(z) + s_{r6}^j(z); \; s_{p6}^j(z) = B_6^j(z)y_6^j(z);$$

$$s_{r5.3}^j(z) = H_{5.3}^j(z)y_6^j(z); \; s_{r5.3}^{j(J-1)}(z) = H_{5.3}^{j(J-1)}(z)y_6^{j-1}(z); \; s_{r5.3}^{j(J+1)} = H_{5.3}^{j(J+1)}(z)y_6^{j+1}(z);$$

$$y_{7.1}^j(z) = s_{r7}^j(z) + s_{r9.2}^j(z); \; s_{p7.1}^j(z) = B_{7.1}^j(z)y_{7.1}^j(z); \; s_{r9.3}^j(z) = H_{9.3}^j(z)y_{7.1}^j(z);$$

$$y_{7.2}^j(z) = s_{p7.1}^j(z) + s_{r5.1}^j(z) + s_{r5.1}^{j(J-1)}(z) + s_{r5.1}^{j(J+1)}(z); \; s_{p7.2}^j(z) = B_{7.2}^j(z)y_{7.2}^j(z);$$

$$s_{r5.2}^j(z) = H_{5.2}^j(z)y_{7.2}^j(z); \; s_{r5.2}^{j(J-1)}(z) = H_{5.2}^{j(J-1)}(z)y_{7.2}^{j-1}(z); \; s_{r5.2}^{j(J+1)}(z) = H_{5.2}^{j(J+1)}(z)y_{7.2}^{j+1}(z);$$

$$y_8^j(z) = s_{p5}^j(z) + s_{p5}^{j(J-1)}(z) + s_{p5}^{j(J+1)}(z) + s_{r8}^j(z); \; s_{p8}^j(z) = B_8^j(z)y_8^j(z);$$

$$s_{r5.1}^j(z) = H_{5.1}^j(z)y_8^j(z); \; s_{r5.1}^{j(J-1)}(z) = H_{5.1}^{j(J-1)}(z)y_8^j(z); \; s_{r5.1}^{j(J+1)} = H_{5.1}^{j(J+1)}(z)y_8^{j+1}(z);$$

$$y_9^j(z) = s_{p8}^j(z) + s_{r9.3}^j(z); \; s_{p9}^j(z) = B_9^j(z)y_9^j(z); \; s_{r8}^j(z) = H_8^j(z)y_9^j(z);$$

$$y_{10}^j(z) = s_{p9}^j(z) + s_{r10}^j(z); \; s_{p10}^j(z) = B_{10}^j(z)y_{10}^j(z); \; s_{r9.1}^j(z) = H_{9.1}^j(z)y_{10}^j(z);$$

$$y_{11.1}^j(z) = s_{r12.1}^j(z) + s_{r12.1}^{j(J-1)}(z) + s_{r12.1}^{j(J+1)}(z) + s_{r11}^j(z); \; s_{p11.1}^j(z) = B_{11.1}^j(z)y_{11.1}^j(z);$$

$$s_{r12.2}^j(z) = H_{12.2}^j(z)y_{11.1}^j(z); \; s_{r12.2}^{j(J-1)}(z) = H_{12.2}^{j(J-1)}(z)y_{11.1}^j(z); \; s_{r12.2}^{j(J+1)}(z) = H_{12.2}^{j(J+1)}(z)y_{11.1}^{j+1}(z);$$

$$y_{11.2}^j(z) = s_{p11.2}^j(z) + s_{r9.1}^j(z); \; s_{p11.2}^j(z) = B_{11.2}^j(z)y_{11.2}^j(z); \; s_{r9.2}^j(z) = H_{9.2}^j(z)y_{11.2}^j(z);$$

$$y_{12}^j(z) = s_{p10}^j(z) + s_{r12.2}^j(z) + s_{r12.2}^{j(J-1)}(z) + s_{r12.2}^{j(J+1)}(z); \; s_{r10}^j(z) = H_{10}^j(z)y_{12}^j(z);$$

$$s_{p12}^j(z) = B_{12}^j(z)y_{12}^j(z); \; s_{p12}^{j(J-1)}(z) = B_{12}^{j(J-1)}(z)y_{12}^j(z); \; s_{p12}^{j(J+1)}(z) = B_{12}^{j(J+1)}(z)y_{12}^j(z);$$

$$y_{13}^j(z) = s_{p12}^j(z) + s_{p12}^{j(J-1)}(z) + s_{p12}^{j(J+1)}(z) + s_{r13}^j(z); \; s_{p13}^j(z) = B_{13}^j(z)y_{13}^j(z);$$

$$s_{r12.1}^j(z) = H_{12.12}^j(z)y_{13}^j(z); \; s_{r12.1}^{j(J-1)}(z) = H_{12.1}^{j(J-1)}(z)y_{13}^{j-1}(z); \; s_{r12.1}^{j(J+1)} = H_{12.1}^{j(J+1)}(z)y_{13}^{j+1}(z);$$

$$y_{f1}^j(z) = s_{p6}^j(z) + s_{rf}^j(z); \; s_{pf1}^j(z) = B_{f1}^j(z)y_{f1}^j(z); \; s_{r6}^j(z) = H_6^j(z)y_{f1}^j(z);$$

$$y_{f2}^j(z) = s_{p7.2}^j(z) + s_{pf1}^j(z); \; s_{pf2}^j(z) = B_{f2}^j(z)y_{f2}^j(z); \; s_{r7}^j(z) = H_7^j(z)y_{f2}^j(z);$$

$$y_{f3}^j(z) = s_{p11.2}^j(z) + s_{pf2}^j(z); s_{pf3}^j(z) = B_{f3}^j(z)y_{f3}^j(z); \; s_{r11}^j(z) = H_{11}^j(z)y_{f3}^j(z);$$

$$y_{f4}^j(z) = s_{p13}^j(z) + s_{pf3}^j(z); \; s_{pf4}^j(z) = B_{f4}^j(z)y_{f4}^j(z); \; s_{r13}^j(z) = H_{13}^j(z)y_{f4}^j(z);$$

$$y_{of}^j(z) = s_{pf4}^j(z) + s_{rof}^j(z); \; s_{pof}^j(z) = B_{of}^j(z)y_{of}^j(z); \; s_{rf}^j(z) = H_f^j(z)y_{of}^j(z);$$

$$y_c^j(z) = s_{pof}^j(z); \; s_c^j = B_c^j y_c^j(z); \; s_{rof}^j(z) = H_{of}^j(z)y_c^j(z)$$

where $y_i^j(z)$ is a z-image of the cross-sectional areas of the ink flows at the contact points of the rollers and cylinders; j are regulation zones of ink supply; $y_{fi}^j(z)$ is a z-image of the cross-sectional areas of the ink flows at the contact points of the printing form fixed on the plate cylinder with the form rollers 6, 7, 11, 13; $y_{of}^j(z), y_c^j(z)$ are z-images of ink cross-sections in the j-th contact zones of the BC with the form and paper;

$s_{pi}^j(z), s_{ri}^j(z)$ are z-images of the cross-sectional areas of direct and reverse ink flows, transmitted in the circular direction by the j-th zones of rollers' and cylinders' surfaces; $s_d^j(z)$ is a z-image of the cross-sectional areas of the ink flows supplied to the input of IPS; $h_d^j(z)$ is the thickness of the zonal ink supply; $s_{rd}^j(z)$ is z-image of the cross-sectional area of the ink flows returned to the ink fountain; $s_{pv}^j(z), s_{rv}^j(z)$ are z-images of cross-

sectional areas of forward and reverse ink flows in the j-th zones of the VR surface; $s_{\text{pfi}}^{j}(z), s_{\text{rf}}^{j}(z)$ are z-images of the cross-sectional areas of the forward and reverse ink flows, modulated by the printing form that transmitted by the j-th zones of its surface; $s_{\text{pof}}^{j}(z), s_{\text{rof}}^{j}(z)$ are z-images of the cross-sectional areas of the forward and reverse ink flows transmitted by the j-th zones of the BC surface; $s_{c}^{j}(z)$ is z-image of cross-sectional areas of ink flows transmitted to the j-th zones of imprints; $h_{c}^{j}(z) = s_{c}^{j}(z)/b_{z}$ is ink thickness in the j-th zones of imprints (b_{z} is the width of the j-th ink supply zone); $H_{d}^{j}(z)$ is transfer operator of ink return flows volumes' in the j-th zones of the FR; $B_{v}(z), H_{v}(z)$, and $B_{v}^{*}(z), H_{v}^{*}(z)$ are transfer operators of direct and return ink flows volumes' by the VR during contact with the FR and the first OR; $B_{vd}^{j}(z), B_{1v}^{j}(z)$ and $H_{v1}^{j}(z), H_{vd}^{j}(z)$ are operators of ink transfer by VR from the FR to the first OR and in the opposite direction; $B_{i}^{j(j-1)}(z), B_{i}^{j(j+1)}(z)$ and $H_{i}^{j(j-1)}(z), H_{i}^{j(j+1)}(z)$ are transfer operators of direct and reverse ink flows volumes' during the movement of the OR to the right and left; $B_{f1}^{j}(z), B_{f2}^{j}(z), B_{f3}^{j}(z), B_{f4}^{j}(z)$ are transfer operators of ink volumes' by printing form; $B_{of}^{j}(z), H_{of}^{j}(z)$ are transfer operators of direct and reverse ink flows volumes' by the BC; B_{c}^{j} is transfer operator of the ink volumes in the j-th zone of the imprint's surface.

Based on the results of previous scientific work (Verkhola and Huk, 2009; Verkhola, et al., 2015), the operators of ink transfer by the ink fountain device in z-images can be represented as follows:

$$B_{v}^{j}(z) = \left[P_{g}(z)\alpha_{v} + \overline{P}_{g}(z)\right]z^{-p_{v}};$$
$$B_{v}^{*j}(z) = P_{d}(z)z^{-p_{v}};$$
$$H_{d}^{j}(z) = P_{g}(z)(1 - \alpha_{v})z^{-p_{d}};$$
$$H_{v}^{j}(z) = P_{g}(z)z^{-r_{v}};$$
$$H_{v}^{*j}(z) = P_{g}(z)y_{1}P_{d}(z)z^{-r_{v}};$$
$$B_{vd}^{j}(z) = z^{-r_{v}}P_{g}(z)z^{-p_{1d}};$$
$$B_{1v}^{j} = \overline{P}_{g}(z)z^{-p_{1d}};$$
$$H_{dv}^{j}(z) = \overline{P}_{d}(z)\overline{z}^{-r_{d1}};$$
$$H_{v1}^{j}(z) = z^{-p_{v}}\overline{P}_{d}(z)z^{-r_{d1}}$$

[2]

where $P_{g}(z), P_{d}(z)$ are the operators that specify the duration of the joint movement of the VR with the FR and the OR 1, and their inversions $\overline{P}_{g}(z), \overline{P}_{d}(z)$; α_{v} is ink splitting factor at the contact point of the VR with the FR; $z^{-b_{d}}$ is the duration of FR rotation to a certain angle during the total supply of the ink pulse of width b_{d}; $z^{-p_{d}}, z^{-r_{d}}$ are transport delays of ink transfer from the fountain to the contact place with the VR and in the opposite direction; $z^{-p_{v}}, z^{-r_{v}}$ are transport delays of direct and return ink flows transmission by the surface of the VR in relative units; $z^{-p_{1d}}$ is the time of the VR stand near the FR in the sum of the time of its movement to the OR in relative units; $z^{-r_{d1}}$ is the time of VR movement from the first OR to the FR in the

sum with the standing time before the beginning of the FR rotation in relative units. When entering the relative time, the description of the process of ink distributes and transferring does not depend on the rotation speed of the rollers and cylinders.

Transfer operators of direct and reverse ink flows in the circular direction can be represented in Equation [3]:

$$B_{i}^{j}(z) = \alpha_{i}z^{-p_{i}};$$
$$H_{i}^{j}(z) = (1 - \alpha_{i+1})z^{-r_{i}};$$
$$B_{fi}^{j}(z) = \alpha_{f_{i}}F(z)z^{-p_{fi}};$$
$$H_{fi}^{j}(z) = (1 - \alpha_{fi})z^{-r_{f}};$$
$$B_{of}^{j} = \alpha_{of}z^{-p_{of}};$$
$$H_{of}^{j}(z) = (1 - \beta)z^{-r_{of}};$$
$$B_{c}^{j}(z) = \beta$$

[3]

where $\alpha_{i}, \alpha_{fi}, \alpha_{of}$ are ink splitting factors in the contact zones of the rollers and cylinders; $F(z)$ is the ink transfer operator at the j-th zone of the printing form; β is the ink transfer coefficient from the surface of the BC to the printed material; $z^{-p_{i}}, z^{-r_{i}}, z^{-p_{fi}}, z^{-p_{of}}, z^{-r_{of}}$ are transport delays of ink transfer by IPS elements in the circular direction between their contact points.

Formation operators of the printing elements placement in the j-th zones of the printing form surface, based on the results of Verkhola, et al. (2019), can be represented as follows:

$$F^{j}(z) = z^{-b_{o}}\left(1 - z^{-a_{1}^{j}} + z^{-\left(a_{1}^{j}+b_{1}^{j}\right)} - z^{-\left(a_{1}^{j}+b_{1}^{j}+a_{2}^{j}\right)}\right.$$
$$\left. + z^{-\left(a_{1}^{j}+b_{1}^{j}+\cdots+b_{m-1}^{j}+a_{n}^{j}\right)}\right)(1 - z^{-d_{f}})^{-1}$$

[4]

where b_{o} is the displacement of the image beginning of the printing elements relative to the form; a_{i}^{j}, b_{i}^{j} are transport delays of ink movement at a distance corresponding to the sizes of printing and blank elements in the j-th zone of the form; d_{f} is the duration of one revolution of the plate cylinder in relative units.

2.4 Simulator of the inking and printing system

Based on the functional scheme (Figure 1), the signal graph (Figure 2), and the mathematical model presented in Equation [1], a simulator of the offset printing machine GTO-52 was developed in the MATLAB-Simulink environment (Tyagi, 2012; MathWorks, 2020), which is presented in Figure 4. During the construction of the simulator, we assume that the number of ink transfer zones by the surfaces of the IPS elements is equal to the number of zones in its supply regulation ($n = 16$) in the offset printing machine GTO-52. The geometric dimensions of the rollers and cylinders, corresponding to the dimensions of IPS elements, are set due to transport delays in the ink
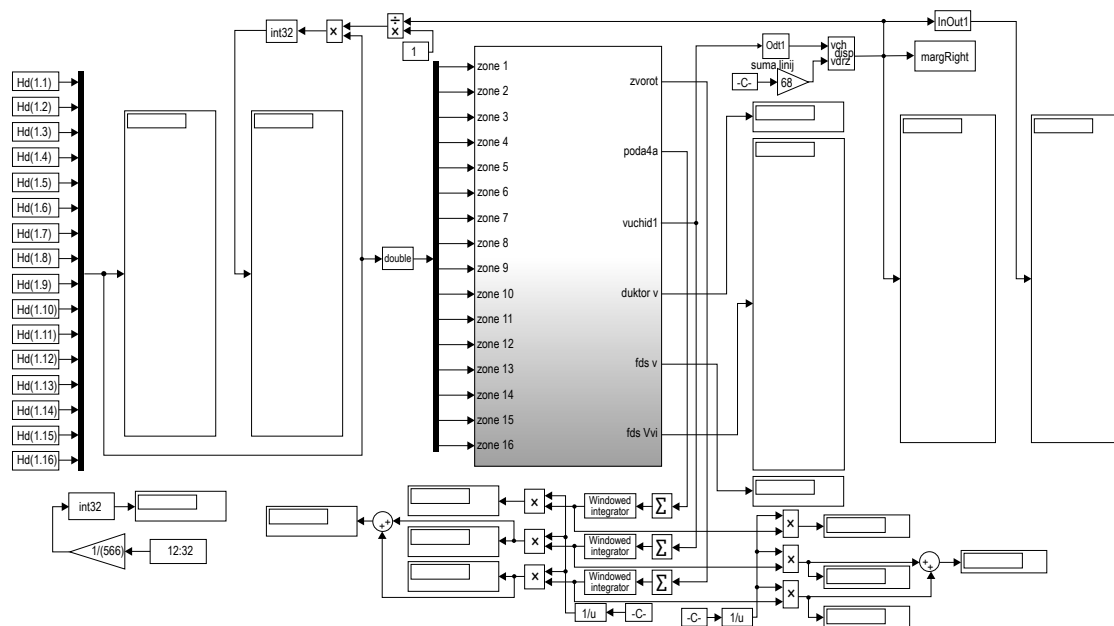
Figure 4: Scheme of the offset printing machine GTO-52 simulator

transfer operators. The ink transfer coefficient in the contact zones of the BC with the paper is taken equal to 0.7, the widths of the supply zones are the same and are b_z = 32 mm. Using expression presented in Equation [4], a subsystem of the simulator was built, which generates the parameters of the printing form.

The constructed simulator is used to study the influence of ink splitting factors in the contact zones of rollers and cylinders on the distribution of ink flow volumes in the IPS. We set the thickness of the zonal ink supply h_d and the value of the total ink supply b_d. By changing the ink splitting factors, we conduct a series of experiments of the IPS model working for the printing form with different values of the coefficients corresponding to the form's area filing by printing elements k_z. The form's filing coefficient is defined as the ratio of the printing elements area to the printing form area. The adequacy of the ink transfer process reproduction is confirmed by the balance of ink supply and its selection when the system enters the steady mode. As a result of the simulation, we determine the ink volumes V_i that accumulate on the surfaces of IPS elements, as well as the ink thicknesses and its volumes on the surface of the imprints h_c. The ink volumes on the surface of each roller, cylinder, and imprint are determined using the appropriate blocks, which implement the following mathematical expression in Equation [5]:

$$V_i(z) = \sum_{j=1}^{16} V_{p_i}^j + \sum_{j=1}^{16} V_{r_i}^j(z) \qquad [5]$$

$$= \sum_{j=1}^{16} \left(\sum_{k=1}^{d_f} (z^{-1} + z^{-2} + z^{-3} + z^{-p_i}) S_{p_i}^j(z) \right.$$

$$\left. + z^{-r_i} \right) S_{p_i}^j(z) \right)$$

where $V_{p_i}^j$, $V_{r_i}^j(z)$ are the volumes of direct and reverse ink flows that accumulate in the j-th zones of the IPS elements surfaces.

Based on the information obtained, we analyze the nature of the ink distribution in the IPS and its ink filling.

3. Results and discussion

From the analysis of scientific publications, it can be concluded that the value of the ink splitting factors in the contact zones of the IPS elements is not a constant. Therefore, we assumed that splitting factor α_i can be in the range from 0.40 to 0.50. Using the simulator for α_i = 0.40, α_i = 0.45 and α_i = 0.50 we determined the parameters of the input task with the value of the total ink supply b_d = 30 mm based on the condition that the ink thickness on the imprints surface is 1 μm. We set the obtained values of the input task at different values of α_i and performed simulations before the IPS enters the operating mode. The modeling process automatically determines the ink volumes V_i that accumulate on the elements of the IPS during printing and the ink volumes V_p and thicknesses h_c on the imprints surfaces. The obtained data are summarized in Table 1. As the ink splitting factors α_i increase from 0.40 to 0.45, the ink volume V_{IPS} that accumulates in the IPS decreases by 2 times. And with the increase of α_i to 0.50, the ink amount in the system decreases by 2.9 times.

In the next step, we expanded the values range of the ink splitting factors to 0.56 and set different values of the zonal ink supply thicknesses. At constant values

of the input task parameters, we conducted a series of model experiments by changing the ink splitting factors α_i in the range from 0.40 to 0.56. The obtained results are summarized in Table A.1 and Table A.2 (Appendix A). According to Table A.1 we constructed a diagram of the ink thicknesses zonal distribution at the output of the IPS for different values of the factors, which is shown in Figure 5.

Table 1: Distribution of ink volumes V_i in the IPS at k_z = 1.0, for the listed parameters α_i, h_d and h_c

Elements IPS	α_i = 0.40 h_d = 156 μm h_c = 0.998 μm V_i (× 10^3 mm³)	α_i = 0.45 h_d = 74 μm h_c = 0.992 μm V_i (× 10^3 mm³)	α_i = 0.50 h_d = 53 μm h_c = 1.006 μm V_i (× 10^3 mm³)
FR	17.300	8.025	5.644
VR	0.740	0.268	0.138
1	3.004	1.197	0.559
2	1.776	0.786	0.404
3	1.331	0.672	0.381
4	0.645	0.382	0.245
5	0.492	0.347	0.254
6	0.259	0.211	0.176
7	0.237	0.204	0.182
8	0.551	0.319	0.194
9	0.344	0.254	0.197
10	0.331	0.244	0.185
11	0.492	0.293	0.187
12	0.577	0.365	0.241
13	0.358	0.261	0.198
PC	0.546	0.470	0.426
BC	0.248	0.245	0.251
IPS	29.231	14.298	10.064
P	0.174	0.171	0.175
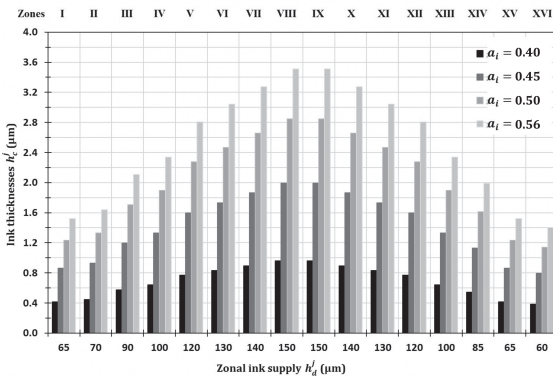
Figure 5: Ink thicknesses in the j-th zones I to XVI on the imprints with k_z = 1.0, at different ink splitting factors

As can be seen from the diagram, increasing the values of ink splitting factors in the contact zones of the rollers and cylinders significantly affects the ink thickness on the imprints. Thus, with an increase in α_i from 0.40

to 0.45, the ink thickness in all zones of the imprints increases 2.1 times, and with an increase α_i to 0.56 it increases 3.7 times. According to Table A.2, we constructed a diagram to analyze the distribution of ink flows volumes on the rollers' and cylinders' surfaces, as shown in Figure 6. When obtaining imprints at α_i = 0.40, the ink accumulates mainly at the input of the IPS, and with increasing splitting factors it is redistributed to the output of the system with a simultaneous decrease of its amount on the rollers and cylinders surfaces. The influence of splitting factors on the ink amount accumulated at the input of the IPS is shown in the diagram in Figure 7. For the lowest α_i the ink volume on the surface of roller 1 is 2 143 mm³. As α_i changes to 0.45, the ink volume decreases by 17 %, and as α_i increases to 0.56, it decreases by 68 %, respectively.
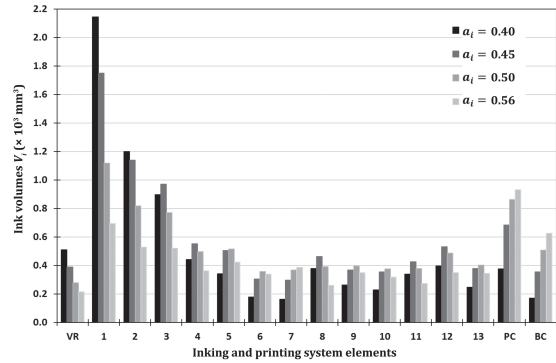
Figure 6: Distributions of ink flow volumes in the IPS at obtaining imprints with k_z = 1.0, when the values of α_i are changed
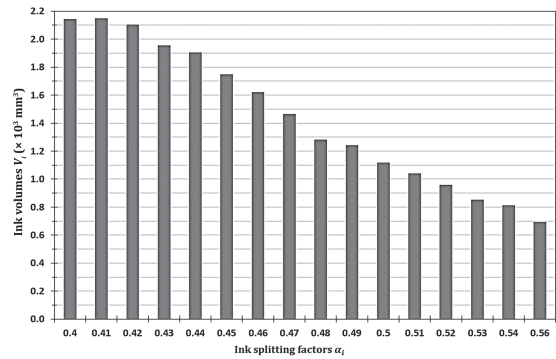
Figure 7: Dependence of the ink volume on the roller 1 surface on the factor α_i when obtaining imprints with k_z = 1.0

A completely different nature of the ink flow volumes distribution is observed in the case of change of α_i on the surfaces of the form rollers (Figure 8) and the PC and BC (Figure 9).

As can be seen from Figure 8 different ink volumes accumulate on the surfaces of the form rollers when obtaining imprints with k_z = 1.0 for α_i = 0.40. Thus,

on the form roller 7, the ink volume is the smallest, V_7 = 163 mm³, and on roller 11 it is the largest, V_{11} = 338 mm³, and this ratio is 2.1.

The total ink volume on the four form rollers 6, 7, 11, 13 is 925 mm³. As α_i increases to 0.50, the ink volumes on the surfaces of the rollers are almost aligned. Thus, the smallest ink amount is on roller 6, and the largest is on roller 13. However, the ratio between the largest and smallest volumes is only 1.1 and the total ink amount on the rollers increases 1.6 times. When printing imprints with k_z = 1.0 at α_i = 0.56, the total ink volume on the surfaces of the rollers decreases by 11 % compared to the results at α_i = 0.50. This changes the nature of the ink volumes distribution: the largest ink amount accumulates on roller 7, and the smallest is on roller 11. It is observed the almost diametrically opposite nature of the ink volume change due to the influence of α_i at the output of the IPS, i.e. on the surfaces of the PC and BC (Figure 9), compared to the input of system (Figure 7). Thus, the ink volumes on the surfaces PC and BC at α_i = 0.40 are V_{PC} = 375 mm³ and V_{BC} = 171 mm³, respectively. As α_i increases to 0.50, the ink volumes increase 2.3 and 3 times, and with α_i = 0.56, they increase 2.5 and 3.5 times, respectively.
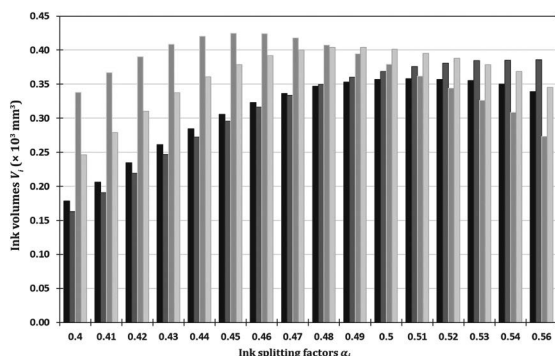
Figure 8: Dependence of the ink volumes on the surfaces of form rollers R_6, R_7, R_{11}, and R_{13} on the factor α_i when obtaining imprints with k_z = 1.0
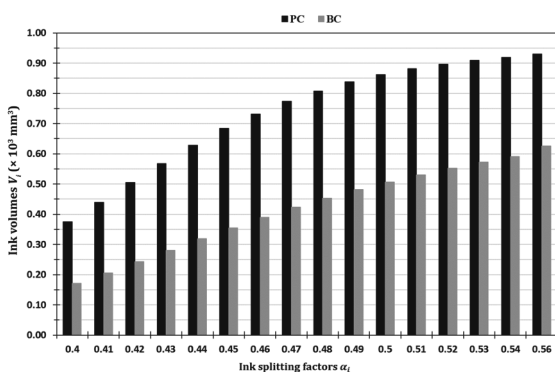
Figure 9: Dependence of the ink volumes on the surfaces of the PC and BC on the factor α_i when obtaining imprints with k_z = 1.0

The ink amount that accumulates in the IPS after the printing process consists of the sum of the ink volumes in the system without FR (V_{IPS*}) and on the surface of the FR (V_{FR}). Its distribution is shown in the diagram in Figure 10. The largest ink amount on the surface of the FR accumulates during the printing imprints with k_z = 1.0 at α_i = 0.40 and is V_{FR} = 11 880 mm³. As α_i increases, the ink volume on the surface of the FR decreases proportionally, but not significantly. So, at α_i = 0.56 it is 11 200 mm³, i.e. decrease by only 6 %. However, the change of α_i has a completely different effect on the ink amount that accumulates on the surface of all other elements of the IPS V_{IPS*}. When printing imprints with k_z = 1.0 at α_i = 0.40, the ink volume in the IPS is V_{IPS*} = 8 243 mm³, and the largest volume is obtained at α_i = 0.44, namely V_{IPS*} = 9 478 mm³. That is, it is higher than in the previous case, by 15 %. And when receiving imprints at α_i = 0.56, the ink volume that accumulates, V_{IPS*}, is 6 916 mm³, and it is 16 % less than that obtained at α_i = 0.40.

Figure 10: Dependence of ink volumes on the FR and in the IPS without it (IPS*) on α_i when obtaining imprints with k_z = 1.0

It is important, both scientifically and practically, to determine whether the same effect of the change α_i on the distribution of ink volumes on the surfaces of the IPS elements takes place during the production of imprints with a lower density of filling their elements. To perform this task, we reconfigured the simulator subsystem, which generates printing elements, so that the form is reproduced with the same zonal filling coefficients of printing elements in all zones, which are k_z = 0.2. The value of the total ink supply b_d is reduced to 10 mm. We set the thickness of the zonal ink supply h_d^j and conducted a series of model experiments changing the values of the factors α_i in the range from 0.40 to 0.56.

The results obtained are summarized in Table A.3, and Table A.4 (Appendix A). According to Table A.3 it was constructed a diagram of the ink thickness in the *j*-th zones of the imprints with k_z = 0.2 for different values of α_i (Figure 11).
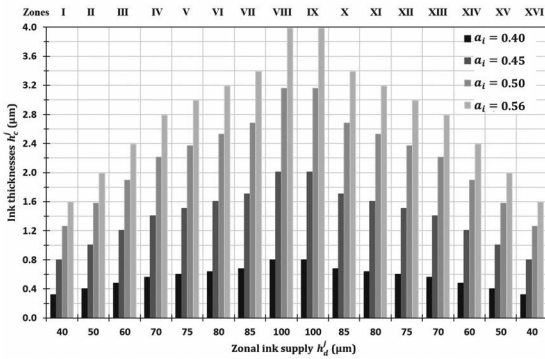
Figure 11: Ink thicknesses in the j-th zones of imprints with $k_z = 0.2$ for different factors α_i

As can be seen from the diagram, the nature of the ink thicknesses zonal distribution on the surface of the imprint is similar to that obtained during the replication of imprints with $k_z = 1.0$. But in this case, there is a much greater influence of the factors α_i on the ink thickness of imprints. Thus, with increasing α_i from 0.40 to 0.45, the ink thickness in all zones of the imprints with $k_z = 0.2$ increases 2.5 times. And, the thicknesses increase 4 and 5 times with the increase of the splitting factor α_i to 0.50 and 0.56, respectively. This increase, respectively, is 20 %, 30 % and 40 % greater than when obtaining imprints with $k_z = 1.0$ (see Figure 5).

According to Table A.4 (Appendix A), the diagrams of ink flows volumes distribution are constructed, presented in Appendix B and in Figure 12.

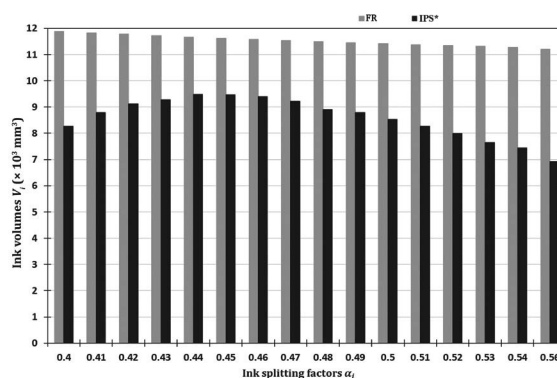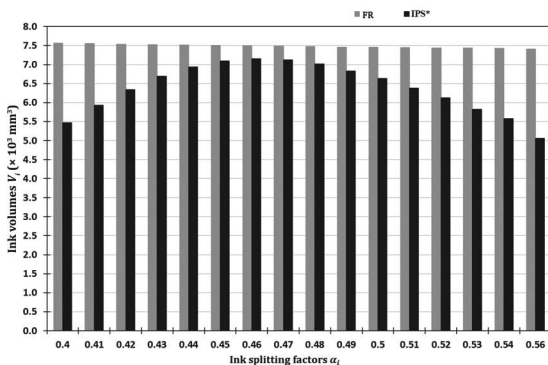*Figure 12: Dependence of ink volumes on the FR and in the IPS (IPS*) on α_i when obtaining imprints with $k_z = 0.2$*

From the comparative analysis of the diagrams shown in Figure 6 and Figure B.1 (Appendix B), we can conclude that the IPS is more sensitive to changes in the ink splitting factors when printing imprints with $k_z = 0.2$. Thus, in the process of printing imprints with $k_z = 0.2$ at $\alpha_i = 0.40$, the ink volume on the surface of the roller 1 (OR 1) (Figure B.2) is $V_1 = 1\,388$ mm³. With

an increase of α_i to 0.56, it decreases by 78 % and this decrease is 10 % greater than when obtaining imprints with $k_z = 1.0$ (Figure 7). It should be noted that in the process of printing imprints with $k_z = 1.0$ and $k_z = 0.2$ according to the diagrams shown in Figure 8 and Figure B.3 (Appendix B), the nature of the ink volumes distributions on the surfaces of the form rollers 6, 7, 11, 13 at the change of α_i in the range from 0.40 to 0.47 is identical. However, as the ink splitting factors increase, these ink flow volumes distributions on the surfaces of the form rollers are different. Thus, when modeling the process of printing imprints with $k_z = 1.0$ at $\alpha_i = 0.56$, the largest ink amount accumulates on the form roller 7, and when obtaining prints with $k_z = 0.2$, it is on the form roller 6.

Comparing the diagrams shown in Figure 8 and Figure B.4 (Appendix B), we can conclude that with increasing values of the factors α_i there is a more pronounced tendency to accumulate ink on the surfaces of the PC and BC during the printing of imprints with $k_z = 0.2$. It should be noted that in the process of obtaining imprints with $k_z = 1.0$ in the range of change α_i from 0.40 to 0.56, as shown in Figure 10, the FR accumulates a larger ink volume than the total volume on the surfaces of all other elements of the IPS (IPS*). However, another trend is observed when simulating the process of printing imprints with $k_z = 0.2$. Thus, with a change of α_i in the range from 0.45 to 0.47, the total ink volume on the surface of all components (IPS*) does not significantly exceed the ink volume that accumulates on the surface of the FR (Figure 12).

We built a diagram for analyzing the effect of the ink splitting factors α_i on the IPS ink filling according to Table A.2 and Table A.4 (Appendix A), which is shown in Figure 13.
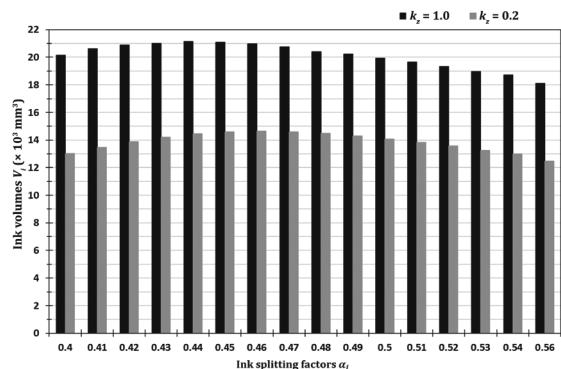
Figure 13: Ink volumes in the GTO-52 offset printing machine system obtained during modeling of the printing process

As can be seen from the diagram, the change of the factors α_i in a sufficiently wide range does not significantly affect the ink amount accumulated in IPS. A more significant influence on the ink accumulation in

M. Verkhola, et al. – J. Print Media Technol. Res. – Vol. 10 No. 4 (2021), 215–229

225

the system has the coverage of the form with printing elements. When replicating imprints with k_z = 1.0, the largest ink volume in the IPS accumulates at α_i = 0.44 and is 21 148 mm³, and the smallest is at α_i = 0.56, being 18 116 mm³. That is, the ink volume that accumulates in the system under the influence of the coefficients α_i varies from minimum to maximum value by only 16.7 %. A similar trend is characteristic when obtaining imprints with k_z = 0.2. However, the largest ink volume accumulates in IPS at α_i = 0.46 (14 645 mm³), and the smallest, as in the previous case, when α_i = 0.56, when is 12 472 mm³. In this case, the ink amount that accumulates in the system under the influence of α_i varies in the same range as during the replication of imprints with k_z = 1.0. Although the ink volume increases with decreasing α_i, the ink thickness on the surface of the imprints with k_z = 1.0 and k_z = 0.2 decreases by 1.96 and 1.76 times, respectively. As a result of the data analysis given in Table A.1, it is established that during the simulation of the process of imprints printing with the maximum coverage of the form surface by image elements (k_z = 1.0) at the change of ink splitting factors α_i from 0.50 to 0.56 ink thickness on the surface of the imprints increases by 23 %. And when receiving imprints at α_i = 0.40, the ink thickness on the imprints decreases by 66 %. Based on the data obtained by simulating the process of printing imprints with k_z = 0.2 (Table A.2), it was found that when α_i changes from 0.50 to 0.56, the ink thickness on the surface of the imprints increases by 26 %, and with decreasing α_i to 0.40 the ink thickness on the imprints is reduced by 75 %. At the same time, the effect of changing the density of form filling with printing elements is not so significant. Thus, at α_i = 0.40, the ink thickness on the imprints with k_z = 0.2 is less by 12 % compared to the ink thickness on the surface of the imprints with k_z = 1.0. And at α_i = 0.56, this thickness becomes greater by only 3 % relative to the ink thickness on the imprint with k_z = 1.0. Therefore, the efficiency of the automatic adjusting system is significantly reduced when determining the parameters

of the previous adjusting, provided that the value of the coefficients α_i in all zones of the IPS elements is 0.50, but in reality, it will be different. In this case, it will be needed to adjust the parameters of the input task already in the printing process.

4. Conclusions

The research of the ink transfer process, which takes place in the IPS of the offset machine during printing, was carried out with the help of the developed method utilising computer technology. The influence of the ink splitting factors change in the contact zones of rollers and cylinders on the redistribution of ink flows in the IPS is established. As the ink splitting factors decrease from 0.50, the ink volumes on the surfaces of the rollers and cylinders close to the system input increase. As the splitting factors increase, there is a tendency to increase the ink volume on the surfaces of the elements close to the system output. However, both at the minimum and at the maximum value of the splitting factors α_i, the total ink volume in the IPS is not the maximum. The maximum is achieved in the duplication process of imprints from the printing plate with k_z = 0.2 at the ink splitting factors α_i = 0.46. And the maximum ink volume when printing imprints with k_z = 1.0 is obtained at the ink splitting factor of 0.44. The ink thickness on the surface of the imprints significantly depends on the change of ink splitting factors in the contact zones of the rollers and cylinders. Therefore, the value of the ink splitting factors must be taken into account at the stage of the previous adjusting of the IPS. The proposed method makes it possible to determine the ink consumtion for printing jobs, taking into account the ink amount that accumulates in the IPS during printing. To obtain reliable information about the value of ink splitting during printing, it is necessary to develop an appropriate methodology, the testing of which requires thorough experimental research.

References

Chu, H., Lin, X. and Cai, L., 2019. Analysis of temperature characteristics of ink fluid based on power law model in microchannel. *Advances in Mechanical Engineering*, 11(3), pp. 1–15. https://doi.org/10.1177/1687814019833585.

Claypole, J., Williams, P.R. and Deganello, D., 2012. Control of breakup of ink filaments in offset printing. In: N. Enlund and M. Lovreček, eds. *Advances in Printing and Media Technology: Proceedings of the 39th International Research Conference of iarigai*. Ljubljana, Slovenia, September 2012, pp. 207–211.

Kapović, D., Rožić, M., Vukoje, M. and Lozo, B., 2019. Ink tack stability readings of the offset thermochromic inks. *Pigment & Resin Technology*, 48(4), pp. 309–316. https://doi.org/10.1108/PRT-07-2018-0064.

Kipphan, H. ed., 2001. *Handbook of print media*. Berlin, New York: Springer.

Liu, L., Li, K. and Lu, F., 2016. Dynamic simulation modeling of inking system based on elastohydrodynamic lubrication. *International Journal of Heat and Technology*, 34(1), pp. 124–128. https://doi.org/10.18280/ijht.340118.

Ma, J.-J., 2010. Relationship between temperature and ink transferring of the inking system and its control. *Journal of University of Shanghai for Science and Technology,* 6, pp. 609–612.

MacPhee, J., 1998. *Fundamentals of lithographic printing*. Pittsburgh, PA, USA: GATF Press.

MathWorks, 2020. *Simulink is for model-based design*. [online] Available at: <https://www.mathworks.com/products/simulink.html> [Accessed 5 July 2020].

Rech, H., 1971. *Beiträge zur experimentellen und rechnerischen Untersuchung des Farbtransportes in Walzenfarbwerken von Druckmaschinen*. Dr.-Ing. Dissertation. Technische Hochschule Darmstadt. https://tuprints.ulb.tu-darmstadt.de/id/eprint/13556.

Romano, R., 2015. Offset lithography: the future ain't what it used to be. *Nitto printing*, [blog] 14 April. Available at: <http://www.nittoprinting.com/v1/news.php?news_id=15&start=4&category> [Accessed December 2021].

Shen, Y.-H., Cheng, H.-C., Chen, Y.-W., Lu, S.-T., Lin, S.-M. and Chen, W.-H., 2017. Temperature effects on ink transfer performance of gravure offset printing for fine-line circuitry. In: *IEEE 2017 International Conference on Electronics Packaging (ICEP)*. Yamagata, Japan, 19–22 April 2017. IEEE, pp. 475–478. https://doi.org/10.23919/ICEP.2017.7939424.

Tyagi, A.K., 2012. *MATLAB and Simulink for engineers*. New Delhi, India: Oxford University Press.

Verkhola, M.I. and Huk, I.B., 2009. Modeliuvannia ta vyznachennia koefitsiienta peredachi farby peredavalnym valykom u farbovii systemi z roztyralnym tsylindrom. *Komp'iuterni tekhnolohii drukarstva*, 21, pp. 39–52. (In English: Modeling and determination of ink transfer coefficient by transfer roller at ink system with grinding cylinder. *Computer Technologies of Printing*).

Verkhola, M., Huk, I., Panovyk, U. and Spolyak, R., 2015. Information technology of verification of models authenticity of ink printing systems with the drum cylinders. *Technological Complexes*, 11(1/1), pp. 53–63.

Verkhola, M., Panovyk, U., Huk, I. and Kalytka, M., 2019. Modeling of the ink printing system and improving the accuracy of its adjustment based on the obtained three-dimensional imprints. In: N. Kryvinska, I. Izonin, M. Greguš, A. Poniszewska-Marańda and I. Dronyuk, eds. *Proceedings of the 1st lnternational Workshop on Digital Content & Smart Multimedia (DCSMart)*. Lviv, Ukraine, 23–25 December 2019, pp. 292–302. (pdf) Available at: <http://ceur-ws.org/Vol-2533/paper27.pdf> [Accessed December 2021].

Verkhola, M.I. and Kalytka, M.I., 2019. Modelyuvannya ta analiz vplyvu tekhnolohichnykh parametriv na rozpodil ob'yemiv potokiv farby u farbodrukars'kiy systemi poslidovno-paralel'noyi struktury. *Modelyuvannya ta informatsiyni tekhnolohiyi,* 88, pp. 225–242. (In English: Modeling and analysis of technological parameters influence on the ink flow volume's distribution in the ink printing system of serial-parallel structure, *Modeling and Information Technologies*). http://doi.org/10.5281/zenodo.3862078.

Vlachopoulos, G., Claypole, T. and Bould, D., 2010. Ink mist formation in roller trains. In: N. Enlund and M. Lovreček, eds. *Advances in Printing and Media Technology: Proceedings of the 37th International Research Conference of iarigai*. Montreal, Canada, September 2010, pp. 227–234.

Appendix A: Data of model experiments

Table A.1: Ink thicknesses h_c^j (µm) in the j-th zones of the offset machine GTO-52, for imprints with $k_z = 1.0$

Zonal ink supply h_d (µm)	Ink splitting factor α_i															
	0.40	0.41	0.42	0.43	0.44	0.45	0.46	0.47	0.48	0.49	0.50	0.51	0.52	0.53	0.54	0.56
	Ink thickness h_c^j (µm)															
65	0.416	0.501	0.591	0.683	0.775	0.865	0.950	1.030	1.104	1.171	1.233	1.291	1.343	1.392	1.437	1.521
70	0.448	0.539	0.636	0.736	0.835	0.931	1.023	1.109	1.189	1.261	1.328	1.390	1.447	1.499	1.548	1.638
90	0.576	0.693	0.818	0.946	1.074	1.197	1.315	1.426	1.529	1.622	1.708	1.787	1.860	1.927	1.990	2.105
100	0.640	0.770	0.909	1.051	1.193	1.330	1.461	1.584	1.699	1.802	1.897	1.985	2.066	2.141	2.211	2.339
120	0.768	0.925	1.091	1.262	1.431	1.596	1.754	1.901	2.038	2.162	2.277	2.383	2.480	2.569	2.654	2.807
130	0.832	1.002	1.182	1.367	1.551	1.730	1.900	2.059	2.208	2.342	2.467	2.581	2.686	2.783	2.875	3.041
140	0.896	1.079	1.273	1.472	1.670	1.863	2.046	2.218	2.378	2.523	2.656	2.780	2.893	2.998	3.096	3.275
150	0.960	1.156	1.364	1.577	1.789	1.996	2.192	2.376	2.548	2.703	2.846	2.978	3.100	3.212	3.317	3.509
150	0.960	1.156	1.364	1.577	1.789	1.996	2.192	2.376	2.548	2.703	2.846	2.978	3.100	3.212	3.317	3.509
140	0.896	1.079	1.273	1.472	1.670	1.863	2.046	2.218	2.378	2.523	2.656	2.780	2.893	2.998	3.096	3.275
130	0.832	1.002	1.182	1.367	1.551	1.730	1.900	2.059	2.208	2.342	2.467	2.581	2.686	2.783	2.875	3.041
120	0.768	0.925	1.091	1.262	1.431	1.596	1.754	1.901	2.038	2.162	2.277	2.383	2.480	2.569	2.654	2.807
100	0.640	0.770	0.909	1.051	1.193	1.330	1.461	1.584	1.699	1.802	1.897	1.985	2.066	2.141	2.211	2.339
85	0.544	0.655	0.773	0.894	1.014	1.131	1.242	1.346	1.444	1.532	1.613	1.688	1.757	1.820	1.880	1.988
65	0.416	0.501	0.591	0.683	0.775	0.865	0.950	1.030	1.104	1.171	1.233	1.291	1.343	1.392	1.437	1.521
60	0.384	0.462	0.545	0.631	0.716	0.798	0.877	0.950	1.019	1.081	1.138	1.191	1.240	1.285	1.327	1.404

Table A.2: Distribution of ink volumes V_i (× 10^3 mm³) in the IPS
of the offset machine GTO-52, for imprints with $k_z = 1.0$

Elements IPS	Ink splitting factor α_i															
	0.40	0.41	0.42	0.43	0.44	0.45	0.46	0.47	0.48	0.49	0.50	0.51	0.52	0.53	0.54	0.56
	Ink volumes V_i (× 10^3 mm³)															
VR	0.509	0.490	0.468	0.442	0.416	0.389	0.363	0.338	0.316	0.296	0.279	0.264	0.251	0.240	0.230	0.215
1	2.143	2.149	2.104	1.956	1.906	1.749	1.622	1.464	1.282	1.242	1.118	1.042	0.958	0.853	0.814	0.693
2	1.200	1.267	1.249	1.206	1.186	1.138	1.078	1.015	1.903	0.875	0.818	0.755	0.702	0.636	0.609	0.528
3	0.898	0.961	0.980	0.988	0.987	0.971	0.943	0.907	0.843	0.818	0.771	0.723	0.678	0.629	0.595	0.520
4	0.441	0.477	0.508	0.532	0.546	0.553	0.552	0.545	0.529	0.514	0.496	0.473	0.451	0.426	0.407	0.362
5	0.342	0.383	0.422	0.457	0.484	0.504	0.518	0.524	0.528	0.522	0.514	0.503	0.489	0.474	0.457	0.423
6	0.380	0.409	0.434	0.452	0.461	0.463	0.458	0.447	0.434	0.414	0.393	0.371	0.348	0.325	0.302	0.259
7	0.263	0.269	0.299	0.327	0.350	0.368	0.383	0.392	0.398	0.399	0.398	0.394	0.388	0.380	0.371	0.351
8	0.228	0.259	0.288	0.314	0.336	0.354	0.366	0.374	0.378	0.378	0.375	0.369	0.361	0.352	0.341	0.318
9	0.396	0.437	0.472	0.500	0.519	0.530	0.534	0.530	0.520	0.505	0.487	0.466	0.443	0.420	0.396	0.350
10	0.178	0.206	0.234	0.261	0.285	0.306	0.323	0.336	0.347	0.353	0.357	0.358	0.357	0.355	0.350	0.339
11	0.163	0.191	0.219	0.247	0.272	0.296	0.316	0.334	0.350	0.360	0.360	0.376	0.381	0.385	0.385	0.386
12	0.338	0.367	0.390	0.409	0.420	0.425	0.424	0.418	0.408	0.394	0.379	0.362	0.344	0.326	0.308	0.274
13	0.246	0.279	0.310	0.337	0.361	0.379	0.392	0.400	0.404	0.404	0.401	0.396	0.388	0.379	0.368	0.345
PC	0.375	0.440	0.505	0.568	0.628	0.684	0.731	0.773	0.807	0.838	0.862	0.881	0.897	0.908	0.918	0.930
BC	0.171	0.206	0.243	0.280	0.318	0.355	0.390	0.423	0.453	0.481	0.507	0.530	0.552	0.572	0.591	0.626
IPS*	8.271	8.790	9.125	9.276	9.475	9.464	9.393	9.220	8.900	8.793	8.520	8.270	7.990	7.650	7.440	6.919
FR	11.88	11.83	11.78	11.72	11.67	11.62	11.58	11.53	11.49	11.45	11.42	11.38	11.34	11.31	11.27	11.20
IPS	20.15	20.62	20.91	20.99	21.15	21.08	20.97	20.75	20.39	20.24	19.94	19.65	19.33	18.96	18.71	18.12

Table A.3: Ink thicknesses h_c^j (µm) in the j-th zones of the offset machine GTO-52, for imprints with $k_z = 0.2$

Zonal ink supply h_d (µm)	Ink splitting factor α_i															
	0.40	0.41	0.42	0.43	0.44	0.45	0.46	0.47	0.48	0.49	0.50	0.51	0.52	0.53	0.54	0.56
	Ink thickness h_c^j (µm)															
40	0.320	0.401	0.493	0.592	0.697	0.803	0.907	1.007	1.101	1.186	1.263	1.334	1.397	1.453	1.505	1.595
50	0.400	0.501	0.616	0.740	0.871	1.004	1.134	1.259	1.376	1.482	1.579	1.667	1.746	1.816	1.881	1.994
60	0.480	0.602	0.739	0.888	1.045	1.204	1.361	1.511	1.351	1.779	1.895	2.001	2.095	2.179	2.257	2.393
70	0.560	0.702	0.862	1.036	1.220	1.405	1.588	1.763	1.927	2.075	2.211	2.334	2.444	2.543	2.633	2.792
75	0.600	0.752	0.924	1.110	1.307	1.506	1.701	1.889	2.064	2.224	2.369	2.501	2.619	2.724	2.821	2.991
80	0.640	0.802	0.985	1.184	1.394	1.606	1.815	2.015	2.202	2.372	2.527	2.667	2.793	2.906	3.009	3.190
85	0.680	0.852	1.047	1.258	1.481	1.706	1.928	2.141	2.339	2.520	2.685	2.834	2.968	3.087	3.197	3.390
100	0.799	1.003	1.232	1.480	1.742	2.007	2.268	2.519	2.752	2.965	3.159	3.334	3.492	3.632	3.761	3.988
100	0.799	1.003	1.232	1.480	1.742	2.007	2.268	2.519	2.752	2.965	3.159	3.334	3.492	3.632	3.761	3.988
85	0.640	0.852	1.047	1.258	1.481	1.706	1.928	2.141	2.339	2.520	2.685	2.834	2.968	3.087	3.197	3.390
80	0.640	0.802	0.985	1.184	1.394	1.606	1.815	2.015	2.202	2.372	2.527	2.667	2.793	2.906	3.009	3.190
75	0.600	0.752	0.924	1.110	1.307	1.506	1.701	1.889	2.064	2.224	2.369	2.501	2.619	2.724	2.821	2.991
70	0.560	0.702	0.862	1.036	1.220	1.405	1.588	1.763	1.927	2.075	2.211	2.334	2.444	2.543	2.633	2.792
60	0.480	0.602	0.739	0.888	1.045	1.204	1.361	1.511	1.651	1.779	1.895	2.001	2.095	2.179	2.257	2.393
50	0.400	0.501	0.616	0.740	0.871	1.004	1.134	1.259	1.376	1.482	1.579	1.667	1.746	1.816	1.881	1.994
40	0.320	0.401	0.493	0.592	0.697	0.803	0.907	1.007	1.101	1.186	1.263	1.334	1.397	1.453	1.505	1.595

Table A.4: Distribution of ink volumes V_i ($\times 10^3$ mm³) in the IPS
of the offset machine GTO-52, for imprints with $k_z = 0.2$

Elements IPS	Ink splitting factor α_i															
	0.40	0.41	0.42	0.43	0.44	0.45	0.46	0.47	0.48	0.49	0.50	0.51	0.52	0.53	0.54	0.56
	Ink volumes V_i ($\times 10^3$ mm³)															
VR	0.299	0.289	0.275	0.258	0.238	0.217	0.195	0.173	0.153	0.135	0.119	0.105	0.093	0.083	0.074	0.062
1	1.388	1.386	1.361	1.311	1.250	1.176	1.073	0.971	0.865	0.742	0.668	0.587	0.523	0.432	0.391	0.304
2	0.796	0.832	0.842	0.845	0.836	0.800	0.764	0.712	0.658	0.605	0.542	0.488	0.435	0.380	0.344	0.274
3	0.593	0.644	0.692	0.722	0.730	0.731	0.721	0.699	0.668	0.636	0.587	0.543	0.499	0.499	0.417	0.344
4	0.298	0.336	0.371	0.403	0.428	0.446	0.456	0.458	0.454	0.443	0.428	0.410	0.389	0.367	0.345	0.302
5	0.255	0.299	0.343	0.687	0.427	0.462	0.490	0.512	0.526	0.532	0.534	0.530	0.522	0.511	0.497	0.465
6	0.138	0.168	0.201	0.236	0.270	0.304	0.335	0.362	0.386	0.406	0.422	0.435	0.444	0.451	0.456	0.459
7	0.127	0.156	0.187	0.219	0.252	0.284	0.314	0.342	0.366	0.386	0.403	0.417	0.428	0.437	0.443	0.450
8	0.289	0.325	0.359	0.388	0.412	0.428	0.437	0.439	0.433	0.422	0.407	0.389	0.369	0.347	0.325	0.281
9	0.190	0.224	0.259	0.294	0.327	0.357	0.381	0.400	0.414	0.422	0.426	0.426	0.423	0.417	0.409	0.382
10	0.187	0.221	0.255	0.289	0.321	0.348	0.371	0.387	0.398	0.403	0.403	0.399	0.392	0.382	0.370	0.341
11	0.298	0.336	0.370	0.400	0.423	0.440	0.448	0.449	0.443	0.431	0.415	0.396	0.376	0.354	0.331	0.287
12	0.330	0.378	0.425	0.467	0.503	0.530	0.547	0.555	0.554	0.544	0.529	0.508	0.484	0.458	0.431	0.375
13	0.193	0.230	0.268	0.305	0.340	0.371	0.396	0.416	0.430	0.437	0.440	0.438	0.432	0.423	0.412	0.385
PC	0.061	0.075	0.089	0.104	0.120	0.134	0.148	0.160	0.171	0.180	0.187	0.193	0.198	0.201	0.204	0.207
BC	0.028	0.035	0.043	0.052	0.061	0.070	0.079	0.088	0.096	0.103	0.110	0.116	0.122	0.127	0.131	0.139
IPS*	5.469	5.931	6.341	6.688	6.941	7.096	7.154	7.122	7.014	6.828	6.630	6.380	6.128	5.818	5.580	5.062
FR	7.559	7.549	7.537	7.526	7.513	7.502	7.491	7.481	7.472	7.453	7.455	7.447	7.439	7.432	7.424	7.410
IPS	13.03	13.48	13.88	14.21	14.45	14.60	14.65	14.60	14.49	14.28	14.09	13.83	13.57	13.25	13.00	12.47

Appendix B: Graphical representation of model experiments
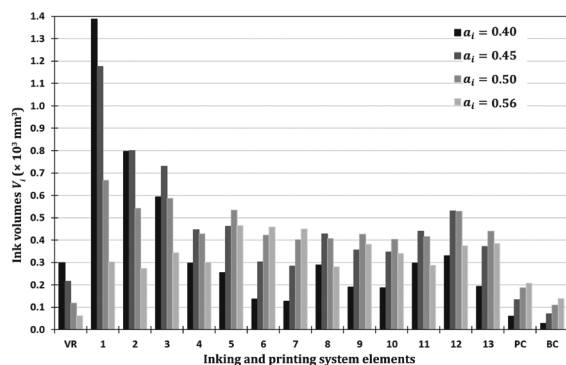
Figure B.1: Distributions of ink flow volumes in the IPS with $k_z = 0.2$ for different values of α_i

Figure B.2: Dependence of the ink volume at the surface of the roller 1 on the splitting coefficients α_i with $k_z = 0.2$

Figure B.3: Dependence of the ink volumes at the surfaces of the form rollers R_6, R_7, R_{11}, and R_{13} on the splitting coefficients α_i with $k_z = 0.2$

Figure B.4: Dependence of the ink volumes on the surfaces of the PC and BC on the factors α_i with $k_z = 0.2$

S. Ritzmann and P. Urban – J. Print Media Technol. Res. – Vol. 10 No. 4 (2021), 231–245

231

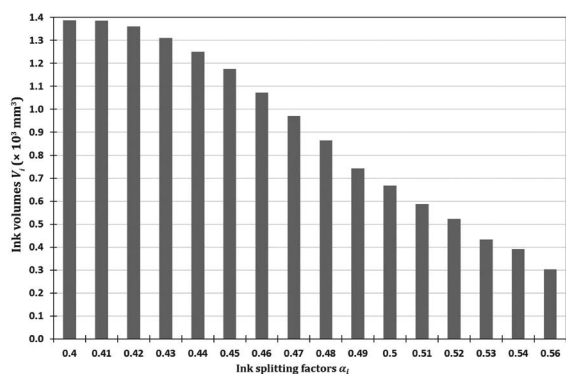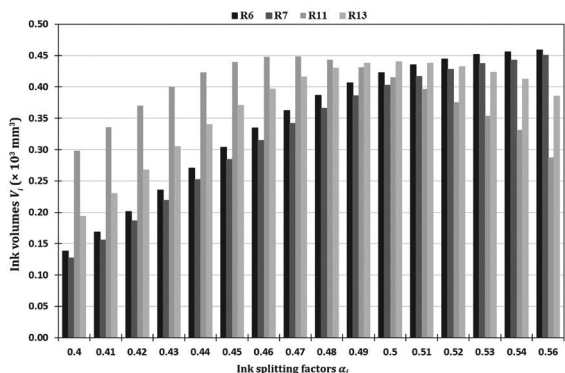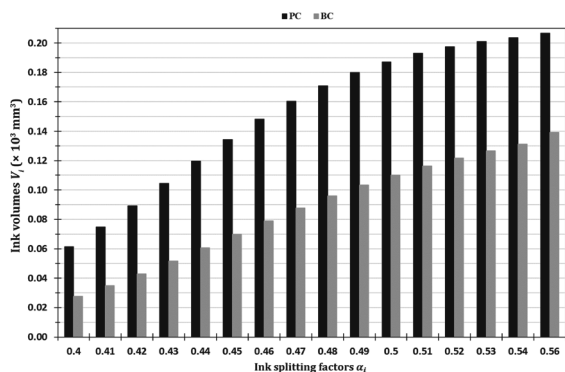# Designing the Spatial star as a three-dimensional derivate of the Siemens star and developing the methods to determine the accuracy, resolution and spatial frequency response from a 3D scan of the Spatial star

Sven Ritzmann and Peter Urban

University of Wuppertal,
School of Electrical, Information and Media Engineering,
Rainer-Gruenter-Straße 21, D.42119 Wuppertal

ritzmann@uni-wuppertal.de
purban@uni-wuppertal.de

Abstract

In many cases investigating a 3D scan of a real object is more time and cost effective than investigating the real object. This is especially the case if related objects are spread over several collections around the world. Investigation results based on a 3D scan depend on the accuracy and resolution of the specific 3D scan. This paper lays the foundation to define the specific characteristics of a workflow to determine the accuracy, resolution and spatial frequency response of any 3D scan. Therefore, it adapts the operating principle of the Siemens star to the third dimension. The result is the Spatial star, a digital three-dimensional derivate of the Siemens star that provides the required information. This paper also develops the methods to determine the accuracy, resolution and spatial frequency response from a 3D scan of the Spatial star. During this process a 3D scan is restructured into a unified matrix representation that ensures comparability between different 3D scans and fits documentation purposes. To validate the developed methods, the paper uses a set of partly simulated 3D scans of the Spatial star.

Keywords: 3D imaging, quality assessment, optical transfer function, modulation transfer function

1. Introduction

The background of this paper is a project that deals with digitization of cultural heritage items. The main purpose of the project, beneath preservation and documentation, is to ease investigations. In general, several cultural heritage items related for example in terms of era or origin are often spread over several collections all over the world. Instead of investigating related items all over the world, investigating a 3D scan of these items is less time and cost consumptive. In this case the investigation results depend on the accuracy and resolution of the investigated 3D scan. This leads to the question how the accuracy and resolution of any 3D scan can be determined to proof the relevance of such investigations.

The determination of the accuracy and resolution is of interest not only for the digitization of objects but also for the development of 3D scanning systems as well

as for the additive production of objects. Therefore, a more generalized concept was designed that is shown in Figure 1.

This concept includes three workflows for investigating 3D scanning systems (respectively 3D scans), 3D scanning algorithms and 3D printers. The first of the two key processes (filled in grey) in each workflow is a digital test element that provides information like accuracy, resolution and the spatial frequency response (SFR). The second key process determines this information from a 3D scan of the test element compared to a reference. The intervening processes vary depending on the system under test. A 3D scanning system under test digitizes a physical copy of the test element. Both the system producing the physical test element and the 3D scanning system that creates the reference must have a higher resolution capacity than the system under test. A 3D scanning algorithm under test processes a set of corresponding ground
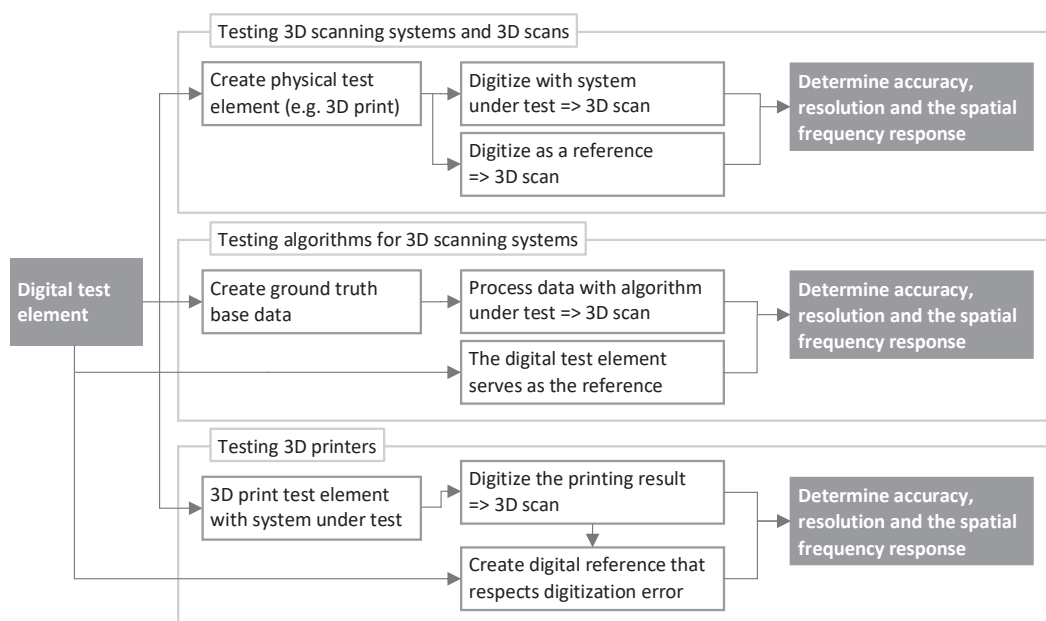
```
┌─ Testing 3D scanning systems and 3D scans ──────────────────────────────┐
│  ┌──────────────────┐   ┌──────────────────┐   ┌──────────────────┐     │
│  │ Create physical  │→  │ Digitize with    │   │ Determine        │     │
│  │ test element     │   │ system under     │→  │ accuracy,        │     │
│  │ (e.g. 3D print)  │   │ test => 3D scan  │   │ resolution and   │     │
│  └──────────────────┘   └──────────────────┘   │ the spatial      │     │
│                         ┌──────────────────┐   │ frequency        │     │
│                         │ Digitize as a    │   │ response         │     │
│                         │ reference        │   └──────────────────┘     │
│                         │ => 3D scan       │                            │
│                         └──────────────────┘                            │
└─────────────────────────────────────────────────────────────────────────┘
```

Digital test element

```
┌─ Testing algorithms for 3D scanning systems ────────────────────────────┐
│  ┌──────────────────┐   ┌──────────────────┐   ┌──────────────────┐     │
│  │ Create ground    │→  │ Process data     │→  │ Determine        │     │
│  │ truth base data  │   │ with algorithm   │   │ accuracy,        │     │
│  └──────────────────┘   │ under test       │   │ resolution and   │     │
│                         │ => 3D scan       │   │ the spatial      │     │
│                         └──────────────────┘   │ frequency        │     │
│                         ┌──────────────────┐   │ response         │     │
│                         │ The digital test │   └──────────────────┘     │
│                         │ element serves   │                            │
│                         │ as the reference │                            │
│                         └──────────────────┘                            │
└─────────────────────────────────────────────────────────────────────────┘
```

```
┌─ Testing 3D printers ───────────────────────────────────────────────────┐
│  ┌──────────────────┐   ┌──────────────────┐   ┌──────────────────┐     │
│  │ 3D print test    │→  │ Digitize the     │→  │ Determine        │     │
│  │ element with     │   │ printing result  │   │ accuracy,        │     │
│  │ system under     │   │ => 3D scan       │   │ resolution and   │     │
│  │ test             │   └──────────────────┘   │ the spatial      │     │
│  └──────────────────┘   ┌──────────────────┐   │ frequency        │     │
│                         │ Create digital   │   │ response         │     │
│                         │ reference that   │   └──────────────────┘     │
│                         │ respects         │                            │
│                         │ digitization     │                            │
│                         │ error            │                            │
│                         └──────────────────┘                            │
└─────────────────────────────────────────────────────────────────────────┘
```

Figure 1: Three conceptional workflows to determine the accuracy, resolution and spatial frequency response of 3D scanning systems and their algorithms, 3D scans and 3D printers

truth base data created from the digital test element. In this workflow the digital test element serves as a reference without any modifications. A 3D printer under test prints the test element. A 3D scanning system with a higher resolution capacity than the system under test digitizes the printing result. To obtain the reference the digital test element is modified with respect to the digitization error of the used 3D scanning system.

The implementation of these workflows raises further questions about the characteristics of the processes. For example, to what degree the resolution capacity of a 3D scanning system has to be beyond the resolution capacity of the system under test? How to precisely produce a physical copy of the test element? How to define a ground truth dataset for several 3D scanning algorithms? Do the computed accuracy and resolution match with the human perception?

To investigate and define these characteristics and to finally implement the workflows the two key processes have to be defined in advance. Therefore, this paper introduces a digital test element that provides information like accuracy, resolution and SFR, and develops a process to determine this information from a 3D scan of the test element. Due to its importance for each workflow and for the mentioned project this paper exclusively deals with 3D scanning and neglects 3D printing.

In general, several 3D scanning systems and methods are able to digitize 3D objects and surfaces. These methods are divided in active and passive methods (Brünger, et

al., 2020). Drouin and Beraldin (2020) offer an in-depth insight into active 3D scanning methods. Simplified, these methods influence the scenery by projecting a light pattern with a known geometry (Figure 2a). Depending on its shape an object in the scene distorts the projected light pattern (Figure 2b). The comparison between the distorted and the undistorted light pattern leads to the reconstruction of the three-dimensional shape. A simple implementation of an active 3D scanning system includes a projector projecting a single line, a camera capturing the distortion of the projected line and a software reconstructing the depth information of the points along the line. To obtain a 360° reconstruction the object can be rotated along its central axis. The resulting points are stitched together to form a point cloud representation of the object.
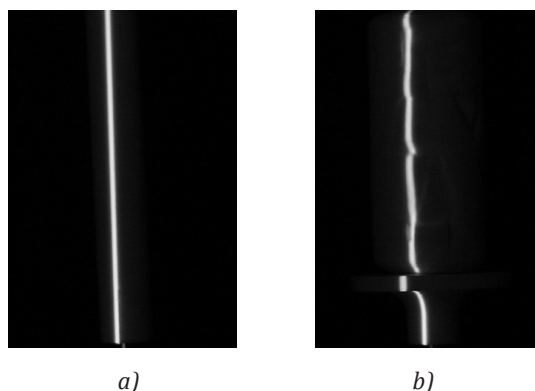

a)   *b)*

Figure 2: A line as a simple light pattern for an active 3D scanning system (a), is distorted by the shape of the 3D scanning object (b)

Contrary, passive 3D scanning methods do not influence the scene. Se and Pears (2020) offers a comprehensive description of several passive 3D scanning methods. Photogrammetry is a multi-view approach and an example for a passive 3D scanning method. A camera captures images of a scene from at least two viewpoints. A photogrammetry software detects matching features between the images (Figure 3a) and reconstructs a point in a 3D space for each feature match based on the change in perspective (Figure 3b). The resulting point cloud represents the scene. A 3D scanning system based on photogrammetry includes at least one camera and a photogrammetry software. To obtain a 360° view the relative position between the camera and scene changes after each image. Alternatively, multiple cameras are placed around the scene.

In summary most 3D scanning systems utilize at least one camera or combine a camera with a projector. The accuracy and resolution of these components can be determined by using several methods.

Despite, it is not sufficient to know the accuracy and resolution of the used components to determine the accuracy and resolution of the 3D scanning system. Besides its components different factors influence these properties.

The result of a photogrammetry scan depends, among other things, on the camera movement between each image. The accuracy of an active 3D scanning system is influenced by the relative position of the camera to the projector and by the used pattern. Furthermore, several material properties of a 3D scanning object cause problems as well (Guidi and Frischer, 2020). For example, translucent materials scatter and distort a projected light pattern or the ambient light that is needed for any camera to work. Reflective and shiny materials also cause several reconstruction errors as they distort the light.

Although it is not sufficient to know the accuracy and resolution of the components the test elements used to determine this information can be adapted to the third dimension. One of these test elements to determine the accuracy, resolution and SFR of cameras, 2D scanners and 2D printers is the Siemens star (Loebich, et al., 2007; International Organization for Standardization, 2017). This paper adapts the operating principle of the Siemens star to the third dimension. The result is the digital Spatial star that fulfills the requirements of the digital test element and thus of the first key process of the workflows shown in Figure 1.

Since the second key process compares an actual 3D scan with a reference 3D scan, the comparability between different 3D scans of Spatial stars is mandatory. As discussed before most 3D scanning methods produce a point cloud representation of an object. Ideally the points are positioned on the object surface. Between two scans, even with the same 3D scanning system, the point positions on the surface differ. Therefore, it is unlikely that a specific point in one 3D scan has a corresponding point with the same position in the other 3D scan. This paper solves the problem by restructuring the 3D scan of a Spatial star into a unified matrix representation (UMR). The development of the second key process is finished with the methods extracting the accuracy, resolution and SFR from the UMR. As the UMR includes all required information it is also used for documentation purposes.

2. The research approach

2.1 Definition of terms

As discussed in the introduction the accuracy and resolution of a 3D scanning system do not equal the accuracy and resolution of its components. It rather depends on different influencing factors that differ between different 3D scanning systems and scanning methods.

a)   b)
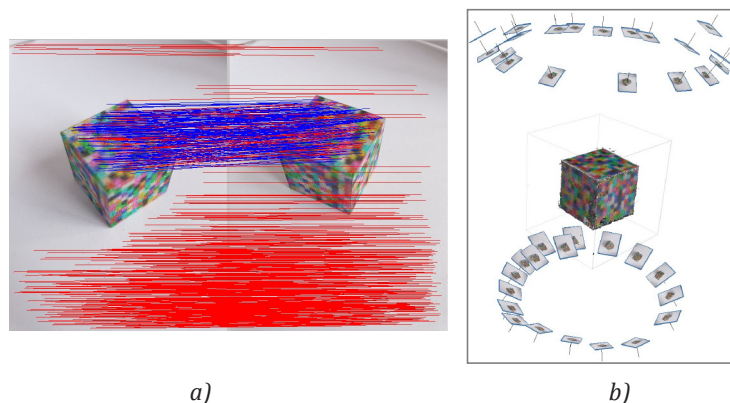
Figure 3: An example of a photogrammetry based 3D scan: the feature matches between two images are visualized with lines (a), the reconstructed object is surrounded by the reconstructed cameras (b)

To simplify the context between accuracy, resolution and influencing factors this paper refers to the combination of every influencing factor that is given by the scanning scenario as the 3D scanning system. It further refers to every influencing factor that is brought into this system as the 3D scanning object.

This paper defines a 3D scan as the result of the digitization process performed by a 3D scanning system. The accuracy of a 3D scanning system describes the maximum possible match of a reproduction and an ideal 3D scanning object where the ideal 3D scanning object has no influence on the 3D scanning system. The accuracy of a 3D scan on the other hand describes the degree a 3D scan actually matches a given 3D scanning object.

This paper describes the resolution capacity of a 3D scanning system as its ability to distinguish details. The resolution of a 3D scan is defined as the distinguishable height differences per length (later referred to as DHD value, expressed as dhd/cm).

2.2　The Siemens star and its operating principle

The Spatial star adapts the main operating principle from the Siemens star. The Siemens star is a 2D test chart to determine the resolution of cameras and 2D scanners. It consists of elongated triangular black spokes on a white ground arranged in a circle with a fixed angle to each other (Figure 4a). The angle is chosen so that the white space between two spokes has the same shape and size as one spoke. As the spokes get narrower towards the center the Siemens star represents (in theory) every spatial frequency between infinite and the frequency given by the outer radius. The spatial frequency is defined (Birch and Griffin, 2015) by the number of pairs of black and white spokes or cycles along the circumference of a given radius (Equation [1]).

a)　　　　　*b)*　　　　　*c)*
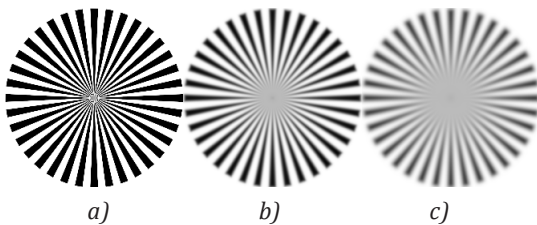
Figure 4: Three Siemens stars with 36 cycles and from the center increasing areas of no contrast due to the decreasing resolution

$$f_s = \frac{c_n}{2\,\pi\,r} \qquad\qquad [1]$$

where f_s represents spatial frequency, c_n is the number of cycles and r is the radius that corresponds to the spatial frequency.

For the increasing spatial frequency, the closer the spatial frequency is to the resolution capacity of the camera or the 2D scanner under test, the higher is the loss in contrast for the reproduction result. Spatial frequencies that exceed the resolution capacity form a circular area of no contrast around the center of the reproduced Siemens star (Figures 4b, and 4c). The radius of this area leads to the spatial frequency that corresponds to the resolution capacity of the device under test.

2.3　Determination of the SFR of a Siemens star

As a part of ISO 12233:2017 (International Organization for Standardization, 2017) the Siemens star is used to determine the SFR of a camera or 2D scanner. This function is a tool to analyze the contrast (respectively the response) over the spatial frequency. Loebich, et al. (2007) show how to process a reproduction of a sinusoidal Siemens star. As a part of this they determine the SFR. To compute the needed contrast, they fitted a sine function into the measurement data along the circumference of a specific radius by using the least squares method. The result is an approximation of the actual offset and amplitude that is used to calculate the contrast for the corresponding spatial frequency.

2.4　Determine the resolution of a Siemens star

In relation to the SFR, the resolution is the spatial frequency for a specific contrast. Perceptual wise this contrast is given by the outer radius of the area around the center of a reproduced Siemens star. To determine the resolution Loebich, et al. (2007) refer to Williams (2004 cited in Loebich, et al., 2007) who used the R10 criterion by Lord Rayleigh to define the smallest distinguishable contrast. As a result, they define the limiting resolution as the spatial frequency where the SFR reaches 10 % of the contrast. In this paper the same value is used as a comparison to the calculated DHD.

2.5　Preference of the Siemens star over the slanted edge method

While the Siemens star is a sine-based method for SFR measurement, the ISO 12233:2017 (International Organization for Standardization, 2017) also refers to an edge-based SFR measurement. Here the system under test captures a slanted edge. The transition in intensity from the edge to the background leads to the edge spread function which shows the pixel intensity over the pixel position. The derivate of the edge spread function is the line spread function. To obtain the SFR the line spread function is transferred into the Fourier domain (Masaoka, 2018). Goesele, Fuchs and Seidel (2003) transferred the slanted edge method into the third dimension to determine the SFR of laser scanners.

Due to two reasons this paper prefers the Siemens star as a starting point. Firstly, contrary to the slanted edge method the Siemens star allows a visual interpretation. Secondly, most 3D scanners rely on motion to achieve a 360° view. Therefore, the test element has to cover angle dependencies. Contrary to the slanted edge the circular arrangement of the Siemens star covers a wide range of angles. Furthermore, every spoke of the Siemens star (and of the Spatial star) can be seen as a slanted edge with which it keeps the possibility to implement the slanted edge method.

2.6 Used software and frameworks

The Spatial star is designed in OpenSCAD version 2021.01 (Kintel, 2021). The Spatial star processing and visualization software (SSPV) is written in Python and uses different frameworks like NumPy version 1.19.2 (Harris, et al., 2020) and SciPy version 1.6.1 (Virtanen, et al., 2020) for scientific computing, Pandas version 1.2.1 (McKinney, 2010) for data analysis and processing, Open3D version 0.11.2 (Zhou, Park and Koltun, 2018) for handling 3D files and Matplotlib version 3.3.2 (Hunter, 2007) for creating visualizations. Furthermore, Blender version 2.92.0 (Blender Online Community, 2021) is used to visualize the digital Spatial star and the 3D scans. Blender is also used for simulation purposes. For testing purposes, the standard edition of the photogrammetry software Metashape version 1.7.3 (Agisoft, 2021a), CloudCompare version 2.11 alpha (CloudCompare, 2021) and ExifTool version 12.32 (Harvey, 2021) are used. Cloud Compare is also used to visualize point clouds.

2.7 Creating sample data for visualization and validation purposes

The design of the digital Spatial star and the methods to determine the accuracy, resolution and SFR from any 3D scan of a Spatial star are described in general terms in section 2.8 and 2.9. Despite the general description, most of the figures and the validation in section 3 are based on partly simulated 3D scans of a digital Spatial star with a defined geometry.

Figure 5 visualizes the dimensions of the digital Spatial star used. It shows a top view of the star like arrangement (top left) of 30 elements, with four points per element, a radius of 25 mm and a height of 5.24 mm. For a better overview it is excluded from the outer body (top center). For orientation and alignment purposes the outer body has a cut-out mark on its left side. The fusion of both forms the digital Spatial star used in this paper (top right). Due to the fusion and the slope on the inside of the outer body, the maximal element height (height difference) of 3.83 mm is given by $r_{max.hd}$ with 18.26 mm (Figure 5). The bottom row shows a side view of the star like arrangement (left) and of a section through the outer body (right). The white lines visualize the terms element (1), cycle (2), and element width (3) which equals the element height (4). The digital Spatial star is programmed in OpenSCAD. The parameters of the Spatial star are adaptable variables. The digital Spatial star is saved as STL file that describes an object with triangular areas each defined by three points (Kai, Jacob and Mei, 1997). Since the relevant points of the star like arrangement are set and
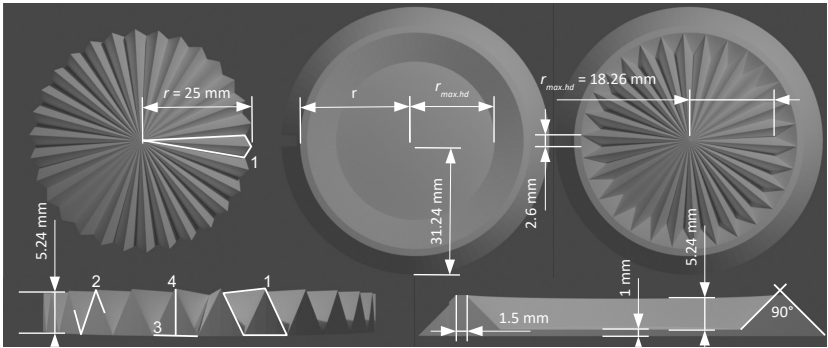

Figure 5: The dimensions of the digital Spatial star and the related terms: element (1), cycle (2), element width (3) and element height (4) as used in this paper
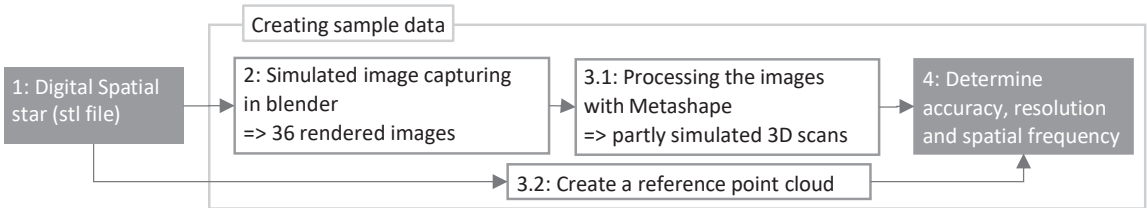

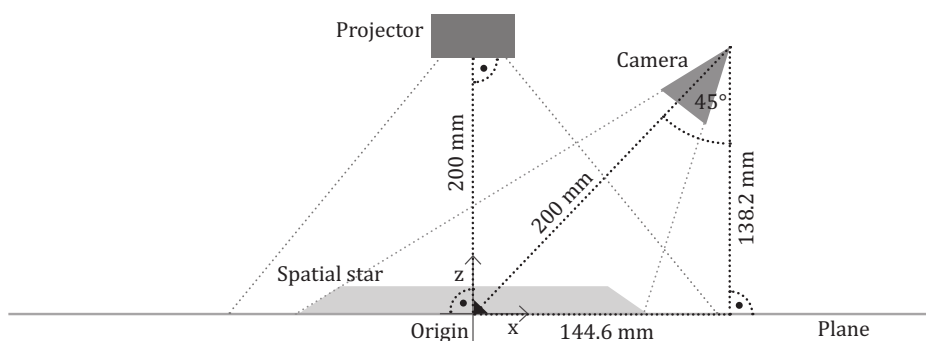
Figure 6: The workflow for creating sample data

Figure 7: The arrangement in Blender to simulate the image capturing

connected to triangles as described in section 2.8 the accuracy of the digital Spatial star equals the accuracy of a double floating-point number.

The digital Spatial star is the starting point of the workflow for creating sample data as shown in Figure 6. The processes 2 and 3.1 represent a photogrammetry based 3D scanning system. While the processing is performed in Metashape as for a real set of images the preceding image capturing is simulated in Blender.

Figure 7 visualizes the arrangement used in Blender. In this scenario the digital Spatial star is the 3D scanning object. The color of the digital Spatial star is white ($R = G = B = 1.0$) and its surface is set to the parameter diffuse bidirectional scattering distibution function (BSDF). Its bottom center is placed at the origin. The 3D scanning system includes the camera, the projector and a plane. The plane has the same surface and color as the digital Spatial star and serves as a base.

The simulated camera captures images with a size of 6 000 × 4 000 px. The focal length is set to 100 mm and the F-Stop value is set to 128.0. For the other camera settings, the default values remain unchanged. During the capturing process, the camera rotates 10 degrees around the *z*-axis after each image. The images are rendered to disk using the cycles renderer with the default settings. The projector projects an image that shows gray scaled pixel noise with a Gaussian distribution onto the digital Spatial star to create a high number of features. Therefore, the projector is not used as for an active 3D scanning method. During the image capturing, the projector remains static.

Figure 8 shows one of the 36 images of the digital Spatial star created during the simulated capturing process. These images are lacking meta data. Since Metashape uses metadata such as focal length and sensor pixel size for its internal processes (Agisoft, 2021b) these data have to be added. Therefore, ExifTool is used to copy the meta data from a reference image to each of the simulated images. The reference image is captured

using a Canon Eos 750d (Canon Deutschland GmbH, 2021) with the same focal length and image size as the simulated camera.
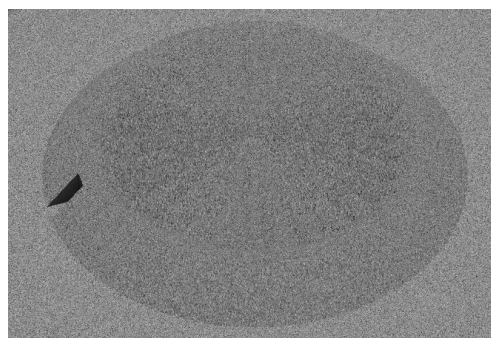

Figure 8: One of the 36 simulated images of the Spatial star

Metashape processes these images into a point cloud representation and thus into a 3D scan of the Spatial star. To obtain four 3D scans the quality parameter for the dense cloud processing is switched between high, medium, low and lowest. This scales the images to the size of 3 000 × 2 000 px for high, 1 500 × 1 000 px for medium, 750 × 500 px for low and 375 × 250 px for lowest. As defined in section 2.1, this procedure corresponds to using four 3D scanning systems. The parameter depth filtering is set to aggressive. For the other settings the default values remain unchanged. The four resulting partly simulated 3D scans are saved as a ply file. Points outside the reconstructed Spatial star are removed.

The reference point cloud mentioned in process 3.2 (Figure 6) is calculated in Cloud Compare. The function sample point cloud on mesh distributes 10 million points on the surface of the digital Spatial star. This reference point cloud is also saved as a ply file.

The software described in section 2.9 processes the partly simulated 3D scans and the reference point cloud to determine the accuracy, resolution and SFR. The discretization step length (STP) for computing the UMR (section 2.9.1) is set to 0.025 mm and is only

changed to show the influence of different values on the SFR (section 3). The non-tolerable error (NTE) for computing the accuracy UMR (section 2.9.4) is set to 0.05 mm and is twice as high as the STP value. This value is chosen arbitrarily as the STP value is determined by the requirements of the specific use case.

The discrete reference cross section used in sections 2.9.1 and 2.9.3 is calculated using Equations [2] to [14] with a radius of 18.26 mm, 30 elements, 4 points per element and a discretization step of 0.025 mm.

The figures in section 2 are exemplary and use the partly simulated 3D scan generated in Metashape with the medium quality parameter (Figures 11, 12, 18, 19, 20, 21), the reference point cloud (Figures 13, 14, 15, 17) and the discrete reference cross section (Figures 10, 12, 19).

2.8 Design of the Spatial star

The Spatial star is a digital 3D derivate of the Siemens star. The requirements influencing the designing process and the transformation from a planar graphical element to the 3D specimen exemplary shown in Figure 9 are discussed as well as the way a 3D scanning system distorts the Spatial star.
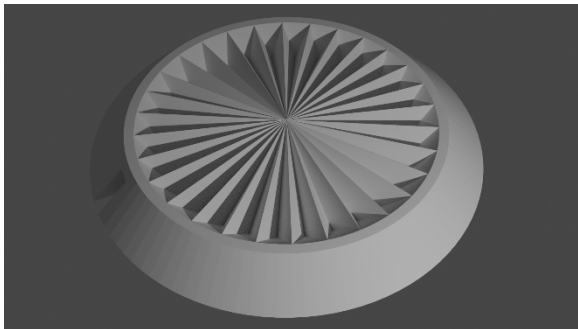
Figure 9: Example of a Spatial star with 30 cycles

The Spatial star is a crucial part to determine the accuracy and SFR of any 3D scanning system and 3D scan. Therefore, its structure has to provide this information and has to be compatible with a wide range of 3D scanning systems. Strongly simplified every 3D scanning system measures the distance to the scene points based on at least two known positions defined by its main components. Depending on the used method these components are at least one camera or one camera and one projector. Correspondingly, the surface of the Spatial star has to be completely visible to both kind of devices.

As a digital derivate of the Siemens star the Spatial star has to adapt its operating principle. Therefore, its structure has to represent an increasing spatial resolution towards its center.

Since most 3D scanning systems rely on motion to achieve a 360° view of a scene the motion path influences the 3D scan. Therefore, the Spatial star has to represent the influence of the relative position between the motion path and a structure element.

These requirements lead to the structure of the Spatial star. Its main part is a circle consisting of elements getting narrower towards the center. This is a similar layout to the Siemens star. To achieve spatiality the elements are based on a sine function. The sine function is applied perpendicular along the circumference of a circle. Every cycle proceeds along a definable number of data points. The height of one element is the same as its width. These descriptions are represented by Equations [2] to [4]:

$$p_i = \begin{pmatrix} p_x \\ p_y \\ p_z \end{pmatrix} = \begin{pmatrix} r \times \sin\left(360 \times \dfrac{i}{p_n}\right) \\ r \times \cos\left(360 \times \dfrac{i}{p_n}\right) \\ h \times 0.5 \times \left(\sin\left(360 \times e_n \times \dfrac{i}{p_n}\right) + 1\right) \end{pmatrix} \quad [2]$$

with $i = \{1, \dots, p_n\}$

$$h = \frac{2\,\pi\,r}{e_n} \quad\quad [3]$$

$$p_n = e_n \times p_{n.data} \quad\quad [4]$$

with $p_{n.data} = \{x | x \geq 2 \times k\}$

with $k = \{2, 3, \dots\}$

where p_i is the i-th point along the circumference defined by p_x, p_y, p_z; r is the radius, h is the height for each element at radius r, e_n is the number of elements, p_n is the number of points along the circumference, and $p_{n.data}$ is the number of data points per element.

To represent increasing spatial frequencies each two consecutive points along the sine function form a triangular area with the center point p_c. The height of p_c is given by the outer radius and Equation [3]. Therefore, the highest point of the circumferential cross section of each radius lies in the same plane. As the radius decreases the element width and height also decreases, while the spatial frequency increases.

As a result, for each radius the circumferential cross section has the same shape, but differs in length and height. The shape approximates the sine function to a degree defined by $p_{n.data}$. In this paper $p_{n.data}$ equals four to adapt the operating principle of the Siemens star (see section 2.8.1). This leads to a triangular shaped circumferential cross section as in an example shown in Figure 10.
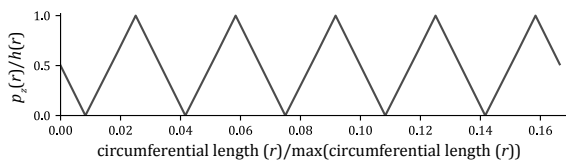
Figure 10: A Portion of the ideal circumferential cross section

Consequently, each radius corresponds to DHD as shown in Equation [5]. The DHD value defines the 3D resolution of a 3D scan. Its reciprocal value indicates the spatial dimension of the smallest detail.

$$\text{DHD} = \frac{1}{h} \qquad\qquad [5]$$

Furthermore, every relevant point of the Spatial star can be seen by a camera or projector with a perpendicular view from above. This complies the compatibility with a wide range of 3D scanning systems. Due to the circular arrangement each element meets a linear motion path in a different angle. This is sufficient to represent the influence of the relative position of the 3D scanning object to the motion path.

Finally, the star like arrangement of the Spatial star is surrounded by an outer body as in an exemple shown in section 2.7.

2.8.1 Adapting the operating principle of the Siemens star

Depending on its resolution capacity a 3D scanning system distorts the ideal Spatial star. The distortion rounds off the corners of the triangular shaped circumferential cross sections. This effect is used to adapt the operating principle of the Siemens star.

The spatial frequencies that exceed the resolution capacity of a 3D scanning system form a circular area around the center of the reproduced Spatial star (an exemple shown in Figure 11).
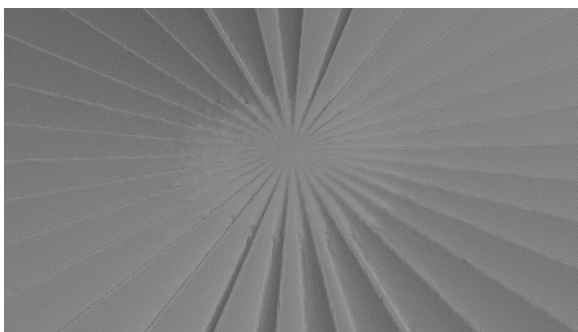
Figure 11: The circular area around the center of a partly simulated 3D scan of the Spatial star

This behavior is the same as for the Siemens star and therefore expected and desired. Equivalent to the Siemens star the outer radius of this circular area corresponds to the first radius that distinguishes the correct number of height differences. The DHD value of a 3D scan is calculated with this radius.

Contrary to the Siemens star a 3D scanning system distorts the corners of the circumferential cross sections of the Spatial star. Every upper and lower corner is, in theory, an ideal sharp tip. A 3D scanning system rounds off the part of a corner that exceeds its resolution capacity. The ratio of this part to the corner increases with the spatial frequency. If this part completely occupies the corner, the 3D scanning system is not able to reproduce the corresponding height difference. Figure 12 shows the circumferential cross section for two radii of the same partly simulated 3D scan to visualize this effect.
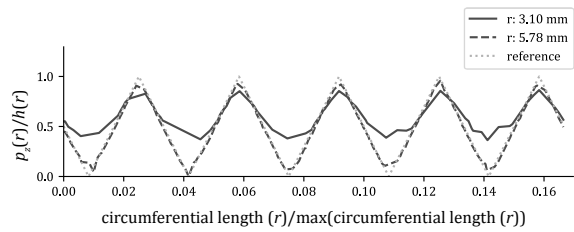

Figure 12: The corners of different circumferential cross sections of a partly simulated 3D scan in comparison

In summary the Spatial star represents the resolution of a 3D scan independently of the spatial direction. Its structure utilizes the system specific rounding off of corners in analogy to the operating principle of the Siemens star.

2.9 Processing a 3D scan of the Spatial star

To process the information of a 3D scanned Spatial star and thus to implement the second key process the SSPV is developed. Its first purpose is to restructure the information of a 3D scan of the Spatial star into a UMR. Its second purpose is to determine the accuracy, resolution and SFR based on the UMR.

2.9.1 The unified matrix representation of a 3D scan of the Spatial star

The UMR ensures the comparability between different 3D scans of Spatial stars with the same number of elements while preserving all required information. To create the UMR the SSPV processes point clouds. For most 3D scanning systems point clouds are the raw scanning result whereas triangle meshes include further computations and algorithms.

In preparation of the UMR creation process, a 3D scan of the Spatial star has to be scaled to the size of its template. Orientation-wise it has to lie on its bottom. The star like arrangement has to face up in positive z direction. The mark in the frame has to point to the negative x direction.

To create the UMR, SSPV needs information about the 3D scanned Spatial star. This includes the maximum height difference and the corresponding radius as well as the number of elements. Another needed parameter is the discretization step length STP as SSPV unified the information by discretizing the radii and circumferential length. The actual processing is initiated by transforming each point of the 3D scan as shown in Equations [6] to [9].

$$p_{\text{transformed}} = \qquad\qquad\qquad [6]$$

$$\begin{pmatrix} p_x \times \sin(-\alpha) + p_y \times \cos(-\alpha) + \alpha \times N_{xy} \times s_x \\ p_x \times \cos(-\alpha) - p_y \times \sin(-\alpha) \\ p_z \times s_z \end{pmatrix}$$

$$\alpha = \arctan2(p_y, p_x) \qquad\qquad [7]$$

$$N_{xy} = \sqrt{p_x^2 + p_y^2} \qquad\qquad [8]$$

$$s_x = s_z = \frac{r_{\text{max.hd}}}{N_{xy}} \qquad\qquad [9]$$

where $p_{\text{transformed}}$ corresponds to the point defined by (x,y,z) after transformation; α is the angle between a point projected on the x,y plane $p(x,y)$ and $p(1,0)$ [rad]; p corresponds to a point $p(x,y,z)$ as a part of the point cloud; s_i is scaling factor in i direction; N_{xy} is the Euclidean norm of any point $p(x,y)$; and $r_{\text{max.hd}}$ is the radius that corresponds to the maximum height difference.

While Figure 13 shows a top view of a partly simulated 3D scan, Figure 14 visualizes its transformation by Equation [6] without scaling ($s_x = s_z = 1$). Due to the transformation each point on a specific circumference now lies on a straight line. Figure 15 shows the transformation by Equation [6] with s_x and s_z calculated by Equation [9]. As a result, the linearized circumferential length is the same for each radius, while the height of each point is normalized to the height given by $r_{\text{max.hd}}$.

As SSPV uses depth maps the height is represented by gray scales, where white represents the highest and black the lowest point. It has to be mentioned that areas with no points are also black. For orientation purposes the visualizations in Figures 13 to 15 are subdivided in eight areas that are delimited by dashed lines.
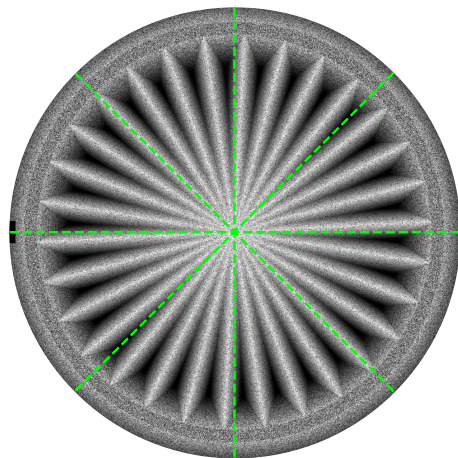

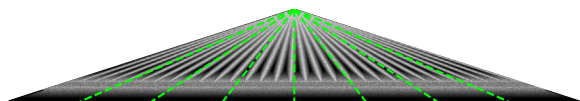*Figure 13: Top view with grey scaled height of a partly simulated 3D scan of the Spatial star*

Figure 14: The points of a partly simulated 3D scan of the Spatial star transformed by Equation [6] with $s_x = s_z = 1$
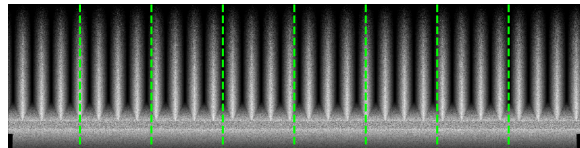

Figure 15: The points of a partly simulated 3D scan of the Spatial star transformed by Equation [6] with s_x and s_z calculated by Equation [9]

Due to the transformation the radius corresponds to the y coordinate while the circumferential length corresponds to the x coordinate and the height corresponds to the z coordinate of a transformed point. The transformation process simplifies the circumferential cross sections of a 3D scan of the Spatial star to linear cross sections and eases further calculations and processes. The scaling allows a direct comparison of circumferential cross sections with originally different length and height.

For a point cloud it is unlikely to have a sufficient number of points that lie exactly on a specific radius and circumferential length. To ensure a point-by-point comparison between different cross sections and 3D scans, SSPV implements the discretization process. The process shifts every transformed point to a specific discrete radius and circumferential length given by a multiple of discretization step length STP (Equation [10]). The `ceil` function of NumPy is used since it is less

time consuming than the `round` function. However, the `ceil` function causes a larger shifting error. This shifting error affects the point height. Due to the scaling process each radius has the same height difference, so that the radius shift has no effect. The circumferential shift on the other hand translates a point along the cross section in positive *x* direction. This shift causes when considering Equation [3] a maximum error in height that is two times the STP value. The SSPV adjusts the point height by utilizing a discrete ideal reference cross section (Equations [10] to [14]). Figure 16 visualizes the shifting, the shifting error and the adjustment.

$$p_d = \begin{pmatrix} \text{ceil}\left(\dfrac{p_{\text{transformed.x}}}{\text{STP}}\right) \\ \text{ceil}\left(\dfrac{p_{\text{transformed.y}}}{\text{STP}}\right) \\ p_{\text{transformed.z}} * s_{\text{z.CL}} \end{pmatrix} \qquad [10]$$

$$\text{CL} = \frac{p_{\text{transformed.x}}}{\text{STP}} \qquad [11]$$

$$s_{\text{z.CL}} = \frac{h_{\text{ref}}(\text{CL}_{\text{ceil}})}{h_{\text{ref}}(\text{CL})} \qquad [12]$$

$$\text{SLP} = h_{\text{ref}}(\text{CL}_{\text{ceil}}) - h_{\text{ref}}(\text{CL}_{\text{floor}}) \qquad [13]$$

$$h_{\text{ref}}(\text{CL}) = \qquad [14]$$
$$\begin{cases} (\text{CL} - \text{CL}_{\text{floor}}) \times |\text{SLP}| + h_{\text{ref}}(\text{CL}_{\text{floor}}) & \text{if SLP} \geq 0 \\ (\text{CL}_{\text{ceil}} - \text{CL}) \times |\text{SLP}| + h_{\text{ref}}(\text{CL}_{\text{ceil}}) & \text{if SLP} < 0 \end{cases}$$

where p_d is a point with discretized radius and circumferential length; $p_{\text{transformed}}$ is calculated according to Equation [6]; $s_{\text{z.CL}}$ is transformation factor to correct the circumferential length shifting error; $h_{\text{ref}}(x)$ is discrete reference cross section height at circumferential length *x*; CL is circumferential length, CL_{floor} and CL_{ceil} depicted circumferential length floored or ceiled; and SLP is slope.
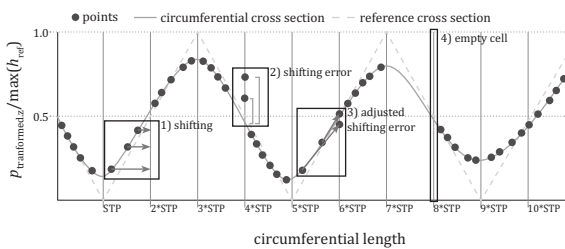

Figure 16: Visualization of the shifting (1), the shifting error (2), the adjusted shifting error (3) and empty cells (4)

The result of transforming, scaling and discretizing the point cloud is a matrix. Each matrix row represents a discrete radius (given by a number of row × STP), while each column stands for a discrete length (given

by a number of column × STP) on the scaled circumference. The matrix cells hold the mean value of the height of every point shifted to the corresponding row and column. As the cross sections decrease in length and height towards the center smaller radii tend to be represented by less points. The scaling spreads those points over a longer distance. As a consequence, the matrix has empty cells (4 in Figure 16). SSPV fills these empty cells by using linear interpolation (Figure 17).
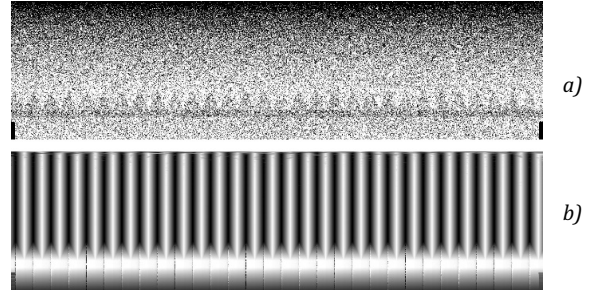

Figure 17: Visualization of empty cells (black) between the data points (white) (a), and the corresponding depth map after interpolating the empty cells (b)

After the interpolation the matrix gathers all required information provided by the 3D scan. This matrix is the UMR of a 3D scan of the Spatial star. The advantage of this representation is the point-by-point comparability between different 3D scans of Spatial stars with the same parameters.

2.9.2 Determining the distinguishable height differences of a 3D scan

Figure 18 visualizes the UMR of a partly simulated 3D scan. The area of low contrast at the top of the UMR represents the circular area of spatial frequencies that exceed the resolution capacity of the 3D scanning system. The first row with a visible alternating change in gray tones corresponds to the radius whose circumferential cross section distinguishes the correct number of elements.
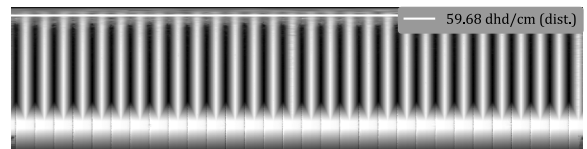

Figure 18: Visualization of the unified matrix representation of a partly simulated 3D scan (the line marks the first row that distinguishes the correct number of height differences)

To determine this row the SSPV utilizes the median function, translation and counting. For every matrix row SSPV calculates the median of the corresponding cells. The median is translated to the median of a dis-

S. Ritzmann and P. Urban – J. Print Media Technol. Res. – Vol. 10 No. 4 (2021), 231–245

241

cretized reference circumferential cross section. As a result, each cross section has the same baseline. The SSPV counts the changes around the baseline and compares the result to the number of elements of the used Spatial star. The first row with the correct number of changes corresponds to the radius of interest. The DHD are calculated as shown in Equation 5.

2.9.3 Determining the spatial frequency response

As discussed before, the determined value of the DHD reduces the resolution of a 3D scan to a single value. In comparison, the SFR is a more analytical approach. In the case of the Siemens star the SFR shows the contrast over the spatial frequency. For a 3D scan of the Spatial star the spatial frequency corresponds to the DHD value while the contrast corresponds to the reproduced height. Due to the scaling in height the theoretical height of the UMR is as the theoretical contrast of the Siemens star the same for each radius. Accordingly, the SSPV has to determine the actual reproduced height for each radius to determine the SFR.

$$f_{opt} = CS_{ref} \times s - CS_{actual} \qquad [15]$$

where f_{opt} is a function to optimize, CS_{ref} is reference cross section, CS_{actual} is measured cross section, and s is scaling factor.

Therefore, SSPV simplifies the method shown by Loebich, et al. (2007) (see section 2.3) and uses a discretized reference cross section and a scaling factor instead of a sine function. The baselines of the reference and the measured cross section are shifted to zero by subtracting the respective median. To determine the reproduced height the SciPy function `leastsq()` optimizes the function given by Equation 15.
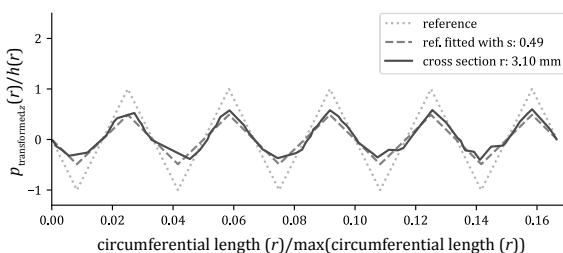

Figure 19: The reference height is fitted to the height of a cross section

Due to the shifting the only optimizable variable s scales the reference in height (Figure 19). The optimized s value corresponds to the relative reproduced height difference for the specific radius. The SSPV repeats the process for each radius and plots the reproduced height difference over the corresponding DHD value. Figure 20 shows an example of an SFR of a partly simulated 3D scan.
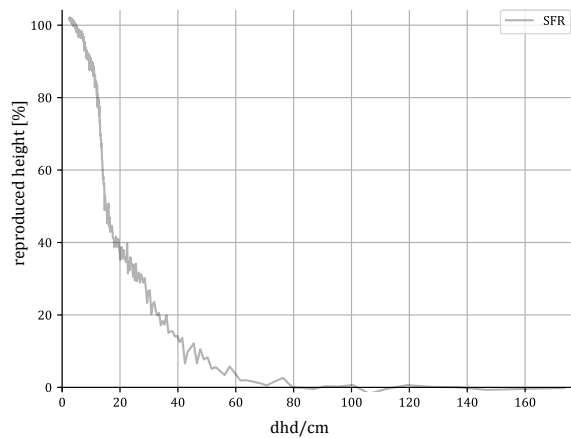

Figure 20: SFR of a partly simulated 3D scan of the Spatial star (DHD values over 160 dhd/cm are cut off due to the lack of changes)

2.9.4 Determining the accuracy unified matrix representation

In addition to the value of the DHD and the SFR, the SSPV determines the accuracy for each point of the UMR. The accuracy describes the degree a 3D scan matches the 3D scanning object (see section 2.1). Thus, it is the result of comparing a sample with its reference. To quantify this comparison SSPV computes the Euclidean distance between each sample point and its corresponding reference point.

Initially, the SSPV computes the UMR for both a sample point cloud and a corresponding reference point cloud. Contrary to the process described in section 2.9.1, the height is not scaled during the transformation (Equation [6] with $s_z = 1$) as scaling would falsify the accuracy test. Due to the discretization process, each reference point has the same radius and circumferential length as its corresponding sample point. Therefore, the Euclidean distance is reduced to the absolute difference in height as shown in Equation [16].

$$dis_{Eucl.} = |h_{sam.} - h_{ref.}| \qquad [16]$$

where $dis_{Eucl.}$ is Euclidean distance, and $h_{sam.}$ is height of the sample.

The SSPV calculates the Euclidean distance for each cell. The result is an accuracy UMR with the same shape as the compared UMRs. A cell value of zero defines a perfect match between the sample and the reference. A higher value means a higher loss in accuracy. The median of all accuracy values reduces the accuracy UMR to a single indicator.

To visualize the accuracy UMR, SSPV uses a color gradient. The gradient is scaled from an accuracy error of

zero to a definable NTE. Since this error depends on the requirements of the use case it cannot be universally determined. The gradient starts with green ($dis_{Eucl.} = 0$) over yellow ($dis_{Eucl.} = 0.5 \times NTE$) to red ($dis_{Eucl.} \geq NTE$) as shown in Figure 21.

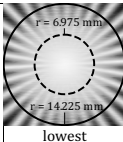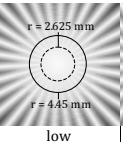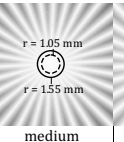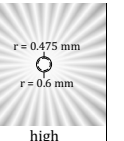non tolerable error (NTE): 0.05 mm, median accuracy: 0.02 mm
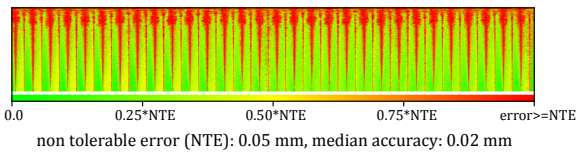
Figure 21: The accuracy UMR of a partly simulated 3D scan with an arbitrarily chosen NTE of 0.05 mm

3. Validation

To validate the presented results the SSPV processes four 3D scans produced with a partly simulated photogrammetry-based system as described in section 2.7. Figure 22 visualizes these 3D scans. The four chosen quality parameters in Metashape – lowest, low, medium and high – correspond per definition in section 2.1 to four 3D scanning systems with an increasing sensor size. As a smaller sensor leads to less pixels per detail the resolution and accuracy and also the point density increases from lowest to high.

Table 1 confirms this prediction. Noticeable is the difference between the two values of the DHD.

Table 1: The results of the validation in terms of resolution and accuracy

Scaled top views of the center of the reproduced Spatial stars				
	lowest	low	medium	high
DHD (see 2.9.2) (solid)	**3.36** dhd/cm	**10.73** dhd/cm	**30.80** dhd/cm	**79.58** dhd/cm
SFR 10% (see 2.4) (dashed)	**6.82** dhd/cm	**18.02** dhd/cm	**44.42** dhd/cm	**95,49** dhd/cm
median accuracy	**0.24** mm	**0.07** mm	**0.02** mm	**0.02** mm

The visualizations in the first row show that the DHD value for the 10 % contrast in the SFR is perceptually more accurate than the DHD value determined as shown in section 2.9.2. The condition to reproduce the correct number of elements seems to be too strict.

Medium and high have the same median accuracy. By comparing the respective accuracy UMR this result is plausible (Figures 23 and 24). Visually the majority of the values for high is around 0.35 × NTE. While medium has a higher amount of non-tolerable errors, it also has a higher amount of values around 0.25 × NTE.

non tolerable error (NTE): 0.05 mm, median accuracy: 0.02 mm
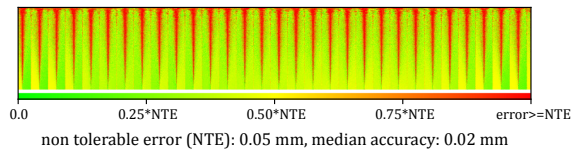
Figure 23: The accuracy UMR for high

non tolerable error (NTE): 0.05 mm, median accuracy: 0.02 mm
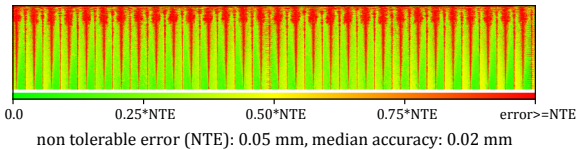
Figure 24: The accuracy UMR for medium

With the decreasing resolution the SFRs of the 3D scan decrease as well (Figure 25). Thus, the high SFR lies completely above the medium SFR, while the medium SFR lies completely above the low SFR which lies completely above the lowest SFR. Noticeable is the characteristic of the SFRs. First the negative slope increases and then turns into a linear negative slope. After the linear decreasing the SFR starts to fluctuate.

Another critical factor is the discretization step as it controls the restructuring of the data. Figure 26 shows the medium SFR for several discretization steps. A larger discretization step results in an increased percentage of the reproduced height. The reason for this is the interpolation. For example, a first point with maximum height lies on radius 0.049 mm. To its left lies a second point with the same height on radius 0.035 mm.
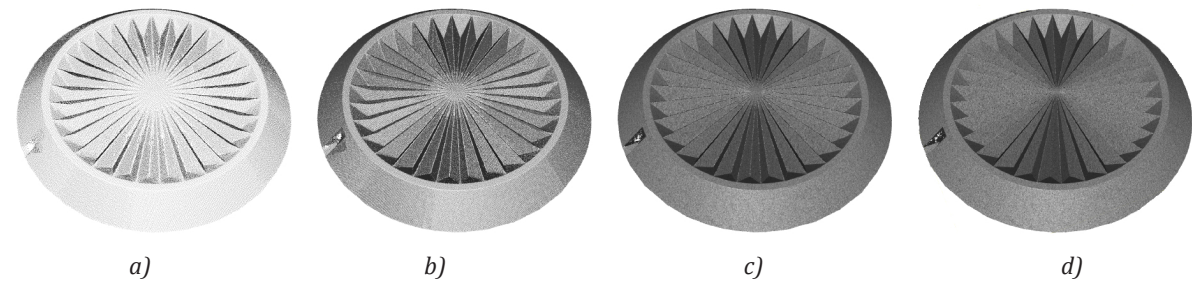
a)   b)   c)   d)

Figure 22: Four partly simulated 3D scans of the Spatial star corresponding to the quality parameters in Metashape: lowest (a), low (b), medium (c) and high (d)

A third point with minimal height lies in between those points on radius 0.029 mm. A discretization step of 0.06 mm shifts all these points to the same radius. The reproduced height is 100 %. A discretization step of 0.03 mm shifts the first and second point to radius 0.06 mm and the third point to radius 0.03 mm. For both radii the reproduced height would be 0 %.
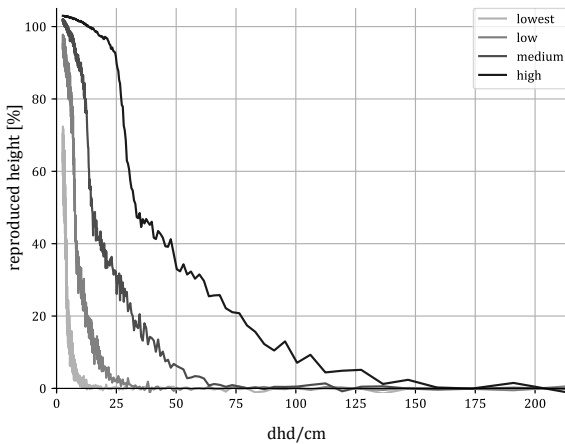

Figure 25: The SFRs of the four partly simulated 3D scans with decreasing resolution and the same discretization step of 0.025 mm
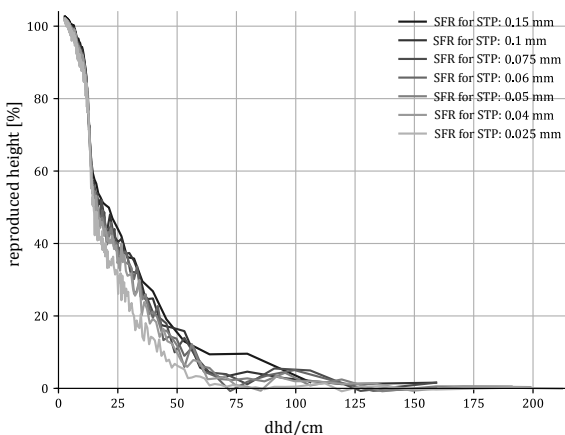

Figure 26: The medium SFR for different discretization steps

4. Discussion and conclusion

This paper has two results. The first result is the Spatial star, a digital testing element to provide the accuracy, resolution and SFR. The second result is the method to restructure a 3D scan of the Spatial star to ensure comparability and to gather and process all required information to determine the accuracy, resolution and SFR. The digital Spatial star therefore allows to determine this information from 3D scans of the Spatial star. The SSPV on the other hand determines the accuracy,

resolution and SFR from an 3D scan of the Spatial star. Therefore, the digital Spatial star in combination with the methods proposed with SSPV built the foundation to implement the workflows shown in the introduction (Figure 1).

The validation shows that the main principle is working. But it also reveals two major issues that need further work. The first one is the influence of the discretization step in combination with the interpolation on the UMR. At the moment only UMRs with the same discretization step are comparable. The optimal discretization step would avoid empty cells in the UMR and therefore minimize the necessity of interpolation. Accordingly, the density of the point cloud defines the optimal discretization step. To get around this issue the processing of triangle meshes will be implemented as the next step.

The second issue is the strict determination of the value of DHD. The DHD value for 10 % reproduced height of the SFR seems to be a good alternative. Further investigations have to proof that this alternative can be transferred to the Spatial star. In respect to the discretization step issue the extracted DHD value needs a visual verification.

With the digital Spatial star this paper introduces a fundamental test element. Further works have to deal with the implementation of the processes required to use the Spatial star in real world scenarios.

One possible implementation could be a workflow to test 3D scanning algorithms or even slicer software for 3D printers. These two testing scenarios can completely be done with the digital Spatial star as no physical object is required. The advantage is the lack of any production uncertainty. In fact, the combination of the partly simulated 3D scans shown in section 2.7 and the validation in section 3 can easily be modified to compare different photogrammetry software.

Another implementation could deal with the testing of 3D printing systems. Here a system under test consists of the slicer software and the 3D printer itself. While the slicer software processes the digital Spatial star into G-code, the 3D printer prints out a physical copy of the Spatial star. The critical part is the re-digitizing of the physical copy as a 3D scanning system depending on its resolution capacity distorts the physical copy by itself.

A good first step would be to use a 3D scanning system with a higher resolution capacity. This raises the question mentioned in the introduction. To what degree the resolution capacity of a 3D scanning system has to be beyond the resolution capacity of the system under test?

Another question is, if the operating principle would work with 3D printers. Figure 27 shows a 3D print-out of the Spatial star described in section 2.7 that looks promising. However real scientific testing has to follow.

Figure 27: A 3D print of the Spatial star
(performed by unfurther specified 3D printer)

The implementation of a workflow to test 3D scanning systems would be the most complex task. The problem here is that the required physical copy of the Spatial star has to have a high degree of detail to be compatible with a wide range of 3D scanning systems. The resolution capacity of the production system has to be at least beyond the resolution capacity of the system under test.

The problem is getting more complex if it comes to creating a digital reference from the physical copy. Here the resolution capacity of the used 3D scanning system has to be beyond the resolution capacity of the production system used. This, from the present point of view, limits the usage of the Spatial star for very detailed 3D scanning systems as the production of the physical copy will be very difficult as well as the creation of the reference. These limits also have to be characterized.

In conclusion, this paper lays the foundation to test several 3D scanning and printing systems. But a lot of work has to be done to implement, characterize and optimize the required processes.

References

Agisoft, 2021a, *Metashape standard edition (1.7.3)*. [computer program] Agisoft Limited Liability Company. Available at: <https://www.agisoft.com/downloads/installer/> [Accessed 1 June 2021].

Agisoft, 2021b, *Agisoft Metashape user manual: standard edition, Version 1.7*. [pdf] Agisoft Limited Liability Company. Available at: <https://www.agisoft.com/pdf/metashape_1_7_en.pdf> [Accessed 11 October 2021].

Blender Online Community, 2021. *Blender – a 3D modelling and rendering package (2.92.0)*. [computer program] Stichting Blender Foundation, Amsterdam. Available at: <http://www.blender.org> [Accessed 1 June 2021].

Birch, G.C. and Griffin, J.C., 2015. Sinusoidal Siemens star spatial frequency response measurement errors due to misidentified target centers. *Optical Engineering,* 54(7): 74104. https://doi.org/10.1117/1.OE.54.7.074104.

Brünger, J., Koch, R., Pears, N., Liu, Y., and Rosin, P.L., 2020. Introduction. In: Y. Liu, N. Pears, P.L. Rosin and P. Huber, eds. *3D imaging, analysis and applications.* 2nd ed. Cham: Springer International Publishing. Ch. 1.4, pp. 12–17. https://doi.org/10.1007/978-3-030-44070-1.

Canon Deutschland GmbH, 2021. *Canon EOS 750D: Technische Daten*. [online] Available at: <https://www.canon.de/for_home/product_finder/cameras/digital_slr/eos_750d/specifications.html> [Accessed 11 October 2021].

CloudCompare, 2021. *CloudCompare (2.11 Alpha)*. [computer program] Available at: <http://www.cloudcompare.org/> [Accessed 11 October 2021].

Drouin, M.-A. and Beraldin, J.-A., 2020. Active triangulation 3D imaging systems for industrial inspection. In: Y. Liu, N. Pears, P.L. Rosin and P. Huber, eds. *3D imaging, analysis and applications.* 2nd ed. Cham: Springer International Publishing. Ch. 3, pp. 109–165. https://doi.org/10.1007/978-3-030-44070-1.

Goesele, M., Fuchs, C., and Seidel, H., 2003. Accuracy of 3D range scanners by measurement of the slanted edge modulation transfer function. In: *Fourth International Conference on 3-D Digital Imaging and Modeling: Proceedings*. Banff, AB, Canada, 6–10 October 2003. IEEE, pp. 37–44. https://www.doi.org/10.1109/IM.2003.1240230.

Guidi, G. and Frischer, B.D., 2020. 3D digitization of cultural heritage. In: Y. Liu, N. Pears, P.L. Rosin and P. Huber, eds. *3D imaging, analysis and applications.* 2nd ed. Cham: Springer International Publishing. Ch.13.2.1, pp. 631–697. https://doi.org/10.1007/978-3-030-44070-1.

Harris, C.R., Millman, K.J., van der Walt, S.J., Gommers, R., Virtanen, P., Cournapeau, D., Wieser, E., Taylor, J., Berg, S., Smith, N.J., Kern, R., Picus, M., Hoyer, S., van Kerkwijk, M.H., Brett, M., Haldane, A., Del Río, J.F., Wiebe, M., Peterson, P., Gérard-Marchant, P., Sheppard, K., Reddy, T., Weckesser, W., Abbasi, H., Gohlke, C. and Oliphant, T.E., 2020. Array programming with NumPy. *Nature*, 585, pp. 357–362. https://www.doi.org/10.1038/s41586-020-2649-2.

Harvey, P., 2021. *ExifTool (l2.32)*. [computer program] Available at: <https://exiftool.org/> [Accessed 01 June 2021].

Hunter, J.D., 2007. Matplotlib: a 2D graphics environment. *Computing in Science & Engineering*, 9(3), pp. 90–95. https://www.doi.org/10.1109/MCSE.2007.55.

International Organization for Standardization, 2017. *ISO 12233:2017(en) Photography – Electronic still picture imaging – Resolution and spatial frequency responses*. Geneva: ISO.

Kai, C.C., Jacob, G.G.K. and Mei, T., 1997. Interface between CAD and rapid prototyping systems. Part 1: a study of existing interfaces. *The International Journal of Advanced Manufacturing Technology*, 13(8), pp. 566–570. https://doi.org/10.1007/BF01176300.

Kintel, M., 2021. *OpenSCAD (2021.01)*. [computer program] Available at: <https://openscad.org/> [Accessed 01 June 2021].

Loebich, C., Wueller, D., Klingen, B. and Jaeger, A., 2007. Digital camera resolution measurement using sinusoidal Siemens star*s*. In: *Proceedings SPIE 6502, Electronic Imaging 2007, Digital Photography III.* San Jose, CA. USA, 20 February 2007. SPIE. https://doi.org/10.1117/12.703817.

Masaoka, K., 2018. Accuracy and precision of edge-based modulation transfer function measurement for sampled imaging systems. *IEEE Access,* 6, pp. 41079–41086. https://doi.org/10.1109/ACCESS.2018.2856742.

McKinney, W., 2010. Data structures for statistical computing in Python. In: S. van der Walt and J. Millman, eds. *Proceedings of the 9th Python in Science Conference*. Austin, TX, USA, 28 June – 3 July 2010. SciPy, pp. 56–61. https://www.doi.org/10.25080/Majora-92bf1922-00a.

Se, S. and Pears, N., 2020. Passive 3D imaging. In: Y. Liu, N. Pears, P.L. Rosin and P. Huber, eds. *3D imaging, analysis and applications.* 2nd ed. Cham: Springer International Publishing. Ch. 2.2.1, pp. 39–107. https://doi.org/10.1007/978-3-030-44070-1.

Virtanen, P., Gommers, R., Oliphant, T.E., Haberland, M., Reddy, T., Cournapeau, D., Burovski, E., Peterson, P., Weckesser, W., Bright, J., van der Walt, S.J., Brett, M., Wilson, J., Millman, K.J., Mayorov, N., Nelson, A.R.J., Jones, E., Kern, R., Larson, E., Carey, C.J., Polat, İ., Feng, Y., Moore, E.W., VanderPlas, J., Laxalde, D., Perktold, J., Cimrman, R., Henriksen, I., Quintero, E.A., Harris, C.R., Archibald, A.M., Ribeiro, A.H., Pedregosa, F., van Mulbregt, P. and SciPy 1.0 Contributors, 2020. SciPy 1.0: fundamental algorithms for scientific computing in Python. *Nature methods,* 17(3), pp. 261–272. https://www.doi.org/10.1038/s41592-019-0686-2.

Zhou, Q-Y., Park, J. and Koltun, V., 2018. Open3D: a modern library for 3D data processing. *arXiv* [online] Available at: <http://arxiv.org/pdf/1801.09847v1> [Accessed 01 June 2021].

Glucomannan–xylan blend biofilms for food packaging: preparation and evaluation of filmogenic solutions and biofilms

Kholoud Al-Ajlouni, Paul D. Fleming and Alexandra Pekarovicova

Chemical and Paper Engineering,
Western Michigan University, USA

kholoudsaleh.alajlouni@wmich.edu
dan.fleming@wmich.edu
a.pekarovicova@wmich.edu

Abstract

Food packaging nowadays requires a sustainable, biodegradable, and friendly to the environment wrapping films. After cellulose, the hemicellulose in plants and grasses is the potential source for the biofilms. Konjac glucomannan is one of the hemicelluloses used to synthesize wrapping films. In this research, we conducted three sets of experiments: we formulated pure glucomannan biofilms, glucomannan–xylan blend biofilms with nano-fibrillated cellulose (NFC), and finally glucomannan–xylan blends without NFC. We studied the rheology of the filmogenic solution of the blends, before casting, and the physical and mechanical properties of the biofilms. The biofilms consisted from: glucomannan, xylan, NFC as reinforcement polymer, Surfynol 104 PA as surfactant and Sorbitol as a plasticizer. Pure glucomannan was stiff and viscous and in some cases showed a faceting phenomenon. In general, blended biofilms exhibited better properties with the presence of NFC in the formulation.

Keywords: faceting, nano-fibrillated cellulose, stretch wrapping, shear thinning, frequency sweep

1. Introduction and background

The global market for food packaging is a fast-growing one. In 2019, it was estimated as USD 303 billion and is predicted to be 503 billion in 10 years (Grand View Research, 2020). The increase of the consumer's awareness of environmentally friendly packaging and the demand for cheap, lightweight, stretchable, moisture and aroma barrier protection and printable materials, was the fuel for the continuous search for green alternatives. Wrapping films from petroleum-based plastics have the good qualities for food packaging, however, they do not exhibit biodegradability or recyclability (Honarvar, Hadian and Mashayekh, 2016). Low density polyethylene (LDPE), for example, is flexible, tough and transparent, which makes it dominating in bags or stretch film applications, but it needs 10–20 years to decompose naturally in landfill (Kunlere, Fagade and Nwadike, 2019). Bioplastics are the alternatives to plastics and they are extracted from plants, algae, shells of crustaceans and agricultural wastes. In plants, hemicellulose represents 20–30 % of the dry weight of the biomass and has 500–3 000 sugar units per polymer and

dissimilar linkages (Hu, Du and Zhang, 2018). Biofilms synthesized from hemicellulose polymers are renewable, sustainable, biodegradable, and non-toxic, yet, they have proven to show semi crystallinity and hygroscopic behavior. They also allow moisture and gases to pass through them causing the food to rot. They do not stretch and elongate as plastic films, which means that their mechanical properties are poor (Hartman, 2006; Zhong, et al., 2013). One of the ways to improve the tensile strength of biofilms is blending with other polymers. Hemicelluloses have abundant number of hydroxyl groups distributed along their long backbone and frequent side chains, allowing hydrogen bond formation with other polymers; this bond is comparatively weak, but the composite film can be strong (Chen, et al., 2016). Glucomannan is a water-soluble hemicellulose found in hardwood, representing 1–4 % of the dry matter; in softwood its amount is about 20–25 % (Deshavath, Veeranki and Goud, 2019) and similarly in other plants. The content depends on the type and part of the plant from which it is extracted (Shi, et al., 2020). It is a hetero polysaccharide made up of glucose and mannose units (1:1.6) and its backbone consists of linked β-1,4 glyco-

sidic bonds between the sugar units (Wang, et al., 2017; Scheller and Ulvskov, 2010). Glucomannan from the tuber of konjac plant is an edible hemicellulose, viscous, dissolves easily in water and has high molecular weight. To overcome poor mechanical and barrier properties of pure glucomannan films, xylan and nano-fibrillated cellulose (NFC) have been blended with it. Xylan from corncobs makes up to 40 % of the dry matter, is a branched hetero polysaccharide whose backbone is composed of β-1,4-D-xylopyranose units with different side chains (Sasmitaloka, et al., 2019). The chemical structures of glucomannan and xylan are shown in Figure 1.
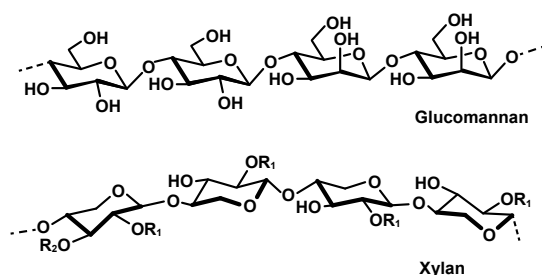

Figure 1: Chemical structure of glucomannan and xylan hemicelluloses (adapted from Nechita and Roman, 2020)

Konjac glucomannan films for food packaging improved its oxygen barrier property by using sorbitol as an external plasticizer; enhanced tensile strength by blending with NFC (Ma, Pekarovicova and Fleming, 2018), starch (Yoshimura, Takaya and Nishinari, 1998), cellulose (Kalia, et al., 2011), chitosan (Wu, et al., 2019) and others. Xylan-based packaging films suffer from poor mechanical strength, brittleness, due to strong hydrogen bonding, and moisture sensitivity. Its performance is also reinforced by cellulose, micro and nano-fibrils, plasticizer and biopolymers (Zhong, et al., 2013).

Rheology is important for flow of the filmogenic or film-forming solutions of the polymers during production, the uniformity and thickness of the produced films and spreading of the ink over the films during printing (Chakravartula, et al., 2019). A rheological study of the polymers was made since all biopolymers exhibit viscoelastic behavior, that is, their viscosity decreases when the applied shear rate is increased (Lopez and Richtering, 2021; Picout and Ross-Murphy, 2003). The gel point of the film-forming solutions was determined by storage and loss moduli, G' and G'', respectively. For a polymer, if $G' < G''$ then the filmogenic solution is viscous and behaves like a liquid, else it is elastic and acts as a soft solid or gel (Morrison, 2001). The viscosity of the filmogenic solution of the biopolymers is reduced by increasing the applied shear rate, because the bonds were broken and the particles present in the aqueous suspension are ruined by shear (Triantafillopoulos, 1988). In a previous work, we used konjac glucomannan to make packaging films, but we confronted a phase

transformation of the polymer droplets and freezing of the surfactant at the glucomannan–water interface. This phenomenon is called faceting, and triggered the deformation of glucomannan spherical droplets into distorted polygons and long thin fibers. Uncontrolled slow cooling with the presence of the surfactant was the reason behind faceting. The 3D structure of the frozen surfactant made the produced films non-transparent, weak and gas permeable (Al Ajlouni, Fleming and Pekarovicova, 2021). In this work, the glucomannan–xylan biofilms studied were divided into three sets: pure glucomannan, glucomannan–xylan blends reinforced with NFC, and glucomannan–xylan blends without NFC. The aim is to see the effect of xylan and NFC on the properties of blend films all together.

2. Experimental

In the first sets of the studies (Al Ajlouni, Fleming and Pekarovicova, 2021), a shape deformation of pure glucomannan droplets emulsion in the surfactant solution showed up, and resulted in hard, rough and polygon surface, which was revealed after drying and did not show upon casting. The surfactant lowered the surface tension of the glucomannan drops at the interface with water and made them lose their spherical shape into polygons; this phenomenon is known as faceting. The authors studied the effect of the surfactant of faceting of the biofilms. The concentrations were 0.05–0.4 g of the surfactant in 100 ml of DI water. The films gained thickness but lost some of their optical, physical and mechanical properties.

2.1 Materials

Xylan from corncob, Biosynth Carbosynth company, molecular weight: 300–900 Da; glucomannan from konjac, NOW Food Company, molecular weight: $(0.2–2) × 10^6$ Da (Now Foods, n.d.); Surfynol 104 PA, Air Products and Chemical Inc.; Sorbitol, Alfa Aesar, molecular weight: 182.17 Da, and deionized (DI) water from WMU. The components of each film are given in Table 1. The name of the films represents the amount of glucomannan mass in the film formulation, for example, Gluc90 means 0.9 g glucomannan with 0.1 g xylan dissolved in 100 ml of DI water. The other ingredients are kept constant: Surfynol 104 PA, NFC and Sorbitol.

2.2 Glucomannan–xylan biofilms synthesis

Glucomannan was dissolved in 100 ml of DI water at room temperature and then transferred into a water bath at 40 °C, where the solution was mixed for 15 minutes by a rotary mixer. The surfactant, Surfynol 104 PA, was added to the solution and mixed for 3 minutes followed by xylan, which was mixed for 5 minutes.

Table 1: Glucomannan and glucomannan–xylan films showing NFC contributions (in 100 ml DI water)

	Film's name	Glucomannan [g]	Surfynol 104 PA [g]	Xylan [g]	NFC [g]	Sorbitol [g]
Pure	Gluc100	1.0	0.1	0	0.1	0.2
Without NFC	Gluc90	0.9	0.1	0.1	0	0.2
	Gluc80	0.8	0.1	0.2	0	0.2
	Gluc70	0.7	0.1	0.3	0	0.2
	Gluc60	0.6	0.1	0.4	0	0.2
	Gluc50	0.5	0.1	0.5	0	0.2
	Gluc40	0.4	0.1	0.6	0	0.2
With NFC	Gluc90	0.9	0.1	0.1	0.1	0.2
	Gluc80	0.8	0.1	0.2	0.1	0.2
	Gluc70	0.7	0.1	0.3	0.1	0.2
	Gluc60	0.6	0.1	0.4	0.1	0.2
	Gluc50	0.5	0.1	0.5	0.1	0.2
	Gluc40	0.4	0.1	0.6	0.1	0.2

NFC was mixed for 5 minutes more and finally Sorbitol for 3 extra minutes. In pure glucomannan experiments, xylan was not added. For density, viscosity, rheology, contact angle and surface energy tests, a 5–10 ml sample of the film-forming solution was collected and tested. The rest of the film-forming solution was casted in a Petri dish and dried at 60 °C and 35 % RH. After drying, the film was peeled off and stored in the testing lab for conditioning before testing based on TAPPI's conditions: 50 % RH, 23 °C for 24 hours. For film characterization, some tests were accomplished and compared with the control sample, LDPE film.

2.3 Filmogenic solutions' tests

2.3.1 Density

Density is measured by a Gardco pycnometer, which has an exact volume of 8.32 ml at 20 °C. The mass of the filmogenic solution is calculated by the difference of the masses of the cup, with and without the solution, and the density is calculated in g/cm^3.

2.3.2 Viscosity and rheology

An Anton Paar rheometer was used and a rheogram of the apparent viscosity vs. shear rate was produced; the shear rate range was 0.1–1 000 s^{-1}. The value of the storage and loss shear moduli under frequency sweep test were determined and plotted, and the point where the film-forming solution turns into gel was detected.

2.3.3 Surface tension of filmogenic liquids before drying

A FTA200 instrument was used for contact angle and surface tension measurements by recording a video of drops of a fluid falling over a substrate by a controlled needle pump and a camera capturing 300 images per run.

2.4 Non-destructive tests of the biofilms

Non-destructive tests are the tests that keep the sample as it is before testing; these were done first. Examples of non-destructive tests are: measurement of thickness, roughness, air permeability, opacity, transparency and other properties.

2.4.1 Thickness of the glucomannan–xylan biofilms

After conditioning the biofilms, the thickness or caliper was measured by Technidyne Profile Plus machine. Its accuracy is ± 0.508 mm. The thickness of the films depends on the type of mold used in casting the filmogenic solution, and the drying conditions. Once the solution was poured into a Petri dish, it was levelled and started cooling. Air flow inside the Caron environmental chamber was not circulated evenly on the surface, which caused little variations in the thickness of the biofilms between the center and at the rim. Thickness influences roughness, transparency, permeability, tensile strength and % elongation of the films.

2.4.2 Transmittance and transparency

Transmittance is the ratio between visible light transmitted through the film to that falling on the surface, expressed as a fraction T and governed by Beer's law (Ingle and Crouch, 1988). Transparency is usually characterized by light transmittance, type of polymer crystallinity and types of additives used. Crystalline or semi-crystalline polymers, LDPE for instance, are opaque because there are amorphous and crystalline regions, which make transmission different.

A Spectroscan auto scanner measures the transmission of visible light, in the range of 280–600 nm, passing through the biofilm according to ISO 13468–1 (International Organization for Standardization, 2019).

Transparency is defined as:

transparency = −log (transmittance/thickness)   [1]

Equation [1] depends on the unit of length used to measure the thickness. If the thickness is measured in mm, the transparency is given in terms of the transmittance of 1 mm thick sample. This is based on how transparency scales with thickness according to the Beer–Lambert law (Ingle and Crouch, 1988). If the amount of light transmitted through the biofilm is high, the higher the transparency will be.

2.4.3 Air permeability

Parker Print Surf instrument measures the "PPS porosity" of the biofilms in ml/min, and air permeability coefficient K is calculated according to TAPPI T 555 (Technical Association of the Pulp and Paper Industry, 2010). Air permeability (PPS porosity) means the ability of the films to let air pass through as a result of air pressure difference on both sides for 5 seconds and it has the units of (mm^2 for permeability, or ml/min for PPS porosity) (IGT team, 2021). Darcy's equation describes the fluid flow through any porous material, where the flow rate of the fluid is a function of the pressure drop across the sample, area of flow and viscosity of the fluid and defines the permeability coefficient K (m^2). Pal, Joyce and Fleming (2006) proposed a method to calculate the permeability coefficient based on PPS porosity values in ml/min at 1 000 kPa air pressure with viscosity of air at 23 °C of 1.8×10^{-5} Pa·s, area of 10 cm^2 and air pressure drop of 6.17 kPa between the two sides. The relation becomes:

$K = 0.048838 \times Q \times L$ [2]

where K is given in μm^2, Q is air flow rate in ml/min and L is the thickness of the film in m, the number 0.048838 contains the constant values, such as viscosity of air and the area of the sample (Pal, Joyce and Fleming, 2006). This property is essential for packaging biofilms to protect food from getting spoiled or altered by chemical reactions with air or moisture.

2.5 Destructive tests of the biofilms

The destructive tests are the tests that deform or damage the specimen upon testing and it is done to identify physical and chemical properties of the material. One example is tensile test.

2.5.1 Tensile strength and % elongation

The ability of the packaging films to stretch and ensure a good seal is expressed in terms of tensile strength and % elongation of the films. High tensile strength keeps the products secured and sealed during shipping.

An Instron instrument was used to test the tensile and elongation of the films. The samples were cut as a strip of 100 mm × 15 mm, gripped in Instron clamps and pulled apart under a 500 N load and with a speed of 2.5 cm/min until it breaks. The software accompanied with the machine reports the values and plots the results of tensile strength at break and % elongation at break or strain among other properties.

3. Results and discussion

3.1 Faceting of glucomannan polymer

In Figure 2, the surface of the deformed biofilms after drying (at 50 °C and 11.4 % RH) shows clear polygon shapes and solid boundaries. The best concentration of Surfynol 104A used in the experiments is 0.1 g in 100 ml DI water. Upon testing, the films gained thickness but lost some of their optical, physical and mechanical properties.

3.2 Results of filmogenic solutions' tests

Characterization of the filmogenic solutions started with the density. The density of the all the samples was measured by Gardco pycnometer at 20 °C and rounded to three significant figures, so the density was 1 g/cm^3 or 1 000 kg/m^3 for all samples. All results, including the values for xylan, are listed in Table 2.

a)   b)   c)   d)   e)
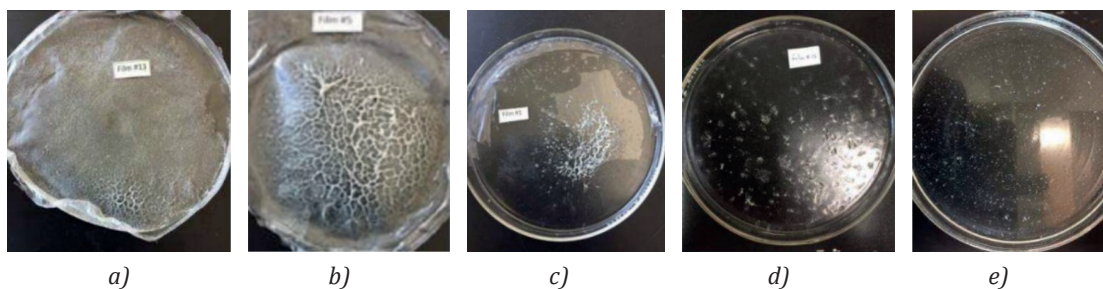
Figure 2: Faceted glucomannan biofilms (a) to (d) and a successful one (e)
(adapted from Al Ajlouni, Fleming and Pekarovicova, 2021)

Table 2: Some properties of the filmogenic of glucomannan, glucomannan–xylan and xylan solutions

	Filmogenic film	Density [g/cm³]	Apparent viscosity at 100 s⁻¹ [mPa·s]	Contact angle [Angle]	Surface tension [mN/m]
Pure	Gluc100	1.0	1 333	57	38
Without NFC	Gluc90	1.0	1 169	54	45
	Gluc80	1.0	767	55	46
	Gluc70	1.0	611	62	43
	Gluc60	1.0	384	56	41
	Gluc50	1.0	263	57	41
	Gluc40	1.0	179	52	42
With NFC	Gluc90	1.0	1 117	68	45
	Gluc80	1.0	773	62	46
	Gluc70	1.0	576	56	45
	Gluc60	1.0	410	51	44
	Gluc50	1.0	238	44	42
	Gluc40	1.0	72	42	42
	Xylan	0.9	68	23	43

3.2.1 Viscosity

The apparent viscosity in Table 2 shows that the pure glucomannan film is the most viscous one having 1333 mPa·s at 100 s⁻¹. The viscosities of the film-forming solutions without the presence of NFC were higher than the solutions had when NFC was added, with exception for Gluc80 and Gluc60. For example, Gluc90 filmogenic solution viscosity without NFC was lowered from 1167 to 1117 mPa·s. Similarly, increasing the concentration of the glucomannan made the film-forming solutions more viscous, due to the highly viscous nature of glucomannan and higher molecular weight as illustrated in Figure 3.

3.2.2 Rheology

The Anton Paar Rheometer with a parallel plate measuring system used a frequency sweep test to measure the loss G'' and storage G' moduli, in the range of 0.01 to 100 rad s⁻¹ at 25 °C and under shear strain of 5 %.

Figure 4 demonstrates the viscoelastic behavior of pure glucomannan filmogenic solution.

Reinforced pure glucomannan turned into a gel at 63 rad/s, whereas the non-reinforced became a gel earlier at 3.6 rad/s. This implies that the internal friction between the molecules and particles is higher due to NFC addition to the polymer matrix. The same arguments can be said about glucomannan–xylan filmogenic solutions illustrated in Figure A1 in Appendix. A comparison of the rheological behavior of each filmogenic solution is presented between that reinforced with NFC (Figure A1a) and that without NFC. A summary of the loss and storage moduli is listed in Table 3, evaluated at 100 rad/s.

The glucomannan–xylan filmogenic solutions with NFC were gelling slower than the same solutions without NFC, i.e. $G' > G''$, which means that NFC hindered the gelation process. Also, the storage modulus was greater than the loss modulus $G' > G''$ for higher gluco-
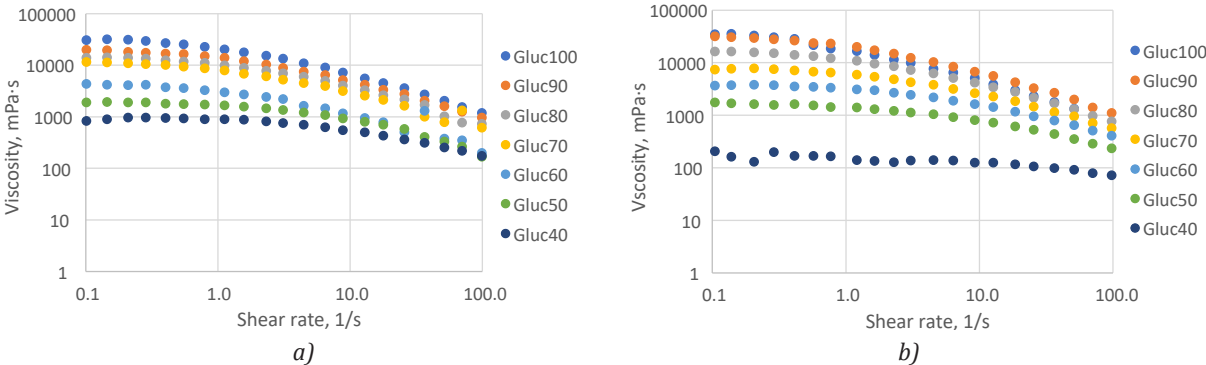

Figure 3: Viscosity of filmogenic solutions of glucomannan and glucomannan–xylan, without NFC (a) and reinforced with NFC (b)
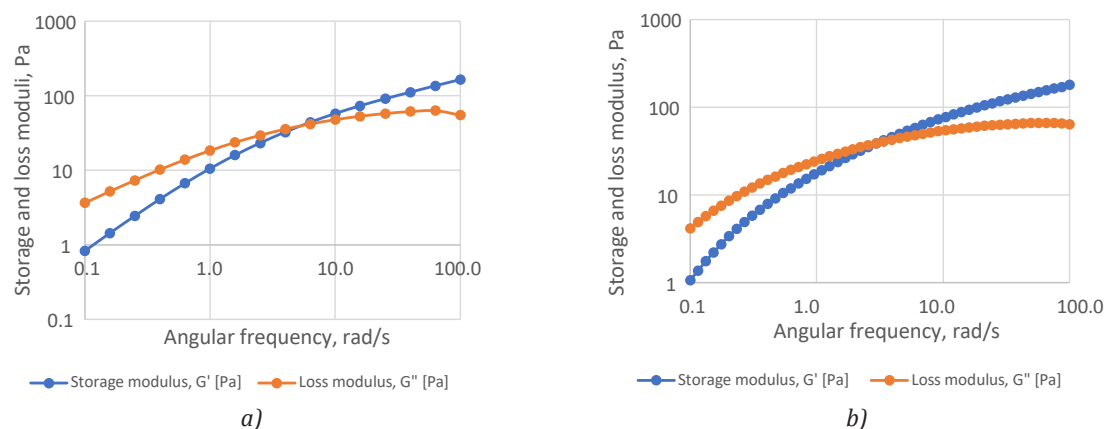
a)   *b)*

Figure 4: Frequency sweep for pure glucomannan filmogenic solutions reinforced with NFC (a) and without NFC (b)

mannan concentrations (Gluc100–Gluc70) and Gluc40, but Gluc60 and Gluc50 without NFC had $G' < G''$, which indicated that both started gelation earlier than the other samples.

Table 3: Storage and loss moduli of glucomannan and glucomannan-xylan filmogenic solutions at 100 rad/s

	Filmogenic film	Storage modulus, G' [Pa]	Loss modulus, G'' [Pa]
Pure	Gluc100	179	64
Without NFC	Gluc90	174	76
	Gluc80	139	21
	Gluc70	30	18
	Gluc60	21	25
	Gluc50	5	12
	Gluc40	15	8
With NFC	Gluc100	165	55
	Gluc90	112	70
	Gluc80	129	21
	Gluc70	62	36
	Gluc60	20	22
	Gluc50	8	3
	Gluc40	5	2

3.2.3 Surface tensions and contact angles

Figure 5 shows a demonstration of the contact angle and a pendant drop of glucomannan over glass measured by FTA200. The blends of glucomannan–xylan were tested for the effect of the NFC on the formulation of the biofilms. The NFC revealed a direct increase in the value of the contact angles of the filmogenic solutions.

Pure glucomannan filmogenic solution possessed a 57° contact angle (rounded on two digits), which implies that wettability of the solution onto the surface of glass is low. The contact angle of all solutions exceeded 40°, however, the average of the solutions' contact angles without NFC was higher than that with NFC, 56° and 54°, respectively. The values of the contact angles of the blends of glucomannan–xylan were less than pure glucomannan, which may give an indication that xylan reduced the contact angle and increased the wettability of the blends. Xylan has a small contact angle of 23° and a surface tension 43 mN/m, therefore, when the amount of xylan is increased, it contributes in reducing the contact angles of the overall solutions, as shown in Figure 6.
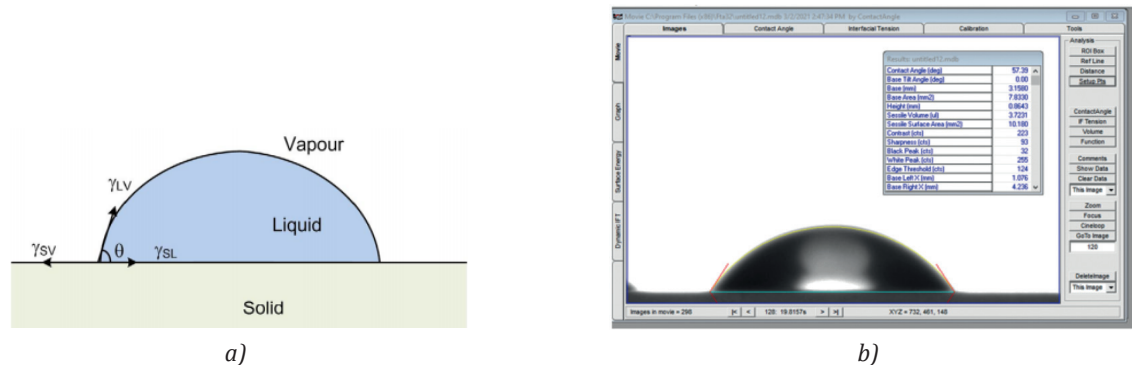

a)   *b)*

Figure 5: Contact angle and surface tension of a drop over a substrate when surface tensions between each two phases are in equilibrium (Makkonen, 2016) (a); and a drop of pure glucomannan filmogenic solution over glass, with contact angle 57.29° for 0.1 g surfactant in pure glucomannan (Al Ajlouni, Fleming and Pekarovicova, 2021) (b)
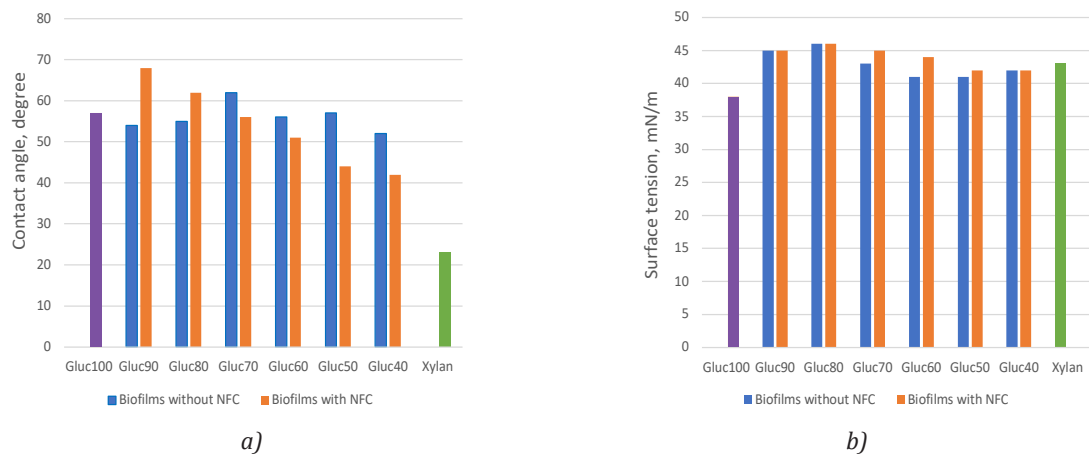
a)   *b)*

*Figure 6: The contact angles (a), and surface tensions (b) of filmogenic solutions
of glucomannan, glucomannan–xylan biofilms, and xylan*

3.3 Results of non-destructive testing of glucomannan–xylan biofilms

The non-destructive tests are illustrated in Table 4 and the graphs are shown in Figure 7 for all samples compared with LDPE film.

3.3.1 Thickness of glucomannan–xylan biofilms

The thickness of the biofilms was measured and the average of 5 readings was recorded as illustrated in Table 4 and shown in Figure 7. The changes in the thickness due to air flow on the surfaces appeared during the drying process; the areas close to the edges of the Petri dish were thinner than the middle, so leveling and thickness were not the same. The addition of NFC increased the caliper of the biofilms, maybe because

it made extra bonding between the components of the biofilms and made it tighter and thicker. Only Gluc80 deviated from the trend, there was 7.6 μm difference between the two cases of NFC presence or not.

3.3.2 Transmittance and transparency

As given in Table 4, LDPE has a highest transmittance of 96 %, which is obvious since it is semi-crystalline. All the films showed an average > 71 % transmittance; the films Gluc100 to Gluc50 have almost close % transmittance, average of 77 %, but Gluc40 deviated by almost 12 %. This may indicate that the structure of the glucomannan–xylan biofilms is semi-crystalline. We may also conclude that the glucomannan concentration enhanced the % transmittance of visible light through the polymer blend matrices.

Table 4: Results of non-destructive tests of glucomannan and glucomannan–xylan films

|	Filmogenic film	Thickness [μm]	Transmittance [%]	Transparency (Eq. [1])	PPS roughness [μm]	PPS porosity [ml/min]	Air permeability coefficient (Eq. [2]) [μm²]
Pure	Gluc100	62.01	79.0	1.89	4.34	1.34	4.1×10^{-6}
Without NFC	Gluc90	76.44	80.8	1.98	5.94	1.57	5.9×10^{-6}
	Gluc80	87.60	80.1	2.04	2.13	0.71	3.0×10^{-6}
	Gluc70	96.52	78.7	2.09	0.32	0.33	1.6×10^{-6}
	Gluc60	116.58	73.3	2.20	1.64	0.11	6.3×10^{-7}
	Gluc50	140.13	70.3	2.30	0.83	0.14	9.6×10^{-7}
	Gluc40	108.15	55.2	2.29	0.61	0.36	1.9×10^{-6}
With NFC	Gluc100	71.75	87.6	1.91	6.63	0.84	2.9×10^{-6}
	Gluc90	83.78	75.4	2.05	7.33	0.59	2.4×10^{-6}
	Gluc80	80.00	68.6	2.07	5.43	0.34	1.3×10^{-6}
	Gluc70	105.91	71.3	2.17	1.36	0.18	9.3×10^{-7}
	Gluc60	150.28	66.8	2.35	2.67	0.08	5.9×10^{-7}
	Gluc50	155.18	65.5	2.37	5.94	0.90	6.8×10^{-6}
	Gluc40	134.33	53.0	2.40	1.95	0.45	3.0×10^{-6}
	LDPE	118.00	96.0	2.09	0.11	0.10	8.8×10^{-8}
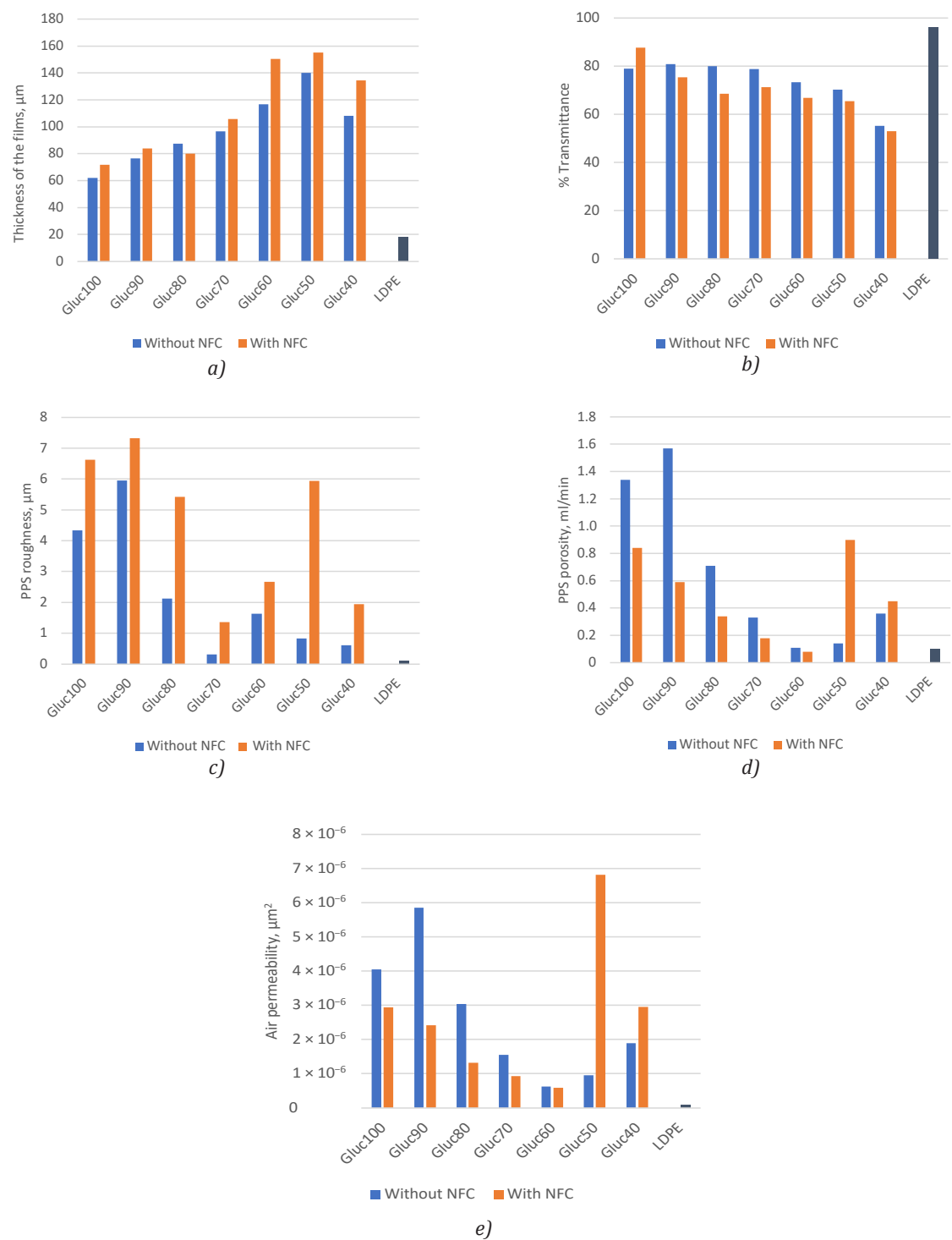
Figure 7: Non-destructive tests of glucomannan, glucomannan–xylan biofilms, reinforced with NFC and without NFC, compared with LDPE films: thickness (a), transmittance (b), PPS roughness (c), PPS porosity (d), and air permeability (e)
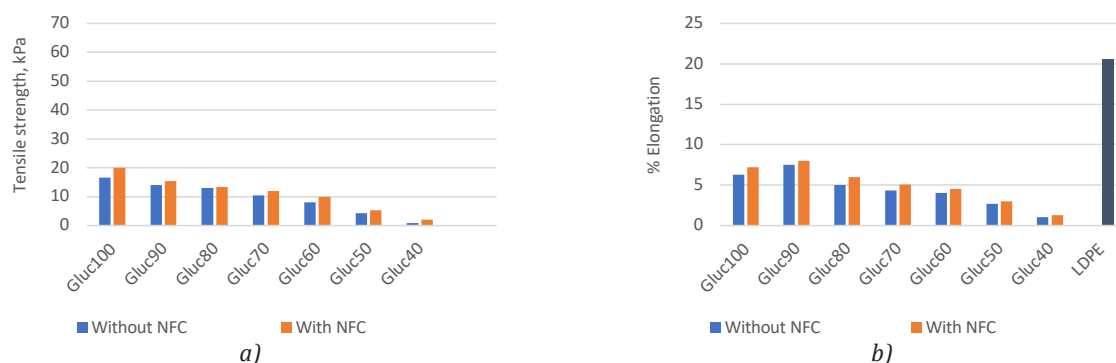
Figure 8: Tensile strength (a), and % elongation (b) of glucomannan and glucomannan–xylan biofilms, reinforced with NFC and without NFC, in addition compared with LDPE films (b)

3.3.3 PPS roughness

The PPS roughness was measured (soft backing and a clamping pressure of 1 000 Pa). The results (Figure 7) confirmed that the presence of NFC generated more rough surfaces for all biofilms; Gluc90 without NFC displayed the highest roughness of all, 5.94 μm, and the smoothest biofilm was Gluc70 with NFC, 1.36 μm, though it still has higher roughness than LDPE, 0.1 μm.

3.3.4 PPS porosity

The porosity of reinforced Gluc60 has the least value, 0.08 ml/min followed by LDPE film, 0.1 ml/min. The presence of NFC affected the PPS porosity in a good way by making non-porous biofilms, but not in the case of reinforced Gluc50 and Gluc40, maybe because the amount of xylan was increased. Gluc90 without NFC is the most porous biofilm. Figure 7 shows how the NFC helped in blocking the passages for air to flow through the biofilms.

3.3.5 Air permeability

The calculations of air permeability coefficient according to Equation 2 are listed in Table 4 and plotted in Figure 7. The less permeable biofilms were Gluc60, Gluc70, Gluc80 and Gluc40. Gluc50 reinforced with NFC had the maximum air permeability coefficient, 1.3×10^{-6} mm² compared to Gluc50 without NFC, while Gluc90 showed the opposite. For LDPE film, the air permeability coefficient was the least value 8.8×10^{-8} mm², making it a good barrier of air and other gases, so does Gluc60 and Gluc70.

3.4 Destructive tests

Tensile test and % elongation test for each sample is presented in Figure 8, the latter compared with plastic film LDPE. The plastic film LDPE has the tensile strength of 600 kPa. The reason of this value is the crystallinity of LDPE and long branches that give it strong structure (Bastarrachea, Dhawan and Sablani, 2011). The biofilm of pure glucomannan showed the highest tensile value of all biofilms. From the Figure 8a, we notice that there is a drop of the tensile values as the concentration of the glucomannan is lowered; Gluc100 with NFC had 20 kPa whereas Gluc40 with NFC had 2 kPa. In the other set, non-NFC biofilms, Gluc100 had 16.7 kPa and Gluc40 0.9 kPa. All biofilms with NFC showed a higher value than non-NFC biofilms. It may be explained as glucomannan has the larger polymer chain among other polymers of the biofilm matrix (xylan, NFC and sorbitol) and the bonds between the chains made it stronger.

Similarly, in Figure 8b, the % elongation of the test samples are plotted. The plastic film LDPE elongated 20.6 %, which is more than other samples, and the least was Gluc40 without NFC by only 8 %. The same reasons as in the case of tensile strength can explain the high value of % elongation of LDPE, its crystallinity and branching.

4. Conclusions

Glucomannan or xylan stand-alone biofilms suffered from mechanical and moisture barrier problems. Therefore, in order to solve these problems, composite biofilms with each other and NFC were prepared. In general, we found that adding xylan to glucomannan improved the wettability, reduced the viscosity and lowered the gelation point of the filmogenic solutions compared to pure glucomannan; from film forming aspects, xylan reduced the PPS porosity, air permeability as well as transmittance, tensile strength and elongation. NFC addition to the glucomannan–xylan matrix hindered the gelation point of the filmogenic solutions and improved tensile and elongation at break of the biofilms.

References

Al Ajlouni, K., Fleming P.D. and Pekarovicova, A., 2021. Glucomannan for food packaging biofilms: faceting of the polymer film. In: C. Ridgway, ed. *Advances in Printing and Media Technology: Proceedings of the 47th International Research Conference of iarigai.* Athens, Greece, 19–23 September 2021. Darmstadt: iarigai, pp. 97–109. http://doi.org/10.14622/Advances_47_2021.

Bastarrachea, L., Dhawan, S. and Sablani, S.S., 2011. Engineering properties of polymeric-based antimicrobial films for food packaging. *Food Engineering Reviews*, 3(2), pp. 79–93. https://doi.org/10.1007/s12393-011-9034-8.

Chakravartula, S.S.N., Soccio, M., Lotti, N., Balestra, F., Dalla Rosa, M. and Siracusa, V., 2019. Characterization of composite edible films based on pectin/alginate/whey protein concentrate. *Materials*, 12(15): 2454. https://doi.org/10.3390/ma12152454.

Chen, G.-G., Qi, X.-M., Guan, Y., Peng, F., Yao, C.-L. and Sun, R.-C., 2016. High strength hemicellulose-based nanocomposite film for food packaging applications. *ACS Sustainable Chemistry & Engineering*, 4(4), pp. 1985–1993. https://doi.org/10.1021/acssuschemeng.5b01252.

Deshavath, N.N., Veeranki, V.D. and Goud, V. V., 2019. Lignocellulosic feedstocks for the production of bioethanol: availability, structure, and composition. In: M. Rai and A.P. Ingle, eds. *Sustainable bioenergy: advances and impacts.* Amsterdam: Elsevier. Ch. 1. https://doi.org/10.1016/B978-0-12-817654-2.00001-0.

Grand View Research, 2020. *Food packaging market size, share & trends analysis report, 2020–2027.* [online] Available at: <https://www.grandviewresearch.com/industry-analysis/food-packaging-market> [Accessed 21 Novemer 2021].

Hartman, J., 2006. *Hemicellulose as barrier material.* Licentiate thesis. Kungliga Tekniska Högskolan, Stockholm.

Honarvar, Z., Hadian, Z. and Mashayekh, M., 2016. Nanocomposites in food packaging applications and their risk assessment for health. *Electronic Physician*, 8(6), pp. 2531–2538. https://doi.org/10.19082/2531.

Hu, L., Du, M. and Zhang, J., 2018. Hemicellulose-based hydrogels present status and application prospects: a brief review. *Open Journal of Forestry*, 08(1), pp. 15–28. https://doi.org/10.4236/ojf.2018.81002.

Ingle, J.D. and Crouch, S.R., 1988. *Spectrochemical analysis.* Englewood Cliffs, NJ: Prentice Hall.

International Organization for Standardization, 2019. *ISO 13468-1:2019 Plastics – Determination of the total luminous transmittance of transparent materials – Part 1: Single-beam instrument.* Geneva: ISO.

IGT team, 2021. *IGT Testing Systems: surface characteristics.* [online] Available at: <https://www.igt.nl/laboratory-testing/surface-characteristics/> [Accessed 9 November 2021].

Kalia, S., Dufresne, A., Cherian, B.M., Kaith, B.S., Avérous, L., Njuguna, J. and Nassiopolous, E., 2011. Cellulose-based bio- and nanocomposites: a review. *International Journal of Polymer Science*, 2011: 837875. https://doi.org/10.1155/2011/837875.

Kunlere, I.O., Fagade, O.E. and Nwadike, B.I., 2019. Biodegradation of low density polyethylene (LDPE) by certain indigenous bacteria and fungi. *International Journal of Environmental Studies*, 76(3), pp. 428–440. https://doi.org/10.1080/00207233.2019.1579586.

Lopez, C.G. and Richtering, W., 2021. Oscillatory rheology of carboxymethyl cellulose gels: influence of concentration and pH. *Carbohydrate Polymers*, 267: 118117. https://doi.org/10.1016/j.carbpol.2021.118117.

Ma, R., Pekarovicova, A. and Fleming, P. D., 2018. Biopolymer films from glucomannan: the effects of citric acid crosslinking on barrier properties. *Journal of Print and Media Technology Research*, 7(1), pp. 19–25. https://doi.org/10.14622/JPMTR-1802.

Makkonen, L., 2016. Young's equation revisited. *Journal of Physics: Condensed Matter*, 28(13): 135001. https://doi.org/10.1088/0953-8984/28/13/135001.

Morrison, F.A., 2001, *Understanding rheology.* Oxford, New York: Oxford University Press.

Nechita, P. and Roman, M., 2020. Review on polysaccharides used in coatings for food packaging papers. *Coatings*, 10(6): 566. https://doi.org/10.3390/COATINGS10060566.

Now Foods, n.d. Now foods, glucomannan, pure powder, 8 oz (227 g). *Foodpharmacy Blog*, [blog]. Available at: <https://foodpharmacy.blog/now-foods-glucomannan-2.html> [Accessed 21 November 2021].

Pal, L., Joyce, M.K. and Fleming, P.D., 2006. A simple method for calculation of the permeability coefficient of porous media. *Tappi Journal*, 5(9), pp. 10–16.

Picout, D.R. and Ross-Murphy, S.B., 2003. Rheology of biopolymer solutions and gels. *The Scientific World Journal*, 3: 524215, pp. 105–121. https://doi.org/10.1100/tsw.2003.15.

Sasmitaloka, K.S., Arif, A.B., Juniawati, Winarti, C., Hayuningtyas, M., Ratnaningsih and Richana, N., 2019. Xylan production from corn cobs for osolation of xylanase-producing bacteria. In: *IOP Conference Series: Earth and Environmental Science, 309: 2nd ICAPHP.* Kuta, Bali, Indonesia, 29–31 August 2018. IOP Science. https://doi.org/10.1088/1755-1315/309/1/012066.

Scheller, H.V. and Ulvskov, P., 2010. Hemicelluloses. *Annual Review of Plant Biology*, 61(1), pp. 263–289. https://doi.org/10.1146/annurev-arplant-042809-112315.

Shi, X.-D., Yin, J.-Y., Cui, S.W., Wang, Q. and Nie, S.-P., 2020. Plant-derived glucomannans: sources, preparation methods, structural features, and biological properties', *Trends in Food Science & Technology*, 99, pp. 101–116. https://doi.org/10.1016/j.tifs.2020.02.016.

Technical Association of the Pulp and Paper Industry, 2010. *TAPPI T 555 Roughness of paper and paperboard (Print-surf method)*. Peachtree Corners, GA: TAPPI.

Triantafillopoulos, N., 1988. *Measurement of fluid rheology and interpretation of rheograms*. 2nd ed. Novi, Michigan: Kaltec Scientific.

Wang, K., Wu, K., Xiao, M., Kuang, Y., Corke, H., Ni, X. and Jiang, F., 2017. Structural characterization and properties of konjac glucomannan and zein blend films. *International Journal of Biological Macromolecules*, 105, pp. 1096–1104. https://doi.org/10.1016/j.ijbiomac.2017.07.127.

Wu, C., Li, Y., Du, Y., Wang, L., Tong, C., Hu, Y., Pang, J. and Yan, Z., 2019. Preparation and characterization of konjac glucomannan-based bionanocomposite film for active food packaging. *Food Hydrocolloids*, 89, pp. 682–690. https://doi.org/10.1016/j.foodhyd.2018.11.001.

Yoshimura, M., Takaya, T. and Nishinari, K., 1998. Rheological studies on mixtures of corn starch and konjac-glucomannan. *Carbohydrate Polymers*, 35(1–2), pp. 71–79. https://doi.org/10.1016/S0144-8617(97)00232-4.

Zhong, L.-X., Peng, X.-W., Yang, D., Cao, X.-F. and Sun, R.-C. 2013. Long-chain anhydride modification: a new strategy for preparing xylan films. *Journal of Agricultural and Food Chemistry*, 61(3), pp. 655–661. https://doi.org/10.1021/jf304818f.

Appendix: Frequency sweep for glucomannan–xylan filmogenic solutions
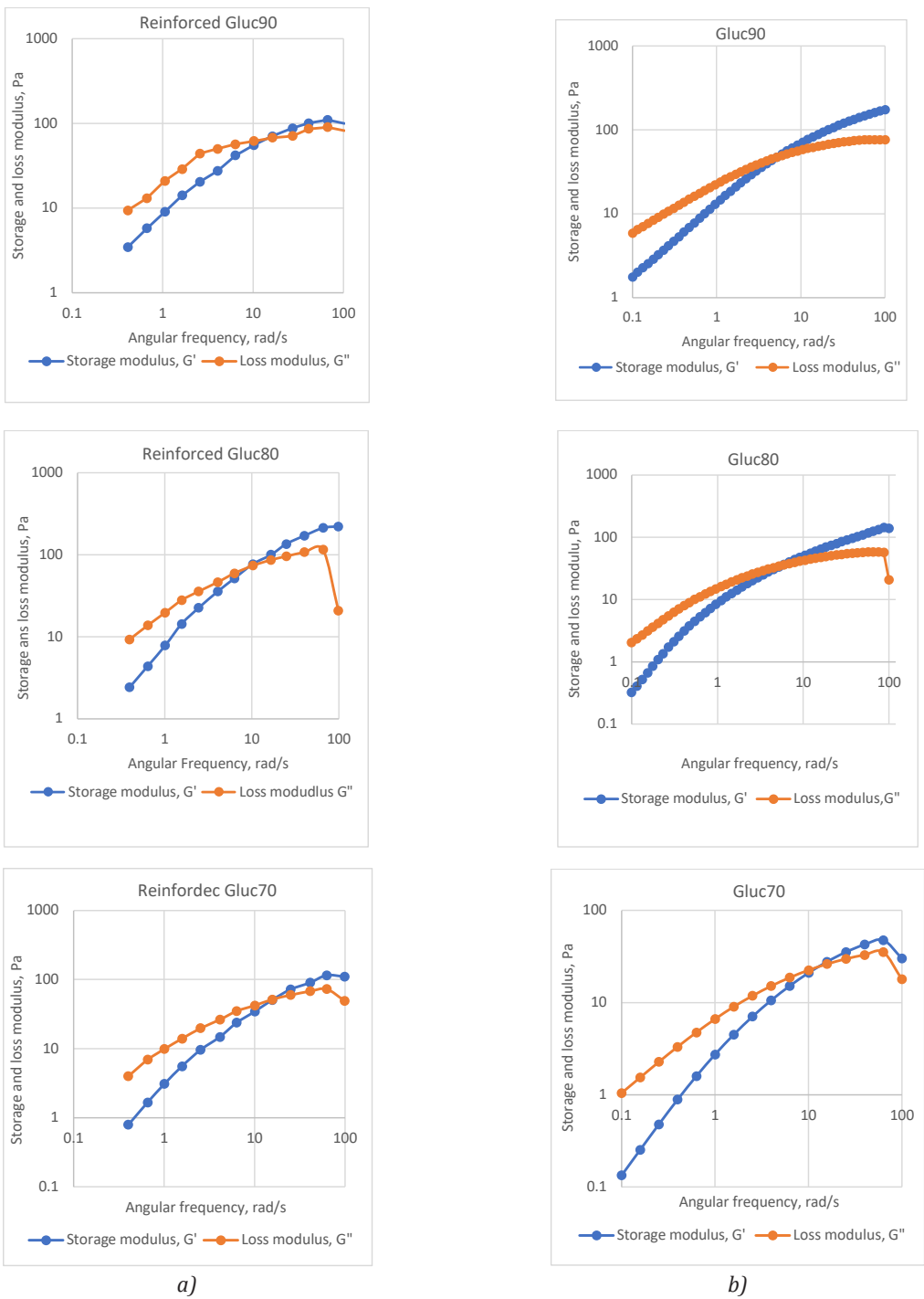

*Figure A1: Frequency sweep for glucomannan–xylan filmogenic solutions,
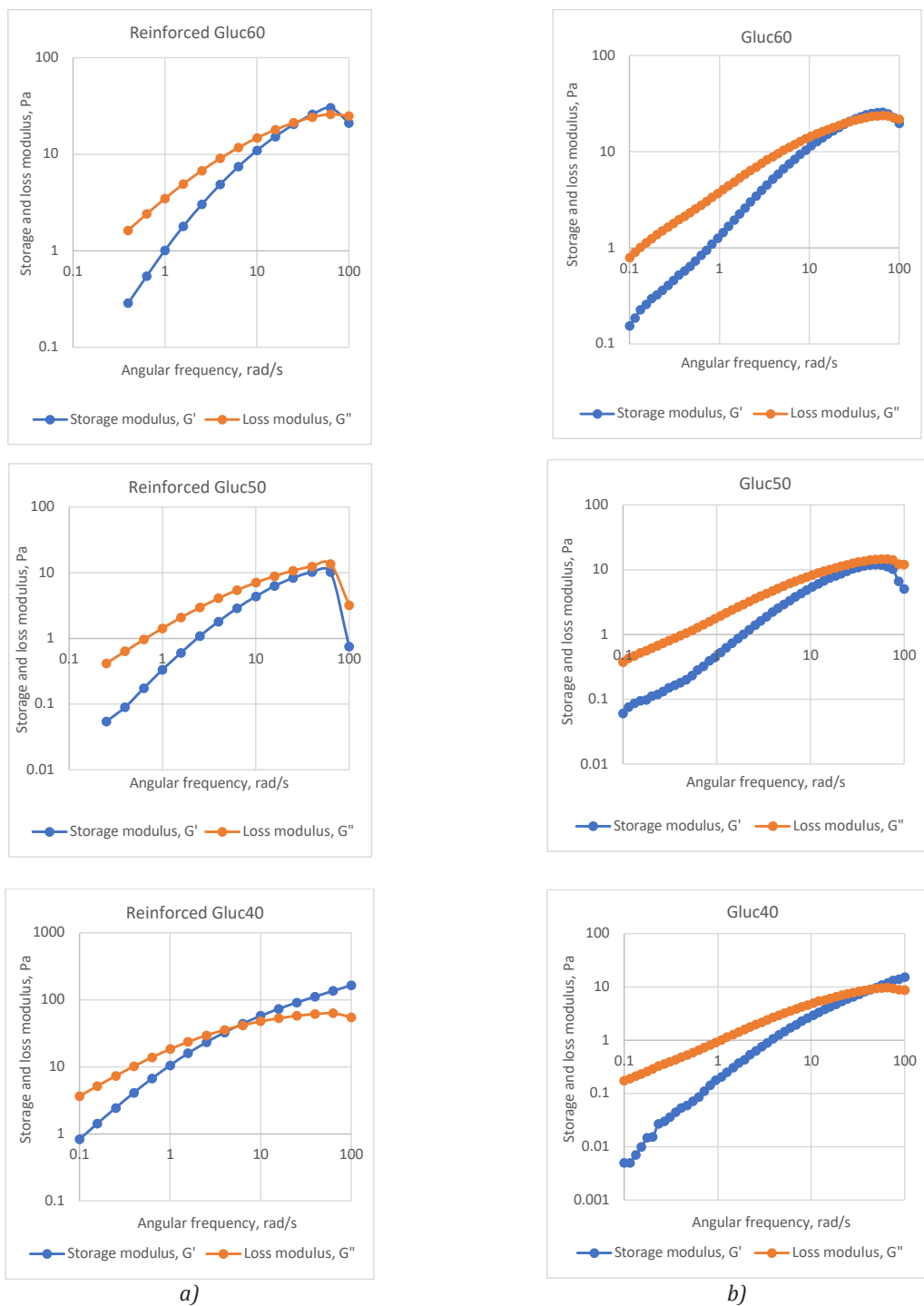reinforced with NFC (a) and without NFC (b) – part 1*

Figure A1: Frequency sweep for glucomannan–xylan filmogenic solutions,
reinforced with NFC (a) and without NFC (b) – continued

TOPICALITIES

Edited by Markéta Držková

CONTENTS

News & more

New Technical Committees and recent publications of CIE

In 2021, three new Technical Committees (TCs) of the International Commission on Illumination (CIE) were established. The first one, CIE TC 2-95 Measurement of Obtrusive Light and Sky Glow, is a part of Division 2, Physical Measurement of Light and Radiation. It aims to propose appropriate guidelines and provide examples for metrics, measurement methods and corresponding instrument specifications, applicable, e.g., to light pollution assessment and research. The other two TCs work under Division 3, Interior Environment and Lighting Design. While CIE TC 3-59 The Integration of Daylight and Electric Lighting – Photometric, Colorimetric and Radiometric Requirements for the Spectral Design of Indoor Lighting deals with a lighting design approach that considers human comfort and wellbeing together with energy efficiency, the purpose of CIE TC 3-60 Spectral Daylight Characteristics is to review geographical, seasonal and time-of-day variations in the spectral power distribution of daylight for 380–780 nm, propose an updated approach for the calculation of D illuminants at a nominal correlated colour temperature (now defined in CIE 15:2018 Colorimetry, 4th edition), and provide spectral information for CIE standard general sky types.

The publications issued during the past 12 months include CIE x048:2021, Proceedings of the Conference CIE 2021 held last October as a 3-day online event. The proceedings include 107 papers of invited, oral, poster and workshop presentations, which are also available individually in the CIE Webshop. About a third of them are the open-access ones, including those dealing with new approaches to spectral measurement and classification utilising modern machine learning methods, the development of a new goniospectrophotometer for measurement of the bidirectional reflectance distribution function on submillimetre surfaces, chromatic discrimination thresholds in the CAM02-UCS and CAM16-UCS colour spaces, determining the reference white in a complex virtual reality environment, optimising camera placement for a luminance-based shading control system in a real office environment, testing sensitivity to differences in colour fidelity and changes in illuminance for better lighting optimisation, changes in perceived chroma and hue angle at high illuminance levels due to the Hunt effect, and the role of daylight in seat preferences of library users, among others, and the invited paper presenting progress in the inter-disciplinary development of measures for reducing the adverse effects of artificial light at night. In addition, the Abstract Booklet of the Conference CIE 2021 is freely available on the CIE website.

Another document offered for free is the Technical Note CIE TN 012:2021 Guidance on the measurement of temporal light modulation of light sources and lighting systems, prepared by the corresponding committee of Division 2. It provides recommendations on measurement protocols to measure periodic waveforms and light modulations and, to some extent, also non-periodic signals, considering the differences between field and laboratory measurements, measurement equipment and evaluation, as well as reporting of results and measurement uncertainty. It is intended as a guide for the correct measurement of new metrics, like the stroboscopic visibility

Fogra research projects and other news in 2021

Among the projects ending in 2021, four dealt with colour. The outputs of the one focused on the characterisation of colour gamut and standardised colour communication in multi-primary printing include the Fogra ECG-7C test form with the evaluation table for media wedge developed for seven-colour printing, together with the characterisation dataset and ICC-profile of FOGRA55, the exchange colour space based on CMYKOGV. The project that concerned with the colour appearance in full-colour 3D printing explored e.g. deep learning models for optical characterisation of multi-material 3D printers and compared simulated and measured remission spectra. Another project aimed to establish suitable characteristic values for paper in order to reduce the presetting time in high-speed inkjet printing while ensuring reliable colour print production; it involved extensive laboratory testing and printing a variety of paper with different machines. The fourth of these projects employed modelling of changes in colour appearance due to transparent top layer, which considered its thickness, refractive index, the spectral characteristics of the involved surfaces and the lateral spread of the light, to allow reliable colour profiling for coated or laminated products. The fifth project ending in 2021 aimed to further improve a cyclical fatigue analysis of smart cards and thus the predictability of their service life using a standardised method, which can also contribute to their optimised design and manufacturing.

The topics of the ongoing projects include the development of a machine learning framework for dynamic image style evaluation and the improvement of textile colour communication (see also

JPMTR Vol. 9, No. 4). The third one deals with a further reduction of waste and thus also the related CO_2 emissions through paper-dependent pre-adjustment of sheet-fed offset presses based on a new paper characteristic value enabling predictions of solid tone densities and tone value increases, which is to be established from laboratory prints and print tests on a production press.

Three of the new projects started in 2021 are also concerned with offset printing, materials and the environment. One deals with the use of 3D-printed, biodegradable hydrogels for on-demand inactivation of microbial contamination in the dampening solution circuit of presses, another one investigates material compatibility and deinking of mineral oil-free newspaper inks, and the last one aims to develop a standard for seven-colour offset packaging printing. Further, two new projects focus on the uncoated printing papers for high-speed inkjet applications, namely on their properties important for print finishing. While one aims to develop the evaluation method for the perfect binding capability, the other investigates the material and process parameters of foil laminations for the prediction of thermal and mechanical resistance. Finally, the new project in security applications develops standardised performance tests to optimise performance and interoperability in near-field communication technology.

The outcomes of Fogra research are reflected also in its knowledge exchange and sharing activities, such as in the Fogra PSD 2022 handbook with the guidelines for the entire digital printing workflow. The main changes in this new edition, which should be available soon, include coverage of the multicolour printing with the expanded colour gamut (ECG), the introduction of media wedges for RGB and ECG, addition of recent Fogra standards (FOGRA55 to FOGRA60), an overview of the updated tolerances together with the previous tolerance schemas, presentation of the certifications related to ProcessStandard Digital, and the barcode evaluation guidelines.

measure, used in regulations that are coming into force in several regions. New technical reports include CIE 243:2021 Discomfort glare in road lighting and vehicle lighting, CIE 245:2021 Optical safety of infrared eye trackers applied for extended durations, CIE 247:2021 Guide for the gonioradiometric measurement of upper air ultraviolet germicidal irradiation luminaires, and the two presented in more detail below.

CIE 244:2021 – Characterization of imaging luminance measurement devices (ILMDs)

This document prepared under Division 2 deals with imaging luminance measuring devices, also referred to as video photometers, imaging photometers or luminance (measuring) cameras, which are used to record images of luminous and illuminated scenes enabling their complex, spatially resolved analysis. These devices find application in many areas, for example, in the characterisation of light sources and displays, analysis of outdoor and indoor lighting, night vision design, etc. On almost 60 pages, the technical report describes the elements, function, characterisation and calibration of imaging luminance measuring devices, providing guidelines for their use and defining the appropriate quality parameters, such as responsivity uniformity, edge function and shutter and aperture repeatability.

CIE 246:2021 – Colour gamuts for output media

This technical report providing methods for computing and communicating colour gamuts for output devices such as printers and displays was prepared under Division 8, Image Technology. It includes a step-by-step procedure for calculating the volume of colour gamut together with the metrics for comparing two colour gamuts, describes methods for visualisation of a 3D colour gamut surface and presents different methods for defining a colour gamut boundary and encoding its description, including the examples for the CxF-based encoding.

Activities towards higher adoption of 3D printing in Sweden

Based on the results of a feasibility study analysing the industrial needs for an open test and demonstration environment for additive manufacturing, which was finished in 2021, RISE (Research Institutes of Sweden) together with 15 industrial and academic partners, including Ericsson, Nikon Metrology Europe, Siemens Energy, Volvo Group, and the Chalmers University of Technology, among others, have recently established the Application Center for Additive Manufacturing as a collaboration platform supporting the development and adoption of additive manufacturing that is seen as a technology important for the transition to a sustainable industry.

In addition, the two-year 3D-Action project, also launched in 2021 and connected with the Application Center for Additive Manufacturing through the shared infrastructure and personnel, should help increase awareness and knowledge about additive manufacturing and its benefits for small and medium-sized companies in the Västra Götaland region. The approach employs the dedicated seminars providing an insight into the 3D printing technology and its opportunities based on the experiences of companies that already have used the technology for some time, the feasibility studies conducted in the interested companies, and, for the companies with an identified potential in adopting the additive manufacturing technology, the in-depth and hands-on training and education.

Bookshelf – J. Print Media Technol. Res. – Vol. 10 No. 4 (2021), 265–270

265

Bookshelf

Information
A Historical Companion

This comprehensive volume explores the approaches to documenting facts and knowledge and sharing information, as well as the related concepts, practices and technologies. Contributed by an international team of more than a hundred experts, the book covers the development from ancient times to the present information age.

A third of the book presents a collection of 13 chapters that provide an insight into the evolution of acquiring, processing, storing and distributing information in premodern regimes, the medieval Islamic world, early modern East Asia and Europe, the interconnecting world in the 16th century, the role of writing offices, periodicals, the commercialisation of information, capitalism, 19th-century media technologies, and networking in the modern world. This part also discusses publicity, propaganda, public opinion, communication, computation, and search. The second part offers over 100 alphabetical entries on selected topics from accounting to xylography. These deal, among others, with algorithms, censorship, computers, data, digitisation, encrypting/decrypting, error, files, forgery, indexing, journals, notebooks, printed visuals, proofreaders, readers, recording, reference books, scrolls, teaching, telecommunications, and travel. In addition, the volume includes a glossary and index, as well as recommendations for further reading.

The book covers all kinds of communication media, including social media – not only the currently dominating ones, such as Facebook, Instagram and Twitter, but also the past or more focused ones, namely Friendster, Grindr, Match, MySpace and Tinder. Naturally, printing is mentioned many times throughout the whole text. Besides its use for advertising and production of books, diagrams, images, manuals, maps, newsletters, newspapers, periodicals, sales catalogues, etc., or connection with technology, such as cameras, colour reproduction, hot metal, letterpress, movable type and linotype, lithography, photocopiers, portable presses, printing on rolls, steam, stereotype, and woodblock printing, the book explores its relationship with the art of memory, bibliography, capitalism, Catholics, commodification, communication, ethnography, excerpting, Google Print, information policy, intellectual property, journalism, letters, libraries, literacy, merchants, money, networks, office practices, plagiarising, political reporting, privacy, publication, regulation, scribes, search, surveilling, translating, typography, and other. The book also describes its development and impacts in different parts of the world. Other topics treated in detail are materials, especially papyrus, parchment, silk and paper, devices used for communication, various aspects and applications of digital technologies, Silicon Valley, the projects of Google, important persons, such as Gutenberg and Claude Shannon, professions, e.g. scribes and secretaries, the mutual relationship between information and science, the role of organisations such as the National Science Foundation and the Royal Society, quantification and statistics, and much more.
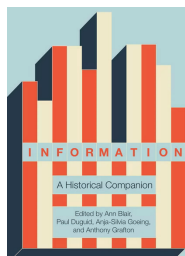
Editors: Ann Blair, Paul Duguid, Anja-Silvia Goeing, Anthony Grafton

Publisher: Princeton University Press
1st ed., January 2021
ISBN: 978-0-691-17954-4
924 pages, 43 images
Hardcover
Available also as an eBook

Environmental and Financial Performance Evaluation in 3D Printing Using MFCA and LCA

Authors: Tiago Y. Kamiya, Marcell M. Corrêa Maceno, Mariana Kleina

Publisher: Springer
1st ed., March 2021
ISBN: 978-3030696948
77 pages, 45 images
Softcover
Also as an eBook

Part of the SpringerBriefs in Applied Sciences and Technology series, this book deals with the methodology for 3D printing performance evaluation. It defines seven main steps comprising the identification of the problem and definition of printing parameters, definition of a product to be printed, preparation of printing process flow diagram, definition of the printed product life span, definition and collection of data for printed product life-cycle assessment (LCA) and material flow cost accounting (MFCA), and finally the comparative assessment of 3D printing financial and environmental performance.

The application of the proposed approach is presented for a real case of a 3D-printed clearance gauge with the comparison of polylactic acid and polyethylene polyterephthalate glycol.

Multimedia Security
Algorithm Development, Analysis and Applications

*Editors: Kaiser J. Giri, Shabir A. Parah, Rumaan Bashir, Khan Muhammad*

Publisher: Springer
1st ed., January 2021
ISBN: 978-9811587108
314 pages, 134 images
Hardcover
Also as an eBook

Three parts of this new reference present the methods reducing threats due to insecure multimedia communication – security using cryptography and chaotic theory, information embedding for secure data communication and authentication, and security in the Internet of Things and enterprise driven by Big Data.

For the Love of Letterpress
A Printing Handbook for Instructors and Students

This handbook makes clear why letterpress still attracts students and how it helps to master typography. The authors share their skills and experience, covering all steps in the production of letterpress prints and different aspects to consider. The well-illustrated text clearly explains all terms and guides through the whole process while providing an insight into reasons for dos and don'ts. After elucidating the fascination of letterpress and the value of its historical legacy, the authors introduce the basics in terms of measurement units, the lay of the case, spacing and leading, the procedure from type setting and alignment to tying up the form, proofing and press operation, up to cleaning the press after printing. They also describe presses and discuss the choice of ink and paper for proofing and printing, lockup, checking the impression, make-ready, registering multiple colours and editioning. One chapter presents various relief matrices. Building upon these fundamentals, the following chapter provides examples of contemporary processes and experimental techniques, e.g. split fountain printing, debossing and intentional ghosting. In three chapters, the authors advise how to create a concept, envision the object considering, among others, the relationship of content and structure, as well as appropriate typefaces, paper and colours, and assess the resulting work. The last chapter before the closing part is new and presents a collection of letterpress assignments to try. Same as the first edition published in 2013, also this new one received an American Graphic Design Award from Graphic Design USA.
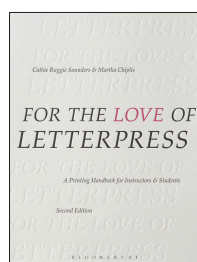
Authors: Cathie Ruggie Saunders, Martha Chiplis

Publisher: Bloomsbury Visual Arts
2nd ed., August 2019
ISBN: 978-1-350-05128-7
208 pages, 242 images
Softcover
Available also as an eBook

Screenprinting on Textiles
The Complete Guide

This new book is also written by an expert with long and rich experience, embracing both traditional and contemporary techniques and approaches. It introduces the fundamentals of printing on textiles, designing for print, making stencils, carrying out make-ready, and printing. In the next chapters, it shows how to work with dye pastes and colourants, achieve the required texture, shape, shine, embellish and finish, utilise scale and repeat, and shares other practical tips and recommendations.

Author: Sue Westergaard

Publisher: The Crowood Press
1st ed., November 2020
ISBN: 978-1-78500-753-8
224 pages
Hardcover
Available also as an eBook

Bookshelf – J. Print Media Technol. Res. – Vol. 10 No. 4 (2021), 265–270

267

The Graphic Design Reader

This anthology, "dedicated to graphic design students everywhere", brings 90 articles that are well organised into seven thematic parts, each of which is framed by the introduction and recommendations for further reading. Written content is complemented by 160 figures. The first part, 'History of graphic design and graphic design history', is the most extensive one, beginning with essays by W. A. Dwiggins and William Morris and ending with the article by Chuck Byrne and Martha Witte exploring the concept of deconstruction. Two sections deal with graphic design from the 19th century to 1980 and from the 1980s to the present, while the third one explores the evolution of graphic design isms. The following six parts focus on 'Education and the profession', 'Type and typography', 'Graphic design, critical writing and practice', 'Political and social change', 'Changing visual landscapes' and 'Graphic design futures'. Each of them collects about a dozen of articles split into two sections. Some of them are visual essays: the one presenting a subjective family tree of (mostly) American graphic designers (1960–2011) in Part 2, 'This year there is no manifesto', 'Design and reflexivity' and the one showcasing the development of hip-hop typographic ornaments in Part 5, and 'RCA graphic design: 1960s–2010s' in Part 7. The volume concludes with an epilogue by the editors, followed by a rich bibliography and index.
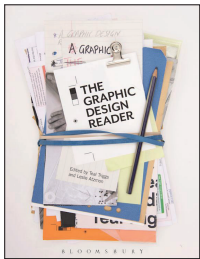
Editors: Teal Triggs, Leslie Atzmon

Publisher: Bloomsbury Visual Arts
1st ed., February 2019
ISBN: 978-1-4725-3620-4
997 pages
Hardcover

Data Sketches
A journey of imagination, exploration, and beautiful data visualizations

This book is a part of AK Peters Visualization Series, which now includes seven books (also Visualizing with Text presented in JPMTR Vol. 10, No. 2). In this new one, the authors present their approaches to creative coding in 24 data visualisation projects on 12 different, more or less abstract themes: movies, Olympics, travel, presidents and royals, books, music, nostalgia, nature, culture, community, myths and legends, and fearless. After the opening part explaining the concept and introducing technologies and tools, almost 400 pages of the main part track for each project the whole process – from data gathering and sketching to coding and resulting data visualisation graphics. For better insight, the illustrations include drafts and notes.

Authors: Nadieh Bremer, Shirley Wu

Publisher: CRC Press
1st ed., February 2021
ISBN: 978-0-367-00012-7
428 pages, 132 images
Hardcover
Available also as an eBook
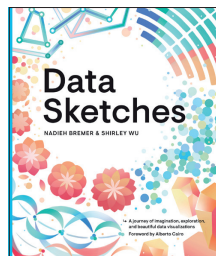
Perspectives on Design and Digital Communication II
Research, Innovations and Best Practices

Editors: Nuno Martins, Daniel Brandão, Fernando Moreira da Silva

Publisher: Springer
1st ed., May 2021
ISBN: 978-3030758660
461 pages, 131 images
Hardcover
Also as an eBook

This volume brings 28 chapters with invited papers and contributions based on the best papers presented at Digicom 2020 (for the conference proceedings, see JPMTR Vol. 9, No. 4). It includes two review articles dealing with the design of visual interfaces for seniors, papers discussing the role of observation and intuition in design practice and research, the future of design doctoral studies in the context of the 4th industrial revolution, the process of modelling a digital font to a 3D-printed letterpress type, design-led branding, functional graphic design for musical writing, a concept of data artification, and more.

Understanding – Combining Typefaces
Typeface combination as a stimulus in typography

Author: Philipp Stamm

Publisher: Birkhäuser
1st ed., June 2021
ISBN: 978-3035611144
360 pages, 275 images
Hardcover

This new book helps to understand the typeface features most important for creating a functional and aesthetic design. Besides explaining the basics, it provides historical insight and revised classification of fonts. The relevant characteristics and factors to consider when combining typefaces, benefiting from a systematic analysis of analogy and contrast, are clearly illustrated in numerous examples. The German edition was published at the end of 2020.

Organic Semiconductors for Optoelectronics

Editor: Hiroyoshi Naito

Publisher: Wiley
1st ed., August 2021
ISBN: 978-1119146100
384 pages
Hardcover
Also as an eBook

In this new book on organic semiconductors, the first nine chapters review the current knowledge of their electronic structures, mechanisms of electronic transport, theoretical treatment of optical properties, light absorption and emission properties, and characterisation of their properties using impedance spectroscopy, time-of-flight measurement, microwave and terahertz spectroscopy, electron spin resonance spectroscopy, and second harmonic generation spectroscopy. The remaining six chapters present the advances and future trends in organic field-effect transistors, organic light-emitting diodes and organic photovoltaics.

Sustainability in the Textile and Apparel Industries
Production Process Sustainability

*Editors: Subramanian S. Muthu,
Miguel A. Gardetti*

Publisher: Springer
1st ed., April 2020
ISBN: 978-3030385446
222 pages, 157 images
Hardcover
Also as an eBook

The first chapter of this new book deals with printing on textiles using sustainable natural dyes and pigments. The following chapters cover innovative technologies for sustainable textile colouration, patterning and surface effects, cellulose textile colouring with clay particles, ozone as an alternative oxidant, sustainable textile processing with zero water utilization, and other recent developments in sustainable approaches applicable in textile dyeing, finishing and spinning.

Organic Electronics for Electrochromic Materials and Devices

The author of this new volume brings a comprehensive account of organic electrochromic materials and their applications. The first chapter provides a brief overview of six generations of electrochromic materials and introduces their key parameters – electrochromic contrast, switching time, colouration efficiency, optical memory, and stability. Ten chapters then discuss in detail advances in polymer electrolytes for electrochromic applications, electrochromic small-molecule materials, conjugated polymers, triarylamine-based polyimides and polyamides, and metallo-supramolecular polymers, electrochromism of viologens and metallohexacyanates, electrochromism based on metal–organic frameworks, covalent organic frameworks and porous structures, especially nanostructures, and organic electroluminochromic materials. The following two chapters are dedicated to organic photoelectrochromic devices and the utilisation of organic electrochromic devices in smart windows, dimmable rearview mirrors, sensors, displays and other applications. The next one reviews commercial organic electrochromic materials and the related patents. The last chapter discusses the main challenges for the commercialisation of organic electrochromic materials, in particular in terms of their long-term stability, the mechanical stability of flexible devices and their encapsulation, and large-area process technologies, including inkjet printing, spray coating and screen printing.

Author: Hong Meng

Publisher: Wiley-VCH
1st ed., July 2021
ISBN: 978-3-527-34871-8
528 pages
Hardcover
Available also as an eBook
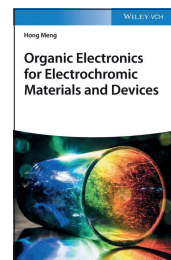
Applications of Biotechnology for Sustainable Textile Production

This new book begins with an overview of textile fibres and forms. The second chapter provides the techno-economic analysis of current processes in the textile industry considering price components, plant capacity, costs, hazards, wages, gender equality, law requirements and many other factors. In seven chapters, it reviews biotechnological approaches in desizing, scouring, sustainable pre-treatment, dyeing, printing and finishing of textile materials, including the advanced flame-retardant, antimicrobial, crease-resistant and UV-resistant finishes utilising biochemicals. The next chapter presents biotechnological and nano-biotechnological approaches in the treatment of textile effluents, followed by a conclusion and future scope.

Editor: O. L. Shanmugasundaram

Publisher: Woodhead Publishing
1st ed., September 2021
ISBN: 978-0-323-85651-5
276 pages
Softcover
Available also as an eBook

Bookshelf – J. Print Media Technol. Res. – Vol. 10 No. 4 (2021), 265–270

269
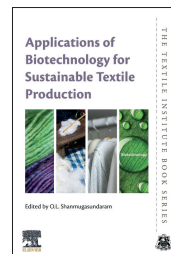
Bookshelf

Academic dissertations

In Situ Investigation of the Highly Dynamic Interfacial Instability in the Cylinder Gap

The study of the phenomena occurring in the gap between the substrate and the printing forme of a gravure printing machine carried out in this thesis contributes to the research of transport and wetting processes for the production of thin, homogeneous and closed layers, which is important for functional printing. In particular, the aim was to provide an in situ insight into the printing nip to increase understanding of fluid splitting and the formation of finger-shaped structures. The work employed a high-speed camera capturing the images of the printing forme surface and the ink layer formed during the operation of an upscaling laboratory printing system. The acquired image sets were processed to automatically identify the finger-shaped structures and determine the mean finger frequency as a characteristic quantity of the highly dynamic interfacial instability to investigate the influence of the printing speed and the geometric properties of the printing forme. The dissertation brings a comprehensive and well-illustrated account of the study. It provides the background on the gravure printing process and printing forme, rheology of fluids, fluid splitting and viscous finger formation, camera measurement technology, and image data processing. Next, it details the experimental setup and characteristics of its components – the printing system, printing forme, glass substrate, optical substrate carrier, high-speed camera, light source and diffuser, along with important considerations regarding the exact setting of the substrate guide height, the depth of field of the optical detection system and the maximum printing speed. The following chapters describe the experimental design and evaluation method, present the obtained results and discuss the fluid-splitting regime, scaling law for the mean finger frequency and limitations of the study. While the dependence of the mean finger frequency on the printing speed was not observed, nor its dependence on the cell volume, the results showed a significant influence of the screen frequency. The revealed lock-in phenomenon is explained by the contact between the substrate and the printing forme, which is not assumed in the existing models describing flow profiles in the cylinder gap.

Formulation of 3D Printable Edible Materials for Innovative Recipes

Food 3D printing is a technology with great development potential in the context of a growing trend of personalised food. This thesis focused on the formulation and production of food materials with the aim to gain an understanding of the mechanisms of their transformation during mechanical and heat treatment to be able to propose a specification of ingredients, printability indicators and processing routes for the production of printed foods of varying texture and composition. The approach employs the use of wheat flour as a starting raw material and its combination with sucrose, sunflower oil, milk, stirred yoghurts, and fruit and vegetable purees as the complementary ingredients fulfilling the requirement on the lowest level of processing. The research investigated the structuring mechanisms of wheat flour dough in dependence on the water content in a higher concentration range than that usually studied and the number and sequence of mechanical and heat treatment operations, the options to modify material rheology to

ensure good printability, the influence of various complementary ingredients on the structuring of the cereal material and its printability, the levers for ensuring good print quality, and the possibility to use drying as a post-printing step for modification of the mechanical properties of the printed food. The first step in the research design comprised the study of the dough structure, followed by characterisation of its rheology and determination of its printability.

The first part of the extensive dissertation reviews the state of the art in the field considering 3D printing, cereal material formulation and behaviour of dispersions. The second part defines the objectives and strategy and the third one provides experimental details. The fourth part presents the results of the experiments comprising the structuring of wheat flour doughs highly hydrated by mechanical or thermomechanical treatment, diversification of the cereal material composition by incorporation of ingredients of both plant and animal origin, and optimisation of 3D printing and drying methods. The fifth part reviews the identified technological routes and discusses the role of water and solid ingredients along with considerations for extrusion-based 3D printing of dense particulate systems.

Doctoral thesis – Summary

Author:
Devin John Roach

Speciality field:
Mechanical Engineering

Supervisor:
H. Jerry Qi

Defended:
*28 April 2021, Georgia Institute
of Technology, Woodruff School of
Mechanical Engineering
Atlanta, Georgia, USA*

Contact:
djroach@sandia.gov

Further reading:
http://hdl.handle.net/1853/64721

Developing Intelligent Structures and Functional Devices Using Novel Smart Materials and Multi-Material Multi-Method (m⁴) 3D Printing

Despite its extensive development, 3D printing still has great potential for further growth. The research in this thesis explores novel manufacturing methods, smart materials and structural design combining multiple materials to print a variety of multi-functional components and devices. After a concise overview of relevant advances in the field, the dissertation presents four research projects. The first one comprised building a multi-material multi-method (m4) 3D printer that integrates four deposition technologies, namely inkjet printing, fused filament fabrication, direct ink writing, and aerosol jetting, in combination with robotic pick-and-place arms and modules for photonic and UV curing. The work describes the hardware, its control, required coordinate transformations and software development. It demonstrates the functionality of the multi-material printer on a 3D-printed wheel, three different interface shapes and soft pneumatic actuators. Also, it presents m4 3D printing with implemented machine vision. The next step comprised the use of the m4 3D printer for electronics manufacturing. The presented examples include a stretchable light ribbon, multi-layer circuit board with vertical interconnect access through conductive lines, digital LED light with the chip assembled into the 3D-printed structure using pick-and-place, thermocouple, triboelectric nanogenerator and fuse. In addition, the chapter discusses surface modifications of parts made by fused filament fabrication and shows an approach based entirely on utilisation of the m4 3D printer where the surface of 3D-printed polyetherimide substrates was modified by inkjet printing poly(ethylene glycol) diacrylate and polyimide. Further, the work presents the m4 3D printer applicability to smart materials development, in particular, the design and fabrication of long fibres of liquid crystal elastomers, further enhanced by the addition of magnetic particles, as well as their use to produce three types of actuators. Finally, the above-described methods and materials were employed in the fabrication of different smart textiles, twined fibres mimicking bicep muscle contraction and relaxation, and a number of directly 4D-printed smart structures, including a hinge, sequentially folding box, soft robotic gripper and hand, tunable antenna device, and also reversible actuators with high stiffness, demonstrated on a shape-reconfigurable torque wrench.

Events – J. Print Media Technol. Res. – Vol. 10 No. 4 (2021), 271–272

271

Events

EI 2022 – IS&T International Symposium on Electronic Imaging

https://www.imaging.org
17–21 & 24–27 January 2022

The second online edition of this event features 17 technical conferences with 16 keynotes, three plenary sessions and a symposium-wide interactive poster session. The plenary speakers of the first week are Eric R. Fossum, presenting a concept of the Quanta Image Sensor (QIS), its state-of-the-art implementations and future applications, and Larry Matthies, highlighting new technologies used in the Perseverance rover and the Ingenuity helicopter in the current Mars mission. The plenary session in the second week offers the lecture by Joyce Farrell, describing the open-source software for simulations helping to design novel imaging systems and generate data for machine learning applications, and a panel discussion on the benefits and risks of virtual reality.

The short courses start on 11 January, in a week before the main programme. The four-day schedule includes 25 courses, in part presented live and in part covered by the EI 2021 recordings. The former is the case for all courses on image quality and the latter for all courses on artificial intelligence and machine learning; both types of courses can be found in the other tracks covering 3D imaging, cameras, sensors, colour science, and more. The recordings of live sessions will be available until 15 May 2022.

SPIE Events

Photonics West 2022

San Francisco, California, USA
22–27 January 2022

After the 2021 virtual edition, the current one is announced as an in-person event. It features over two thousand presentations, a few tens of which are related to printing technology, such as the one dealing with light control corrections in scattering materials for 3D printing and the papers presenting optical waveguides for complex low-cost optical networks printed using flexography and studies of a printed optical transmission path regarding its data transmission behaviour at fast-ethernet rates. In addition, the event is co-located with SPIE AR | VR | MR taking place on 23–25 January.

Smart Structures / Nondestructive Evaluation 2022

Long Beach, California, USA
6–10 March 2022

Applications of printing are represented also among hundreds of papers included in the programme of this event, e.g., those presenting the all-printed flexible and morphing electronics and inkjet-printed electro-adhesive pads.

Ongoing changes in the calendar of events

Some of the events presented in the previous issue had to be postponed or switched to online due to the emergence of the Omicron variant of COVID-19. Digital Print for Packaging (8–9 December 2021) was held in an online format instead of taking place in Amsterdam, Netherlands. Two shows organised by Tarsus Group were postponed: Labelexpo Asia in Shanghai, China, with the new dates to be announced and Gulf Print & Pack in Dubai, UAE, to 24–26 May 2022. Similarly, the new ESMA conference, Industrial Print Integration (IPI) in Düsseldorf, Germany, was cancelled for 2021 and should take place on 17–18 May 2022. Meanwhile, the "Pre-Flight" webinars with IPI speakers can be joined for free on five days from 1 February to 12 April, when also the results of the Paperonics project will be presented.

Among the in-person events that have been planned for the first quarter of 2022, the Optical Document Security conference was postponed from January to be held jointly as Optical & Digital Document Security on 11–13 April in the same venue (Vienna, Austria). The 9th edition of C!print in Lyon, France, postponed from 2021, was shifted once more to 10–12 May 2022. The Colour Management Symposium organised by Fogra was shifted from March to 6–7 July. The recording of Fogra Colour Management Café 33 'Why is colour' is now available online for free.
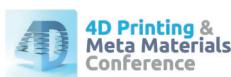
Color22

La Jolla, California, USA
22–25 January 2022

This PRINTING United Alliance event dedicated to achieving accurate and consistent colour again offers a workshop, panel discussion, keynotes, and many lectures on the topic.

4D Printing & Meta Materials Conference

https://www.4dpmmconference.com
22 February 2022

The topics announced for this half-day online event organised by Jakajima include 4D printing of hydrogel materials, the temperature-memory effect in 3D-printed auxetic structures, material programming for 4D printing, 3D-printed soft robotic grippers with integrated metamaterials, development of a new flexible wing concept for unmanned aerial vehicles utilising 4D printing, and more. A few weeks later, on 29–30 March 2022, Jakajima holds the 8th edition of the 3D Medical Printing Series, combining four conferences in the field. It is planned as a hybrid event, which can be joined online or attended live in Veldhoven, The Netherlands.

High Security Printing Latin America

Mexico City, Mexico
14–16 March 2022

The 2022 edition is announced as an on-site event. The attendees of the pre-conference seminars on the first day can learn about the ways to reduce environmental impact, benefits and risks of digitised identity, and security printing in the digital age. The programme of the following conference features over 40 speakers.

InPrint Munich

Munich, Germany
15–17 March 2022

In 2022, the Munich edition of the International Exhibition of Print Technology for Industrial Manufacturing is co-located with the 12th International Converting Exhibition and the International Exhibition for the Corrugated and Folding Carton Industry.

VISIGRAPP 2022
17th International Joint Conference on Computer Vision, Imaging and Computer Graphics Theory and Applications

https://visigrapp.scitevents.org
6–8 February 2022

This established event joining four international conferences covering the theory and applications of computer vision (VISAPP), computer graphics (GRAPP), information visualisation (IVAPP), and human–computer interaction (HUCAPP) is held in a virtual format for the second time, again together with SENSORNETS, the 11th International Conference on Sensor Networks. The technical programme of VISIGRAPP 2022 collects dozens of oral and poster presentations and offers four keynotes: 'Wearable human augmentation' by Roope Raisamo, 'Brain computer interfaces for extended reality' by Fotis Liarokapis, 'The risky business of visualizing known unknowns for decision making with maps' by Sara I. Fabrikant, and 'Neural implicit representations for 3D vision and beyond' by Andreas Geiger.

innoLAE 2022
Innovations in Large-Area Electronics

http://innolae.org
22–24 February 2022

The 8th edition of the annual innoLAE event is also held online for the second time in a row, including the courses on the first day. The conference programme starting on 23 February features four plenary keynote lectures – 'Electronic skins and the next-generation wearables for medical applications' by Takao Someya, 'Soft, skin-interfaced hybrid electronics for clinical-grade wearables' by John Rogers, 'PlasticARM: Challenges of TFT VLSI on a flexible substrate' by John Biggs, and 'Print-in-place and recyclable electronics from nanomaterials' by Aaron Franklin. The schedule includes panel discussions, poster sessions and oral presentations that are split into two tracks, with more than ten invited speakers from academia and leading companies in the field.

LOPEC 2022

Munich, Germany
22–24 March 2022

The 2022 edition of this event dedicated to printed electronics is announced to be held in-person, keeping the proven format with short courses, plenary sessions, conferences covering the business, technical and scientific topics in oral and poster presentations, as well as the trade fair on the last two days with the Start-up Forum, the open OE-A Competition and more. The technical topics include smart and hybrid systems, user interfaces, wearable electronics, biomedical and healthcare applications, upscaling production and manufacturing processes, energy, smart textiles, substrates and encapsulation, circular economy and green electronics, flexible and large-area displays, functional materials, lighting, and 3D structural electronics. The scientific sessions cover advanced materials, strategic devices, innovative processes, smart sensors, and circuit design, simulation and systems.

Journal of
Print and Media Technology
A PEER-REVIEWED QUARTERLY   # Research

Call for papers

The Journal of Print and Media Technology Research is a peer-reviewed periodical, published quarterly by iarigai, the International Association of Research Organizations for the Information, Media and Graphic Arts Industries.

JPMTR is listed in Emerging Sources Citation Index, Scopus, DOAJ – Directory of Open Access Journals, Index Copernicus International, PiraBase (by Smithers Pira), Paperbase (by Innventia and Centre Technique du Papier), NSD – Norwegian Register for Scientific Journals, Series and Publishers.

Authors are invited to prepare and submit complete, previously unpublished and original works, which are not under review in any other journals and/or conferences.

The journal will consider for publication papers on fundamental and applied aspects of at least, but not limited to, the following topics:

⊕ **Printing technology and related processes**
Conventional and special printing; Packaging; Fuel cells, batteries, sensors and other printed functionality; Printing on biomaterials; Textile and fabric printing; Printed decorations; 3D printing; Material science; Process control

⊕ **Premedia technology and processes**
Colour reproduction and colour management; Image and reproduction quality; Image carriers (physical and virtual); Workflow and management

⊕ **Emerging media and future trends**
Media industry developments; Developing media communications value systems; Online and mobile media development; Cross-media publishing

⊕ **Social impact**
Environmental issues and sustainability; Consumer perception and media use; Social trends and their impact on media

Submissions for the journal are accepted at any time. If meeting the general criteria and ethic standards of scientific publishing, they will be rapidly forwarded to peer-review by experts of relevant scientific competence, carefully evaluated, selected and edited. Once accepted and edited, the papers will be published as soon as possible.

There is no entry or publishing fee for authors. Authors of accepted contributions will be asked to sign a Licensing agreement (CC-BY-NC 4.0).

Authors are asked to strictly follow the guidelines for preparation of a paper (see the abbreviated version on inside back cover of the journal).

Complete guidelines can be downloaded from: <http://iarigai.com/publications/journals/guidelines-for-authors/> Papers not complying with the guidelines will be returned to authors for revision.

Submissions and queries should be directed to: journal@iarigai.org

Journal of
Print and Media Technology
A PEER-REVIEWED QUARTERLY
Research

Vol. 11, 2022
Prices and subscriptions

Since 2016, the journal is published in digital form; current and archive issues are available at:
<https://iarigai.com/publications/journals/>.

Since 2020, the journal is published as "open access" publication, available free of charge
for iarigai members, subscribers, authors, contributors and all other interested public users.

A print version is available on-demand. Please, find below the prices charged for the printed Journal,
for four issues per year as well as for a single issue

Regular prices

Four issues, print JPMTR (on-demand)	400 EUR
Single issue, print JPMTR (on-demand)	100 EUR

Subscription prices

Annual subscription, four issues, print JPMTR (on-demand)	400 EUR

Prices for iarigai members

Four issues, print JPMTR (on-demand)	400 EUR
Single issue, print JPMTR (on-demand)	100 EUR

Place your order online at: <http://www.iarigai.org/publications/subscriptions-orders/>
Or send an e-mail order to: office@iarigai.org

Guidelines for authors

Authors are encouraged to submit complete, original and previously un-published scientific or technical research works, which are not under reviews in any other journals and/or conferences. Significantly expanded and updated versions of conference presentations may also be considered for publication. In addition, the Journal will publish reviews as well as opinions and reflections in a special section.

Submissions for the journal are accepted at any time. If meeting the general criteria and ethical standards of the scientific publication, they will be rapidly forwarded to peer-review by experts of high scientific competence, carefully evaluated, and considered for selection. Once accepted by the Editorial Board, the papers will be edited and published as soon as possible.

When preparing a manuscript for JPMTR, please strictly comply with the journal guidelines. The Editorial Board retains the right to reject without comment or explanation manuscripts that are not prepared in accordance with these guidelines and/or if the appropriate level required for scientific publishing cannot be attained.

A – General

The text should be cohesive, logically organized, and thus easy to follow by someone with common knowledge in the field. Do not include information that is not relevant to your research question(s) stated in the introduction.

Only contributions submitted in English will be considered for publication. If English is not your native language, please arrange for the text to be reviewed by a technical editor with skills in English and scientific communications. Maintain a consistent style with regard to spelling (either UK or US English, but never both), punctuation, nomenclature, symbols etc. Make sure that you are using proper English scientific terms. Literal translations are often wrong. Terms that do not have a commonly known English translation should be explicitly defined in the manuscript. Acronyms and abbreviations used must also be explicitly defined. Generally, sentences should not be very long and their structure should be relatively simple, with the subject located close to its verb. Do not overuse passive constructions.

Do not copy substantial parts of your previous publications and do not submit the same manuscript to more than one journal at a time. Clearly distinguish your original results and ideas from those of other authors and from your earlier publications – provide citations whenever relevant.

For more details on ethics in scientific publication consult Guidelines, published by the Committee on Publication Ethics (COPE): <https://publicationethics.org/resources/guidelines>

If it is necessary to use an illustration, diagram, etc. from an earlier publication, it is the author's responsibility to ensure that permission to reproduce such an illustration, diagram, etc. is obtained from the copyright holder. If a figure is copied, adapted or redrawn, the original source must be acknowledged.

Submitting the contribution to the Journal, the author(s) confirm that it has not been published previously, that it is not under consideration for publication elsewhere and – once accepted and published – it will be disseminated and make available to the public in accordance to the Creative Commons Attribution-NonCommercial 4.0 International Public License (CC-BY-NC 4.0), in English or in any other language. The publisher retains the right to publish the paper online and in print form, and to distribute and market the Journal containing the respective paper without any limitations.

B – Structure of the manuscript
Preliminary

Title: Should be concise and unambiguous, and must reflect the contents of the article. Information given in the title does not need to be repeated in the abstract (as they are always published jointly), although some overlap is unavoidable.

List of authors: I.e. all persons who contributed substantially to study planning, experimental work, data collection or interpretation of results and wrote or critically revised the manuscript and approved its final version. Enter full names (first and last), followed by the present address, as well as the E-mail addresses. Separately enter complete details of the corresponding author – full mailing address, telephone number, and E-mail. Editors will communicate only with the corresponding author.

Abstract: Should not exceed 500 words. Briefly explain why you conducted the research (background), what question(s) you answer (objectives), how you performed the research (methods), what you found (results: major data, relationships), and your interpretation and main consequences of your findings (discussion, conclusions). The abstract must reflect the content of the article, including all keywords, as for most readers it will be the major source of information about your research. Make sure that all the information given in the abstract also appears in the main body of the article.

Keywords: Include three to five relevant scientific terms that are not mentioned in the title. Keep the keywords specific. Avoid more general and/or descriptive terms, unless your research has strong interdisciplinary significance.

Scientific content

Introduction and background: Explain why it was necessary to carry out the research and the specific research question(s) you will answer. Start from more general issues and gradually focus on your research question(s). Describe relevant earlier research in the area and how your work is related to this.

Methods: Describe in detail how the research was carried out (e.g. study area, data collection, criteria, origin of analyzed material, sample size, number of measurements, equipment, data analysis, statistical methods and software used). All factors that could have affected the results need to be considered. Make sure that you comply with the ethical standards, with respect to the environmental protection, other authors and their published works, etc.

Results: Present the new results of your research (previously published data should not be included in this section). All tables and figures must be mentioned in the main body of the article, in the order in which they appear. Make sure that the statistical analysis is appropriate. Do not fabricate or distort any data, and do not exclude any important data; similarly, do not manipulate images to make a false impression on readers.

Discussion: Answer your research questions (stated at the end of the introduction) and compare your new results with published data, as objectively as possible. Discuss their limitations and highlight your main findings. At the end of Discussion or in a separate section, emphasize your major conclusions, pointing out scientific contribution and the practical significance of your study.

Conclusions: The main conclusions emerging from the study should be briefly presented or listed in this section, with the reference to the aims of the research and/or questions mentioned in the Introduction and elaborated in the Discussion.

Note: Some papers might require different structure of the scientific content. In such cases, however, it is necessary to clearly name and mark the appropriate sections, or to consult the editors. Sections from Introduction until the end of Conclusions must be numbered. Number the section titles consecutively as 1., 2., 3., ... while subsections should be hierarchically numbered as 2.1, 2.3, 3.4 etc. Only Arabic numerals will be accepted.

Acknowledgments: Place any acknowledgements at the end of your manuscript, after conclusions and before the list of literature references.

References: The list of sources referred to in the text should be collected in alphabetical order on at the end of the paper. Make sure that you have provided sources for all important information extracted from other publications. References should be given only to documents which any reader can reasonably be expected to be able to find in the open literature or on the web, and the reference should be complete, so that it is possible for the reader to locate the source without difficulty. The number of cited works should not be excessive – do not give many similar examples.

Responsibility for the accuracy of bibliographic citations lies entirely with the authors. Please use exclusively the Harvard Referencing System. For more information consult the fifth edition of the Guide to Referencing in the Harvard Style, used with consent of Anglia Ruskin University, released by ARU University Library, available at: <https://library.aru.ac.uk/referencing/harvard.htm>

C – Technical requirements for text processing

For technical requirement related to your submission, i.e. page layout, formatting of the text, as well of graphic objects (images, charts, tables etc.) please see detailed instructions at: <http://iarigai.com/publications/journals/guidelines-for-authors/>

D – Submission of the paper and further procedure

Before sending your paper, check once again that it corresponds to the requirements explicated above, with special regard to the ethical issues, structure of the paper as well as formatting.

Once completed, send your paper as an attachment to: journal@iarigai.org

If necessary, compress the file before sending it. You will be acknowledged on the receipt within 48 hours, along with the code under which your submission will be processed.

The editors will check the manuscript and inform you whether it has to be updated regarding the structure and formatting. The corrected manuscript is expected within 15 days.

Your paper will be forwarded for anonymous evaluation by two experts of international reputation in your specific field. Their comments and remarks will be in due time disclosed to the author(s), with the request for changes, explanations or corrections (if any) as demanded by the referees.

After the updated version is approved by the reviewers, the Editorial Board will decide on the publishing of the paper. However, the Board retains the right to ask for a third independent opinion, or to definitely reject the contribution.

Printing and publishing of papers, once accepted by the Editorial Board, will be carried out at the earliest possible convenience.

4-2021

The journal is publishing contributions
in the following fields of research

- Printing technology and related processes
- Premedia technology and processes
- Emerging media and future trends
- Social impacts

For details see the Mission statement inside

JPMTR is listed in

- Emerging Sources Citation Index
- Scopus
- DOAJ – Directory of Open Access Journals
- Index Copernicus International
- PiraBase (by Smithers Pira)
- Paperbase (by Innventia and
  Centre Technique du Papier)
- NSD – Norwegian Register for
  Scientific Journals, Series and Publishers

Submissions and inquiries

journal@iarigai.org

Subscriptions

office@iarigai.org

More information at

www.iarigai.org/publications/journal